THESIS FOR THE DEGREE OF DOCTOR OF PHILOSOPHY

CHARACTERISATION AND MODELING OF COUPLED-CORE OPTICAL FIBERS

Ekaterina Deriushkina

Photonics Laboratory
Department of Microtechnology and Nanoscience - MC2
Chalmers University of Technology
Göteborg, Sweden, 2024

CHARACTERISATION AND MODELING OF COUPLED-CORE OPTICAL FIBERS
Ekaterina Deriushkina

ISBN 978-91-8103-043-3
Doktorsavhandlingar vid Chalmers tekniska högskola
Ny serie nr 5501
ISSN 0346-718X

Chalmers University of Technology
Microtechnology and Nanoscience - MC2
Photonics Laboratory
SE-412 96 Göteborg, Sweden
Phone: +46 (0) 31 772 1000

Front cover illustration: A cat that is dreaming about the cat-shaped impulse response of the fiber calculated with the random coupling model. Credits: Yan Gao (cat drawing), Vsevolod Deriushkin (illustration creation).

Printed in Sweden by
Reproservice
Chalmers University of Technology
Göteborg, Sweden, May 2024

CHARACTERISATION AND MODELING OF COUPLED-CORE OPTICAL FIBERS

Ekaterina Deriushkina
Photonics Laboratory
Department of Microtechnology and Nanoscience - MC2
Chalmers University of Technology

Abstract

The growth in data traffic coupled with trends in internet use will result in a requirement for interfaces of the network to reach Tb/s data rate in the future. Considering this, novel transmission techniques that can increase the data rate with orders of magnitude must be considered. Coupled-core fibers (CCFs) have several closely spaced cores in the same cladding, which allows carry more data in the spatial domain with slower accumulation of group delay spread (GDS) and higher tolerance to nonlinearities. Application of CCFs in communication systems, though, is coupled with distortions of the signal due to GDS and other effects. They can be calculated, studied and partially mitigated if the transfer function of the fiber under test is known. Thus, it is essential to characterise the fiber's transfer matrix using fast and accurate measurement techniques. These characterisation measurements can also be used for building channel models that assist in simulations of the transmission and estimation of ultimate system performance.

In this thesis a novel method for fiber's characterisation based on dual-comb spectroscopy (DCS) and swept-wavelength interferometry (SWI) is proposed and evaluated. DC-SWI is studied in terms of capabilities, advantages and limitations with application on a CCF with three cores, for which the transfer function was measured. It is found that DC-SWI enables measurement of the broadband features that can not be measured using DCS and provides flexible trade-offs on SNR and frequency resolution. Unlike in SWI, in this experimental scheme it is not necessary to construct an additional interferometer for laser's sweep nonlinearity compensation. Furthermore, this thesis discusses proposed random coupling models that describe the linear properties of CCFs. The application of these models is investigated for CCFs with three and four cores. Modeled results show very good agreement with theory and measured data, which paves the way for using these models in DSP tests, simulations and investigation of installed fibers.

Keywords: swept-wavelength interferometry, dual-comb spectroscopy, transfer function, coupled-core optical fibers, channel modeling.

Publications

This thesis is based on the work contained in the following papers:

[A] **Ekaterina Deriushkina**, Israel Rebolledo-Salgado, Mikael Mazur, Victor Torres-Company, Peter Andrekson, Simon Gross, Michael J. Withford, Tetsuya Hayashi, Takuji Nagashima, Jochen Schröder, and Magnus Karlsson, "Characterisation of a Coupled-Core Fiber Using Dual-Comb Swept-Wavelength Interferometry", in *European Conference on Optical Communication (ECOC)*, Bordeaux, France, Sep, 2021.
DOI: 10.1109/ECOC52684.2021.9605879

[B] **Ekaterina Deriushkina**, Israel Rebolledo-Salgado, Mikael Mazur, Victor Torres-Company, Peter Andrekson, Jochen Schröder, and Magnus Karlsson, "Dual-Comb Swept-Wavelength Interferometry: Theory and Experiment", *Journal of Lightwave Technology*, vol. 40, no. 19, pp. 6508-6516, Oct, 2022.
DOI: 10.1109/JLT.2022.3196161

[C] **Ekaterina Deriushkina**, Jochen Schröder, and Magnus Karlsson, "Modeling of 3-Coupled-Core Fiber: Comparison Between Scalar and Vector Random Coupling Models", *Journal of Lightwave Technology*, vol. 42, no. 2, pp. 793-801, Jan, 2024.
DOI: 10.1109/JLT.2023.3322634

[D] **Ekaterina Deriushkina**, Jochen Schröder, and Magnus Karlsson, "Analysis of the Scalar and Vector Random Coupling Models

For a Four Coupled-Core Fiber", *European Conference on Optical Communication (ECOC)*, Glasgow, UK, Oct 2023.
DOI: 10.1049/icp.2023.2335

[E] Erik Börjeson, **Ekaterina Deriushkina**, Jochen Schröder, Magnus Karlsson, and Per Larsson-Edefors, "Circuit Implementation of Pilot-Based Dynamic MIMO Equalization for Coupled-Core Fibers", *Optical Fiber Communication Conference (OFC)*, San Diego, USA, March, 2024.

[F] **Ekaterina Deriushkina**, Jochen Schröder, and Magnus Karlsson, "Dynamic Model For Coupled-Core Fibers", *Journal of Lightwave Technology*, submitted.

Other publications by the author, not included in this thesis, are:

- [G] Krishna Twayana, Israel Rebolledo-Salgado, **Ekaterina Deriushkina**, Jochen Schröder, Magnus Karlsson and Victor Torres-Company, "Spectral interferometry with frequency combs", *Micromachines*, vol. 13, no. 4, 614, 2022.
  DOI: 10.3390/mi13040614

- [H] Zonglong He, Shen Li, **Ekaterina Deriushkina**, Peter Andrekson, Erik Agrell, Magnus Karlsson, and Jochen Schröder, "12.2 bits/s/Hz C-band Transmission with High-Gain Low-Complexity 24-Dimensional Geometric Shaping", *Journal of Lightwave Technology*, early access.
  10.1109/JLT.2024.3379882

- [I] **Ekaterina Deriushkina**, "How to couple the light to 3CCF".
  DOI: 10.13140/RG.2.2.27868.97928

Contents

Acknowledgement

After almost 5 years of my PhD study in Photonics lab I feel thankful to all the people that have contributed to my work and life. First and foremost, I would like to thank my supervisors, Prof. Magnus Karlsson and Dr. Jochen Schröder, for giving me the opportunity to start my journey towards PhD and guiding me throughout the scientific terrain. Thank you, Magnus, for always having your doors open and teaching me thousands of interesting and important things, not only scientific matters. Thank you, Jochen, for your patience and for showing me the world of Linux and Python. I am grateful to Prof. Peter Andrekson for being such a responsible examiner and leader of the Photonics lab, always motivating and helping me with the research and teaching. I also want to thank my co-supervisor, Prof. Erik Agrell, and all the researchers and colleagues from KAW Dimensions project. I want to acknowledge the funding for the research project, which are the Knut and Alice Wallenberg Foundation (KAW 2018.0090), the Swedish Research Council (VR) project 2019-04078, and the Swedish Foundation for Strategic Research (FID16-0011).

My enormous gratitude is devoted to Prof. Victor Torres Company for his openness, great organization of courses and enlightening the subject matter of the comb spectroscopy. Dr. Israel Rebolledo-Salgado deserves many thanks for his trust, friendliness and for making me understand the dual-comb spectroscopy basics and general lab stuff. Thank you, Dr. Krishna Sundar Twayana, for the time that you devoted to explaining to me the swept-wavelength interferometry technique and for your joyful laughter that has always cheered me up. I would also like to

show gratitude to Dr. Mikael Mazur for his help in the lab in my first months and for participation in the research we made. I am grateful to Dr. Shen Li for all the time we spent together (not only in the lab!) and for sharing her expertise in optical communication. I am thankful to Dr. Erik Börjeson for a nice collaboration and discussions on MIMO algorithms. I am grateful to Mohammad Farsi for all our discussions and collaborations. Special thanks is to brilliant-minded Zonglong He, with whom I am so proud to work and have a friendship. This time has really been special thanks to you. Thank you, Dr. Ali Mirani for your kindness, support, help in the lab and for valuable friendship that went through the joint courses to surfing in the ocean and insightful talks. Rasmus Larsson deserves a "stort tack" for all help during these years and for showing me the best of the Swedish culture and nature. Min vän, tack så jättemycket att du finns I mitt liv!

I am grateful to Dr. Kovendhan Vijayan who shared his excellent knowledge and helped in the lab all the time and Dr. Ping Zhao who is always very friendly and helpful if some issues occur. Dr. Ruwan Udayanga shared a lot of life wisdom together with the lab experience and his smile and support always helped me to stay positive. It has always been a pleasure to spend time in and outside the lab with Vijay Shekhawat, since his sense of humor mixed with intelligence made this time special. I give my special thanks to Manish Raj for his trust, curiosity, kindness, perseverance and for taking the lead with DC-SWI setup, with which I wish him the kindest luck. I thank Dogukan Apaydin for teaching me the things about PCSELs and giving valuable tourist advice on gorgeous Turkey. My big thankfulness is to Dr. Alexander Caut for teaching me a lot of stuff about Canvas and having interesting discussions not always related to science. I am grateful to Yan Gao for giving his drawing for my thesis cover and for nice scientific discussions. I want to thank Prof. Åsa Haglund for all the help and for encouraging me to follow my future goals. I am thankful to all people in Photonics lab for helping, sharing interesting insights and having nice talks.

I am grateful to Jeanette Träff, Gunnel Berggren, Debora Perlheden and Susannah Carlsson for being so nice and professional administrators who do significant work. Thank you, Jeanette, for all your help in my first days in Gothenburg. I wish to thank the former head of department, Prof. Mikael Fogelström, for great support and excellent organization of the work in MC2.

I am grateful to Prof. Serguei Cherednichenko for giving me an opportunity to teach from my very first days in Chalmers and sharing his experience. I express my profound gratitude to all my students with whom I have worked during my life, and especially these 5 years. I have learnt a lot from our lectures, tutorials, and discussions. Special thanks is to Leo and Devin for their trust and interest. I am extremely thankful to TFUK project and personally to Mikhail Khotyakov and Igor Kogan for this miraculous space. I thank Tali Green, Zoya Kozlova, Elena Mikhina, Halyna Dostova, Anna Sokolova and other colleagues that create the project with the deepest warmth of my heart for sharing their love and joy.

I am grateful to Dr. Anna Klepikova for her optimism, excellent mind, and support. Time flies, but we are here again, working in the same building, so I am sure that you are a special person. I thank Dr. Anna Punanova for her sudden and beautiful appearance in my life, which played out as a very appreciated friendship. It will be hard to convey with words my gratitude to Oxana Ahlström (Lubchenko), who has been my friend for so many years filled with her support, love, and joy, which helped me a lot during my PhD study. I thank Eduard Yakupov for all the Python debugging discussions and our warm relationship. I am also thankful to Dr. Roman Skoryunov for all support and participation, which brought me a lot of gladness.

I want to thank my karate sensei Christian Olausson and all karate team for the hardest training sessions that helped me to reboot my mind and for sharing treasured knowledge and skills. Very special thanks to Joakim Holmlund and Björn Andersson for giving us rental contracts in the most beautiful places in Gothenburg (and in the world!) and for always being helpful. I appreciate the great work of my language teachers Dr. Zahia Bouaissi, Davide Gemello, Roberto Mendez, Dr. Anna Oveshkova and Kristina Mamayusupova, thanks to whom I improved my skills and have had a really great time during these years. I am grateful to Dr. Marcello Girardi, Sara Persia and all the Italian lunch group for having very interesting conversations with me in Italian language. Muchas gracias to Estrella Torres for bringing a lot of joy and support and for having conversations in Spanish with me. I am grateful to Sarah Ronström Kern for all the help, nice discussions and beautiful company in journeys. I also thank Linda Brånell for playing a huge role in my Swedish language improvement and for helping me to settle down in Gothenburg.

I want to express acknowledgement to my school physics teacher, Yury Basargin, and Ural Federal university professors Evgeny Pamyatnykh, Yury Panov, Irina Bostrem and Vladimir Malishev for being excellent teachers and supervisors and showing me an exciting world of science. Prof. Eugene Kogan deserves my gratitude for changing my life after the magical meeting in Trieste and sharing his knowledge regarding science and life in general. Big thanks goes to Dr. Olga Yuzefovych, Dr. Mikhail Popov, Dr. Natalia Urusova, Anton Firsin, Dr. Svetlana Gudina and Alexander Saveliev.

In this last, but very special paragraph I want to express my profound gratitude to my family. I thank my mother, Oxana Ilchenko and my deceased father, Vladimir Ilchenko, for encouraging my passion for science and accepting all my life choices. Thank you for your love and endless support. I am especially grateful to my younger sister, Maria Ilchenko, who has always been curious about the world and shared her dreams and thoughts. It has always been fantastic to be your sister! I am so happy to have such a nice mother-in-law, Liubov Deriushkina, whose great wisdom and joy have assisted me all the time. I am extremely glad that I became a part of your family. Finally, and most importantly, huge and very special gratitude to my husband, Vsevolod Deriushkin. I appreciate a lot your help with the algorithms and effective code structuring that I have learnt from you as well as all the time that has been given to us: be it playing music, hiking, discussing the philosophy or just sitting in silence - all the time with you is precious and it is the most treasured gift. Obviously, this work would not have been possible without your continuous love, support, trust, and faith in me.

Ekaterina Deriushkina
Göteborg, April 2024

Dedicated to my father, Ilchenko Vladimir Ivanovich, who passed away at the age of 44 and was the best engineer that I have ever known.

Acronyms

3CCF	three coupled-core fiber
4CCF	four coupled-core fiber
ACF	autocorrelation function
ADC	analog-to-digital converter
AOM	acousto-optic modulator
AWGN	additive white Gaussian noise
BER	bit error rate
CCF	coupled-core fiber
DAQ	data acquisition
DCS	dual-comb spectroscopy
DC-SWI	dual-comb swept-wavelength interferometry
DGD	differential group delay
DMGD	differential mode group delay
DSP	digital signal processing
DUT	device under test
EDFA	erbium-doped fiber amplifier
FC	frequency comb
GDs	group delays
GDS	group delay spread
GVD	group velocity dispersion
IIR	intensity impulse response
MCF	multi-core fiber
MDL	mode-dependent loss
MMF	multi-mode fiber

MIMO	multiple-input and multiple-output
NLSE	nonlinear Schrödinger equation
PMD	polarization mode dispersion
SDM	space division multiplexing
SMF	single-mode fiber
SNR	signal-to-noise ratio
SWI	swept-wavelength interferometry

CHAPTER 1

Introduction

1.1 Motivation

Optical fibers and photonic devices are central to modern communication links and have applications in other areas like medicine and metrology. Since the development of the first optical fibers and their application in gastroscopy [1] and data transmission [2] it was relevant to characterise their parameters. Characterisation measurements assist in estimation of the device quality, its manufacturing process and can give a clue of how the investigated properties can be improved. Extracted parameters can also be used to model the optical channel, which is a paramount task in optical link design and capacity estimation.

The purposes of characterisation are not limited to only quality control. Even if a manufacturing process results in photonic devices of extremely high quality, there are still other features that can be measured and provide information about the device, such as coupling coefficients, higher order dispersion, mode-dependent loss (MDL) or differential group delay (DGD). All such parameters can be extracted from the transfer function, which describes how the output of the system is connected with its input. In other words, if the transfer function of the device under test (DUT) can be measured, almost all linear parameters of interests can be easily extracted. Moreover, results of such measurements can contribute to channel models, which can be beneficial in simulations and further improvements of the optical links. In fact, the channel model is crucial in communication theory for estimating the performance of a communication channel. More specifically, the channel capacity, i.e., the maximum data rate that can be transmitted error-free over a channel, depends solely on the channel model, as pioneered by Shannon in 1948 [3].

Since the demands on data throughput have risen intensely, space division multiplexing (SDM) components have gained significant interest thanks to their potential of increasing the data capacity. There are three general approaches in SDM: multiple independent cores inside a fiber (multi-core fiber (MCF)) [4], transmission through several modes of a multi-mode fiber (MMF) [5] and the use of a special type of MCF with close core spacing, the coupled-core fiber (CCF) [6]. All these fiber types have their advantages and limitations and have been applied in different scenarios. CCFs are particularly interesting for application in optical transmission because of their higher tolerance to nonlinearities and slower accumulation of group delay spread (GDS) with distance due to strong coupling between the cores [7]. CCF transmission, however, is associated with complex random coupling effects that impair propagation and can make digital signal processing (DSP) complicated. This further highlights the relevance of developing high-precision characterisation techniques that can assist in extraction of these impairments and creating realistic channel models for CCFs. In the following section I will review the history of optical characterisation techniques and channel models with a specific emphasis on applications in SDM.

1.2 History

1.2.1 Characterisation of optical fibers and photonic devices

The history of optical fiber characterisation measurements most likely started in 1970, when Kapron with coauthors from Corning published a seminal work on low-loss silica fibers and the measurement of their propagation losses [8]. Another key parameter for fiber characterisation was dispersion since it limited the transmission reach. One of the first works where it was characterised dates back to 1973, where the authors extracted the pulse dispersion by injecting short impulses of light into a fiber and measuring the temporal pulse spread at the output [9]. The pulse dispersion versus length was then measured as a step in a quality control after the manufacturing [10] using a shuttle pulse technique [11]. At the same time, experiments for extraction of material dispersion in the 700-930 nm [12] and 1064-1550 nm [13] wavelength ranges by the time of flight (pulse delay) technique were established. This method is based on injecting pulses of different wavelengths into a fiber and measuring the change in temporal separation between the pulses after propagation through the fiber. Throughout the years the time of flight method using fiber Raman lasers [14], discrete-wavelength laser diodes [15], supercontinuum-radiation sources [16] and tunable soliton sources [17] has been applied for characterisation of photonic devices. Today it is also extensively applied for transfer matrix characterisation [18] and included in methods recommended by the International Telecommunication Union for dispersion measurements alongside with phase-shift [19] and interferometric techniques [20].

With the emergence of optical modulation technologies, other techniques for dispersion characterisation arose. The chirp parameter and chromatic dispersion were measured in the frequency domain with small modulation depth, where sharp resonance frequencies originating from interferences between carrier and sideband wavelengths appear [21]. Another type of technique implied applying modulation instability sideband generation for dispersion and nonlinear coefficient extraction [22]. A method based on the phase mismatch of four-wave mixing was developed in the work [23] and demonstrated dispersion measurements with an accuracy of 0.03 ps/nm/km.

All these techniques would not be possible without the invention of the laser [24]. In 1960 Maiman launched the first ruby laser [25] and one year later, the first continuously operating gas laser was invented [26] at Bell Labs. A few years later, in 1964, Hargrove and collaborators constructed the first mode-locked laser that emitted ultrashort pulses [27]. In the optical frequency domain such a laser presents a sequence of discrete lines that were equally spaced manifesting a comb-like structure. This formation was called a frequency comb (FC) and since 1964 the interest in FCs has led to remarkable research and inventions, particularly in the context of the dual-comb spectroscopy (DCS), which will be described in more detail in Section 2.2.4. This technique has been applied for characterisation measurements not only in photonics [28] but also for liquid [29] and gas samples [30]. Another early example of comb-based fiber characterisation is [31], where a dual-quadrature detection scheme based on polarization demultiplexing was used to characterize the dispersion of the fiber under test. The DCS was also combined with phase-sensitive optical time-domain reflectometry for temperature and strain change characterisation in fibers [32] and with single-pixel-imaging for optical vortex characterisation [33]. In terms of SDM, DCS was recently applied to characterise a 110-km CCF [34]. Other applications of dual-comb interferometers include spectroscopy [35], vibrometry [36], and imaging [37].

Another key technology in this context is tunable lasers. In 1966 Mary L. Spaeth invented the first tunable laser pumped by a ruby laser and in 1980s came the arrival of semiconductor diode lasers that could be tuned using temperature or injection current. These lasers enabled a tremendous progress in telecommunications, but also provided novel experimental opportunities in terms of characterisation of photonic devices. For example, they are crucial in the Poincaré sphere [38] and the Jones matrix [39] methods for measuring polarization mode dispersion (PMD), which is one of the principal impairments in optical fibers.

In 1980s appeared a set of techniques that can be united under the basis of swept-wavelength interferometry (SWI). Eickhoff and Ulrich described optical frequency domain reflectometry (OFDR) in 1981 [40], one of the first such interferometric techniques. Since that time OFDR systems have been developed to characterise fiber-optic networks and components [41, 42] and were employed to measure strain [43], temperature [44] and vibrations [45]. Recent work [46] demonstrates a characterisation of of group and phase delays induced by bending and twisting in a three coupled-core fiber (3CCF) using OFDR. Other SWI techniques include FMCW ladar (laser detection and ranging) [47] and swept-source optical coherence tomography, which has been highly successful in measuring biological samples, such as skin [48]. In SDM devices characterisation it is usual to extend SWI with the configuration called optical vector network analyzer (OVNA). Recent progress shows that this technique is successful in transfer function extraction for few-mode fibers [49, 50], MMFs [51], deployed SDM fibers [52] and spatial multiplexers [53, 54].

Another important breakthrough in characterisation techniques happened in 1948 when Denis Gabor [55] invented holography, a method which enables capturing both amplitude and phase of a DUT by utilizing the interference of light. A medium containing this information is called a "hologram" [56]. A 3D image can be then reconstructed from a hologram by using the theory of diffraction of light. Digital holography (DH) [57] that was developed in 1960s is a technique in which a digital hologram that contains an object wavefront is recorded, and both 3D and quantitative phase images of a DUT are reconstructed using a computer. These developments enabled many applications, which are reviewed in [58] and during the last several years DH became one of the common techniques for characterisation of SDM devices and has been applied to characterise fibers with high mode count [52], photonic lanterns [59] and multimode erbium-doped fiber amplifier [60]. A comprehensive overview on characterisation of SDM fibers using DH can be found in [61].

The historical steps discussed above show a broad perspective of characterisation for the fiber optics research, while the focus of this thesis is on CCFs. A recent review paper on CCFs [6] provides more information about how various characterisation techniques can be applied to measure the transfer function specifically in this type of the fibers.

1.2.2 Modeling of SDM fibers

The purpose behind characterisation of optical fibers can also include building realistic optical channel models, as was mentioned in the previous section. Channel modeling research started from Shannon's communication theory [3] for channels with additive noise and was actively applied in wireless communications [62] and in optical wireless communications [63]. Fiber optical channel models were not described through the concept of communication theory until 2000s, when novel modulation formats [64] and forward error-correction coding appeared in optical communications research [65]. The conventional channel modeling in fiber optical communication was based the on nonlinear Schrödinger equation (NLSE), which can be solved efficiently by the split-step Fourier method [66]. Nevertheless, this method can still be too computationally demanding, especially for real-time applications. This issue paved the way to developing new techniques to model the propagation in an ordinary single-mode fiber (SMF) and then became a basis for modeling novel MCFs. The paragraphs below will provide a short historical review of these developments.

The simplest representation of the SDM fiber is a SMF since in reality it has two modes related to horizontal and vertical polarizations. The development of SDM channel models, thus, is strongly related to theoretical concepts on polarization that were continuously studied after the low-loss optical fibers invention. Earlier in 1970s, the models accounting for polarization impairments were not used much in communication since optical receivers detected the optical power, rather than the field, and were not sensitive to polarization. However, the invention of erbium-doped fiber amplifiers (EDFA) in the 1980s [67] made long-haul optical links possible and the accumulated polarization effects, like PMD, manifested their importance. Since then, the models accounting for polarization impairments were in great demand. The PMD, a phenomena causing the pulse distortion because two modes of different polarizations propagate with different speed, was first measured in [68] and then modeled in [69], where the concept of principal states of polarization (PSP), was first introduced. The PSP are free of group delay dispersion to first order in frequency and form the basis for adaptive optical techniques to compensate PMD in direct detection systems [70]. Since then there were many established models, where PMD and the polarization-dependent optical power attenuation called polarization dependent loss (PDL), were studied. Models based on differential equations describing the state of polarization (SOP) change with frequency and fiber length were presented in [71, 72]. The combined effects of PMD and PDL in optical fibers were investigated in [73]. The PMD was mostly studied with the concatenation model, which is a powerful tool allowing determination of the PMD vector of a set of concatenated fiber pieces with the known PMD vectors. The idea of the model first appeared in experimental work [74] and then was actively developed further [75] and summarized in [70]. The statistical analysis of polarization effects was performed in some of the previously mentioned works, while the autocorrelation function (ACF) of the PMD vector was first derived in 1999 in [76], which enabled estimation of the bandwidth over which the first-order PMD is applicable. In a couple of years, a generalized theory for computing the probability density function of the PMD vector was presented [77].

Later, when interest in coherent detection arose, models that describe electromagnetic wave propagation accounting for the polarization became relevant. To model such a propagation without PDL, the unitary 2×2 Jones transfer matrix formalism [78] was typically used. The description of a polarized electromagnetic wave in terms of its four real quadrature components was pioneered in papers [79] and [80]. There appeared then another analysis, where an extension of the conventional polarization analysis was applied to cover the full degrees of freedom of real four-dimensional rotations [81]. Performance degradation in coherent polarization multiplexed systems as a result of PDL was studied in [82]. Another direction related to models that account for the static [83] and dynamic [84] changes of the SOP during transmission in coherent fibre-optic systems. Paper [85] presented a pioneering model for random SOP drifts in the time domain by generalizing the one-dimensional phase noise random walk to a higher dimension. This model was described in the Jones, Stokes and mentioned 4D formalism. A comprehensive review of channel models related to polarization effects in fiber optical communication systems can be found in [86]. At the same time, in 2000s, there appeared a lot of collaboration between communication and fiber optics researchers since the increased attention to coherent communication demanded an explicit input-output relationship for the fiber optical channel. A good review of such channel models is given in [87].

The models that described the polarization effects became the basis for the first models that appeared after developing the SDM technologies. The modes behavior in MMFs and in MCFs considered to follow similar mechanisms of coupling. The concept of principal modes, the modes that are free of modal dispersion to first order in frequency, was in this sense similar to PSP. Principal modes are fundamental for adaptive optical techniques to compensate modal dispersion in direct-detection systems [88]. Fan and Kahn first predicted the existence of the principal modes in MMFs [89] and the theory was then developed for the random coupling regime in [90]. In [91] authors experimentally demonstrated the principal modes in a six-mode fiber.

When the spatial modes in SDM fibers experience different attenuations, it is said that the fibers have MDL, the phenomenon which is parallel to another polarization effect, PDL. The statistical properties and system impact of MDL in the strong-coupling regime in MMFs were studied in [92, 93]. It was shown that the distribution of the modal gains is equivalent to the eigenvalue distribution of a zero-trace Gaussian unitary ensemble, which is the same as the distribution of the modal group delays [94]. The performance metrics of multiple-input multiple-output (MIMO)-SDM systems with different amplification schemes was investigated in work [95].

Another big trend in modeling MCFs has been supermodes, which are the superposition of the individual modes and the spatial eigenmodes of a MCF. This concept is very useful for describing unperturbed, ideal SDM fibers. The coupled-mode theory (CMT) described in [96] and [97] provided a solid basis for numerous studies of the supermodes and coupling mechanisms in CCFs and MMFs. The analytical approach for two waveguides in a weak coupling regime was published in [98] and one of the first works on two-core fiber was done in [99], where the intermodal dispersion was analytically derived and studied. The coupled-mode analysis for describing the coupling properties of linear-core-array microstructured fiber was shown in [100]. Xia et al. presented the study of the supermodes in a four coupled-core fiber (4CCF) [101] and other CCFs [102], including higher-order supermodes analysis. A comprehensive analytical and numerical work on a CCF with 19 cores was presented in [103]. Supermode characteristics were also investigated in nested multiple hollow-core strongly coupled anti-resonant fibers [104]. In work [105] the supermodes behavior, including the effect of all high-order inter-core couplings, was explored with finite element simulation and compared with the CMT results.

The deterministic models mentioned in the previous paragraph are very useful to study an ideal CCF, without any perturbations. To model a realistic CCF, though, it is important to include the effects of random mode coupling, as it is the main characteristic of such fibers that impact propagation, mainly through the modal dispersion. The effects of random mode coupling in CCFs can be evaluated by the CMT as well and were discussed in a recent work [106]. The coupled mode equation for the waveguide mode system in this case should account for random variations of coupling coefficients [107]. The modal dispersion and its statistical properties in coupled SDM fibers can also be studied using an extension of the formalism developed for PMD [108]. The model was also generalized to a case when the MDL is present in the system [109] and validated by comparison with experimental data.

As temporal fluctuations in the channel can impair the signal, the models that describe dynamic changes in SDM fibers have been in great demand. The ultra-short pulse propagation model for MCFs [110] is based on the concept of local modes, in which the fiber perturbations effects, including various types of nonlinear effects, are incorporated into Maxwell equations. In [111], the authors carried out an experimental analysis of the time-dependence of the transfer matrix of a few-mode fiber, and proposed its parametrization to describe the temporal evolution. The time drift was mathematically expressed as an operator that depended on phase variations. A similar approach was used in [112], where the authors not only designed a model for fast and slow time variations in MMFs, but also tested it for an adaptive MIMO equalizer. Such tests became extremely relevant after emerging experiments on the real-time transmission through CCFs [113, 114] since they assist in studying equalizer performance using a specific channel model. It becomes even more useful if the parameters of the model are fit to properties of field-deployed CCFs, as has been performed in [Paper E]. In a recent work [115] devoted to the dynamic model for MMFs, the authors propose a method for simulating the time and frequency-dependent transfer matrix in all linear coupling regimes.

The linear effects discussed above limit data capacity in fiber telecommunications, but can in general be mitigated by various techniques. However, the nonlinear Shannon capacity limit has been identified as the fundamental barrier to the maximum rate of transmitted information in optical communications as nonlinear effects can occur and can be designed in various ways [116]. Numerous models were created to describe nonlinear impairments in the optical fibers [117], and a lot of efforts have been made to estimate the capacity of the nonlinear optical channel [118]. In case of a SMF, nonlinear propagation is governed by a pair of coupled NLSEs [66], while in the MMF case it is replaced by 2N coupled NLSEs having a more general form [119]. It was shown that in realistic scenarios the nonlinear propagation in MMFs can be modeled with coupled generalized Manakov equations [120]. The Gaussian noise models [121] attracted a lot of attention because of their computational simplicity comparing to other techniques and have been extended for SDM fibers in [122] and in [123], where the authors also took the effect of spatial mode dispersion into consideration. The tutorial [124] gives a broad review over various models for SDM fibers accounting for nonlinear behavior. Communication friendly models accounting for nonlinearities are reviewed in [87]. Extensive research has also been done on the models implemented with the nonlinear Fourier transform [125], another way of solving the NLSE.

1.3 This thesis

The focus of this thesis is on characterising the full linear transfer function of CCFs for building realistic channel models. For this purpose we employ a technique, which combines DCS that is based on the probing a DUT with frequency combs and SWI, where a tunable laser source is used to scan a DUT over a large wavelength range. The established technique, dual-comb swept-wavelength interferometry (DC-SWI), exhibits advantages and flexible trade-offs from both DCS and SWI and enables fast characterisation of CCFs. The experimental results can give the input for modeling the transfer function of CCFs. Thereafter, we designed static and dynamic random coupling models that assist in calculation of the transfer function of CCFs.

The papers included in this thesis mark the benefits of the proposed experimental technique, demonstrate the results on transfer function characterisation and show the analysis of the simulation results obtained using proposed random coupling models for CCFs. In [Paper A], we perform transfer function characterisation of a 3CCF using DC-SWI. The root mean square (RMS) widths of the impulse responses and differential mode group delay (DMGD) values were estimated for every core. [Paper B] is devoted to the comprehensive description of the DC-SWI technique. We discuss the operation principle, experimental implementation, DSP, performance characteristics, advantages and limitations. In [Paper C] we present for the first time, to the best of our knowledge, a comparative analysis between scalar and vector models for 3CCFs. We derive an analytically tractable vector model of the supermodes for an unperturbed 3CCF, accounting for the birefringence from the presence of nearby cores. The model is extended to account for the effects of random mode coupling to analyze the intensity impulse response (IIR) as well group delays (GDs) in a 3CCF by using the concatenated waveplate model. Comparisons with measured IIR [Paper A] then enable an estimate of the correlation length of the fiber. In [Paper D] we present a comparative analysis of the scalar and vector random coupling models for a 4CCF in the ideal case and random coupling regime. In [Paper E] we use our channel model to explore an ASIC implementation for pilot-based MIMO equalizers for coupled-core transmission. This enables a study of chip area scaling trends and performance impact of time-dependent drift. [Paper F] is devoted to designing a dynamic model for CCFs, which contains a static frequency dependent part presented in paper [Paper C] and time-drift part implemented in paper [Paper E]. We show simulation results for IIR, GDs and ACF of a 4CCF, which has the same geometrical parameters as the 4CCF used in reported transmission experiments [113]. We also provide an analytical derivation of time and frequency ACFs in our model.

The outline of this thesis is as follows. In Chapter 2, various SDM-focused characterisation techniques, their advantages and limitations are discussed. Chapter 3 introduces the DC-SWI technique, its implementation scheme, features and capabilities. Chapter 4 overviews the proposed channel models for CCFs. Finally, in Chapter 5, the future outlook is presented and Chapter 6 outlines the main results in the appended papers.

CHAPTER 2

Characterisation of SDM devices

Characterisation of optical fibers and photonic devices is extremely important for quality control and gaining principal information for fiber optical links and their improvement. This requires application of accurate and sensitive measurement techniques capable of retrieving the parameters of interest. Some of the most important characterisation techniques were highlighted in the introduction chapter. In the following I will review spatial and temporal SDM characterisation techniques, with an emphasis on DCS and SWI since they form a basis for DC-SWI, which is one of the topics of this thesis. The chapter starts from a brief description of various impairments present in transmission through SDM fibers that are of importance in characterisation and which should be accounted for in channel modeling.

2.1 Propagation effects in SDM devices

The propagation of the slowly varying envelope of a single polarization electric field along a fiber is described by the NLSE:

$$\frac{\partial E(t,z)}{\partial z} = -\frac{\alpha}{2}E(t,z) - j\frac{\beta_2}{2}\frac{\partial^2 E(t,z)}{\partial t^2} + j\gamma|E(t,z)|^2 E(t,z), \tag{2.1}$$

where $E(t,z)$ is the slowly varying envelope along the fiber at time t and distance z, α is the attenuation coefficient, β_2 is the group velocity dis-

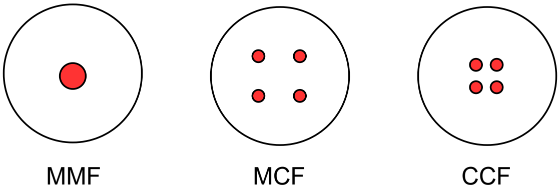

Figure 2.1: Types of the SDM fibers: MMF, MCF and CCF.

persion (GVD) and γ is the nonlinear coefficient. As can be seen, every term on the right-hand side of the equation represents a specific type of fiber impairment. There are thus three main impairments along the fiber: the linear fiber loss and GVD and the nonlinear Kerr effect. There are other linear effects that are relevant for the SDM fibers and will be discussed in this Section. The nonlinear effects can be index-related, like self-phase modulation, cross-phase modulation and four-wave mixing, or scattering-related comprising stimulated Brillouin scattering and stimulated Raman scattering. These nonlinear effects are summarised in [126] and will not be discussed in this section since they are out of scope of this thesis.

SDM fibers can be categorized into MMFs, MCFs and CCFs (Fig. 2.1). The MMFs guide several modes inside one core, while MCFs have multiple cores inside the cladding. The CCFs are MCFs with the cores that are closely arranged. The focus of this thesis and attached papers is on CCFs since they more slowly accumulate GDS than other SDM fibers and exhibit a higher tolerance to nonlinearities, which makes them attractive for long-haul transmission [6].

2.1.1 Attenuation

Fiber loss per unit length is described by the attenuation coefficient α. Attenuation is wavelength-dependent and has three main contributions: Rayleigh scattering at short wavelengths, absorption at long wavelengths and OH-absorption. Around 1550 nm, the sum of their terms is the lowest and the loss typical values are $\alpha \approx 0.2$ dB/km [127]. The power evolution of the optical field in the fiber is dictated by the Beer-Lambert law:

$$P(z) = P(0)e^{-\alpha z}, \tag{2.2}$$

where z is a propagation distance, $P(0)$ is the launched power and α is the attenuation in linear units.

Rayleigh scattering is caused by the refractive index variations due to microscopic fluctuations in material density of the glass, leading to scattering. Absorption appears at longer wavelengths when silica molecules absorb more photons, causing attenuation. Additionally, bending losses can be a significant contribution to accumulated attenuation. If a fiber is bent tightly, the mode moves more to the edge of the core until it is not fully guided any more and starts becoming lossy. This type of loss sets a critical bend diameter found in data sheets of fibers.

Attenuation can be compensated using EDFAs. However, they add noise due to amplified spontaneous emission [128]. The quantum limited noise figure in an ideal EDFA is 3 dB [128], while real-world amplifiers can have the noise figure as large as 6-8 dB.

2.1.2 Group velocity dispersion

The GVD or chromatic dispersion is a linear propagation effect that appears owing to the group velocity is different for different frequency components in the optical fiber. This results in time domain pulse broadening [66] and although spectral components are launched into the fiber at the same time, they have different transit times and will thus arrive at the receiver at different times.

Chromatic dispersion is defined through the dispersion parameter D [ps/nm/km] which gives the pulse broadening per nm of spectral width per km of fiber. It can be described in terms of the propagation constant $\beta(\omega)$:

$$D = -\frac{2\pi c}{\lambda^2}\beta_2, \tag{2.3}$$

where λ is the wavelength, c is the speed of light and β_2 is a term in Taylor expansion of the propagation constant $\beta(\omega)$ that is proportional to its second derivative with respect to frequency evaluated at the carrier frequency ω_0 as $\beta_2 = \frac{\partial^2\beta}{\partial\omega^2}|_{\omega=\omega_0}$.

In SMF links the GVD is static and can be compensated by introducing dispersion compensating fibers or by receiver DSP in case of coherent detection [84]. Thus, it is not a central problem in transmission or channel modeling, unless it is imperfectly compensated.

2.1.3 Modal dispersion

The set of modes, their effective index and group velocity depend on the waveguide geometry. Modes in the optical fiber have different spatial profiles and can have different group velocities. If, for instance, the group velocity for one mode is larger than for another, a pulse exciting both modes will be dispersed and potentially split during propagation along the fiber. This phenomenon is called modal dispersion or intermodal dispersion.

One of the form of modal dispersion is PMD, where the two polarization modes of light in a waveguide propagate at different speeds due to random imperfections breaking the circular symmetry [129]. This results in separation of the signal's polarization components causing spreading of pulses and as for all dispersion effects, the pulse broadening will lead to intrapulse crosstalk that will cause signal distortion and limit the available bandwidth of the channel unless it is compensated. The PMD values of modern low-PMD optical fibers are around 0.02 ps/$\sqrt{km}$.

The strength of modal dispersion can be defined by time delay per unit length. This delay is referred as DGD, DMGD, differential mode delay, spatial mode dispersion, or GDS. The record-low values of modal dispersion measured on 2-core fiber ribbons [130] and on 4CCFs deployed in the SDM fiber testbed in L'Aquila [131] are of 1.5 ps/$\sqrt{km}$ and 2.5 ps/$\sqrt{km}$, respectively, two orders of magnitude larger than aforementioned PMD value. This modal dispersion can be compensated by combining fibers with positive and negative DGD [132, 133]. The principle is to offset the DGD introduced by a certain fiber by a very similar fiber with DGD of opposite sign. However, any mode coupling during transmission deteriorates the compensation making DSP more complicated.

The modal dispersion effect, if static, is not necessarily detrimental for coupled SDM systems since MIMO DSP [134] enables compensation for any mixing. Moreover, the mixing can be even desirable in coupled SDM systems since in the regime of strong coupling DGD accumulates only with the square root of distance [7], which is slower than for uncoupled SDM fibers. However, the random mode coupling that arises in MMFs and CCFs make modal dispersion random as well and time varying. Modal dispersion, thus, requires adaptive equalizers [135] to be compensated, which is challenging if the modal delays are big and the drift is fast. The study [136] showed that the modal dispersion in CCFs can be reduced to 0.1 ps/$\sqrt{km}$ if an even number of cores are placed in a ring-array structure, so that each core is coupled to two identical cores with the same propagation constant mismatch.

2.1.4 Mode-dependent loss

Imperfect coupling in SDM components can lead to different loss in different modes, which results in MDL and deteriorate the transmission performance [137, 138].

In an ideal system without MDL the transfer matrix of an SDM device is unitary. MDL, therefore, is described by non-unitary transfer matrices [92]. Using singular value decomposition, MDL can be then calculated as the ratio between the modulus of the maximum λ_{max} and minimum λ_{min} singular values of the measured transfer matrix, i.e.,

$$MDL_{dB} = 10 \cdot \log_{10} \left[\frac{|\lambda_{max}|^2}{|\lambda_{min}|^2} \right]. \tag{2.4}$$

MDL was measured in the range of 8-10 dB for a 3CCF after 1200 km and 10-12 dB for a three-mode few-mode fiber after 1045 km transmission distance [139]. In [140] MDL a value of less than 0.05 dB over 97.9 km was measured for a 4CCF.

2.2 Experimental schemes for characterisation of SDM fibers

2.2.1 MIMO equalizer tap analysis

MIMO channel equalization [4] assists in unscrambling the mixing of the modes in SDM fibers and resolving the data. The principle is that the signals from outputs of a DUT are received independently (the number of receivers correspond to the number of outputs) and then subjected to the DSP by adaptive equalization. The equalizer adaptively learns how to invert the transmission channel and the filter weights of the equalizer, equalizer taps, contain information about the transmission channel. Equalizers updated using the minimum mean squared error or the least means squares criteria converge to the inverse of the channel transfer matrix in the noiseless regime [141]. Hence, the equalizer taps can be used to simulate the transmission channel and estimate parameters of interest, for example, modal dispersion or MDL.

Modal dispersion can be calculated by analyzing the MIMO equalizer taps in the time domain. The summation of the absolute squared filter weights gives the impulse response of the channel. As was shown in Section 2.1.4, MDL is calculated via singular value decomposition of the transfer matrix of the DUT. MDL calculation is carried out in the frequency domain, so the equalizer has to be run in the frequency domain, or the time domain taps have to be Fourier transformed to represent the frequency domain. It is important to mention though that MDL impairs equalizer convergence, thus increasing the noise of the equalised symbols. Experimental examples and calculation of modal dispersion and MDL for various SDM fibers can be found in Chapter 6 of [61]. Various MIMO equalization algorithms are extensively reviewed in [142].

2.2.2 Spatially and spectrally resolved imaging

Spatially and spectrally (S^2) resolved imaging was first demonstrated in 2008 [143] and applied for imaging higher-order-modes propagating in large-mode-area fibers. The modes that propagate in optical fibers can be identified by both the group delay difference which leads to a spectral interference pattern for a broadband source propagating through the fiber, and a spatial interference pattern between the high-order modes and the fundamental mode [143]. In a MMF, the guided modes propagate with different speeds and spectrally interfere. This results in multi-path interference (MPI) and can lead to signal fading on a slow time scale [144]. The interference period of MPI is connected with the DGD between the two interfering modes. The principle of S^2 imaging is based on measuring the MPI at several spatial points across the transmitted optical beam using a scanning fiber probe.Fourier analysis of the recorded spectra assists in resolving the DGD between two interfering modes and retrieving the corresponding mode profiles.

Figure 2.2 shows the experimental setup for S^2 imaging used in [143]. The light from a broadband optical source is launched into a MMF under test. A magnified image of the output facet is scanned with an SMF which is connected to an optical spectrum analyzer (OSA). A polarizer is needed in order to ensure that polarization states of the modes are aligned on the SMF end-face. The measured optical spectra are Fourier transformed and intensity profiles of the individual modes are extracted. The MPI can be calculated as a ratio of powers of the modes that can be found by integration of intensities over the fiber cross section.

Applications of S^2 imaging include mode analysis not only of large-mode-area MMFs [143, 145], but also photonic crystal fibers [146], all-solid and hollow core band-gap fibers [147], as well as extended long

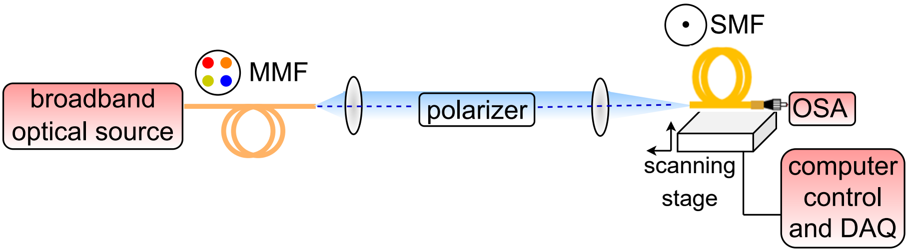

Figure 2.2: Experimental setup for S^2 imaging implementation from [143]

.

tapers [148] and silicon waveguides [149]. It has also been successfully applied to observe supermodes in a coupled few-mode three-core fiber [102], measure higher order mode bend-loss in photonic band-gap fibers [150], characterise efficient higher order mode suppression in scalable output fiber amplifiers [151]. Moreover, S^2 imaging technique was applied in a combination with correlation filter mode analysis for characterisation of optical fibers [152] and such a method provided simultaneous decomposition of one beam with considerable improved accuracy.

2.2.3 Digital holography

Digital holography (DH) is a widely-used imaging method with a lot of applications. In terms of optical fiber characterisation, DH can bring a lot of advantages, especially when a fiber with high mode count and strong coupling is considered [52, 153, 154]. Compared to S^2 imaging that can fail in case of strong mode mixing, DH is more accurate since it acts as a perfect mode demultiplexer [52]. A comprehensive overview of SDM characterisation using DH is presented in Chapter 3.2 of [61].

Figure 2.3(a) demonstrates an experimental setup, where a signal from a DUT beats with an angled reference beam on a camera. The light from an SDM device is imaged with magnification using a free-space optical setup. The interference between DUT signal and reference lead to fringes in optical intensity, which are captured by the camera.

An example of the recorded camera frame taken from [155] and further DSP process is presented in Fig. 2.3(b). First, a part of the image is cropped around the center of interference pattern. Next, these parts can be converted to the angular domain by Fourier transforming. The converted interference pattern needs to be filtered in the angular domain following a similar algorithm, so a new square piece of image has to be

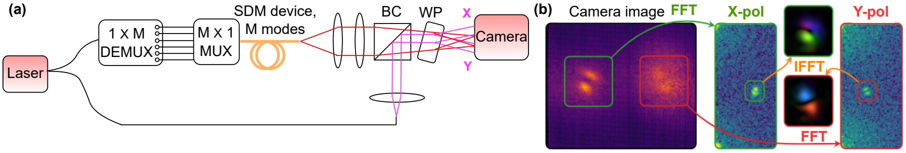

Figure 2.3: (a) Experimental setup for DH implementation. BC - a beam combiner, WP - a Wollaston prism. (b) Example of the DSP from [155].

cropped. The filtered pattern is shifted back to spatial domain using the inverse Fourier transform. The resulted optical field contains both amplitude and phase information making it possible to calculate a complex transfer function of a a SDM-DUT.

2.2.4 Dual-Comb Spectroscopy (DCS)

Dual-Comb Spectroscopy (DCS) uses two FCs with slightly different repetition rates to generate an RF comb that can be measured on an oscilloscope. From the relative phase and amplitude information of the RF comb one can extract the characteristics of the DUT at the corresponding optical frequencies. The DCS is capable of simultaneous measurements of broadband and high-resolution spectra within microseconds. It is also characterised by high signal to noise ratio (SNR), high sensitivity, fast acquisition speeds, a small footprint, and implementation free of moving parts. Recent reviews on DCS can be found in [156, 157] and [Paper G]. Novel experimental schemes using the microcombs are discussed in [158]. This section provides a brief overview of the operation principle, mathematical description, implementation alternatives and key experimental results on the use of DCS in photonic device characterisation.

Operation principle

The operation principle of DCS can be explained in the both frequency and time domain. In the frequency domain two FCs with slightly different repetition rates, f_{r_1} and f_{r_2}, interfere on a photodiode generating an RF comb with a repetition frequency $\Delta f_r = f_{r_1} - f_{r_2}$ formed by heterodyne beating between pairs of the teeth of the optical combs (Fig. 2.4(a)). At least one FC has to pass through the DUT, the frequency response of which changes the shape of the FC (Fig. 2.4(b)). The wavelength-dependent absorption and phase on the comb teeth are

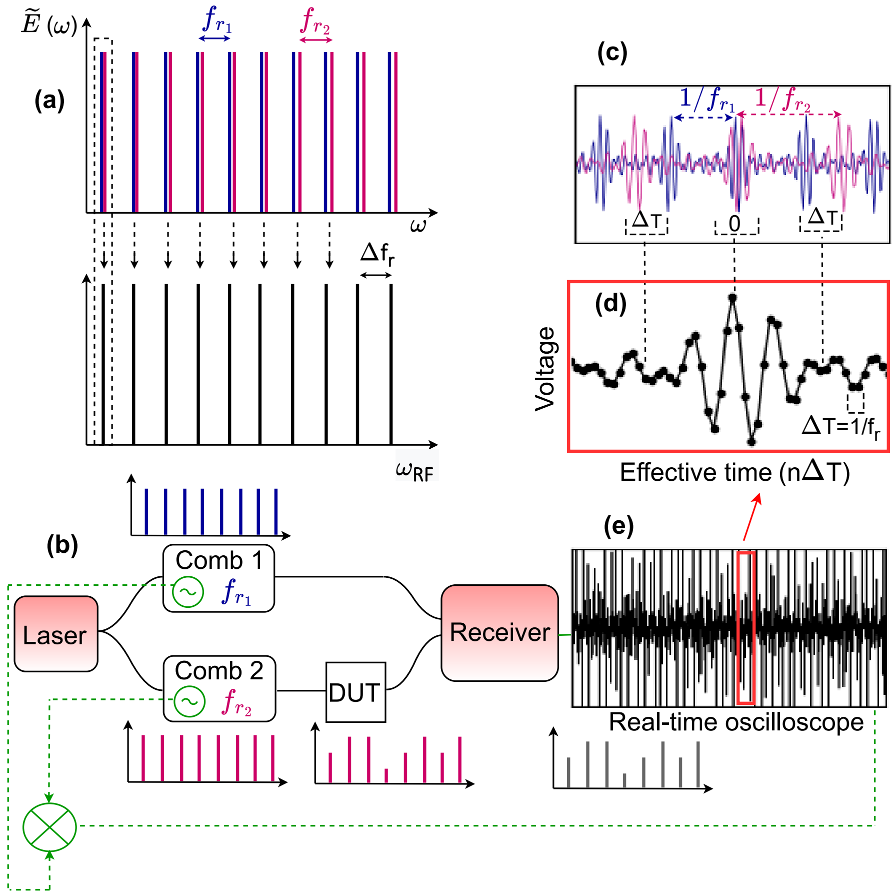

Figure 2.4: (a) Frequency domain representation of DCS. (b) Principle of DCS. The black and green lines relate to optical and RF connections respectively. (c), (d) Time domain representation of DCS for the (c) optical signals and (d) electric signal. (e) Captured interferogram.

modified into the corresponding amplitude and phase of the measured RF comb. The RF comb spectrum can be extracted by Fourier transforming a set of time domain interferograms captured by the real-time oscilloscope (Fig. 2.4(e)).

In the time domain two pulse trains with slightly different repetition rates interact and "walk through" each other (Fig. 2.4(c)). The resulting beating on a photodiode produces an interferogram (Fig. 2.4(e)) that can be described as a product of two FC pulses integrated over the photodiode bandwidth. This signal is usually acquired as a function of the effective time, $n\Delta T$, where n is the sample number at time intervals of ΔT [156]. A weak ringing that can be observed on the edges of the pulse (Fig. 2.4(d)) contains absorption information of the DUT.

Mathematical description

The mathematical analysis in this section is based on the analysis in [159]. Let us denote absolute frequencies of two FCs as $\nu_k = f_{ceo_1} + kf_{r_1}$ and $\nu_m = f_{ceo_2} + mf_{r_2}$, where $k = 0...K-1$ and $m = 0...M-1$ are the comb line numbers and f_{ceo} is a carrier-envelope-offset (CEO) frequency of the corresponding FC, comprising the carrier frequency of the laser. Then, the electric field equations of the FCs can be described as

$$E_1(t) = \sum_{k=0}^{K-1} G_k(\nu_k - \nu_c)e^{i(2\pi\nu_k t+\phi_k)} \tag{2.5}$$

and

$$E_2(t) = \sum_{m=0}^{M-1} G_m(\nu_m - \nu_c)e^{i(2\pi\nu_m t+\phi_m)}, \tag{2.6}$$

where $G_k(\nu_k - \nu_c)$ and $G_m(\nu_m - \nu_c)$ are the spectral profiles of the FCs, ν_c is the center frequency, ϕ_k and ϕ_m are the phase factors. Note that in Fig. 2.4(a,b) both FCs have ideal rectangular shape, which is not true in reality.

After the interaction of two FCs on the detector, the heterodyne interference output voltage is given by [159]

$$U(t) \sim Re\{\sum_{k,m} \tilde{A}_k \tilde{A}^*_m e^{i(2\pi[\nu_k - \nu_m]t)}\}, \tag{2.7}$$

where $\tilde{A}_k = G_k(\nu_k - \nu_c)e^{i\phi_k}$ and $\tilde{A}_m = G_m(\nu_m - \nu_c)e^{i\phi_m}$ are complex amplitudes of the k^{th} and m^{th} components for corresponding FCs.

The RF frequency components after multi-heterodyne interference are defined as

$$\begin{aligned} f_k^{RF} &= \nu_k - \nu_m = f_{ceo_1} + kf_{r_1} - (f_{ceo_2} + mf_{r_2}) = \\ &= \Delta f_{ceo} + (k-m)f_{r_2} + k\Delta f_r = f_{ceo}^{RF} + k\Delta f_r, \end{aligned} \tag{2.8}$$

where $f_{ceo}^{RF} = \Delta f_{ceo} + (k-m)f_{r_2}$ is the artificially prescribed CEO frequency of the heterodyne comb structure, far from the zero frequency to maintain k as a common index between the combs in optical and RF domains [159].

An electronic filter is applied to restrict each optical frequency in FC to one single RF frequency. In this case comb line numbers k and m match each other and are limited to satisfy the following inequality:

$$\frac{-f_{r_2}}{2} < f_{ceo}^{RF} + k\Delta f_r < \frac{f_{r_2}}{2}. \tag{2.9}$$

The range of k is defined by the center wavelength and bandwidth of the optical band-pass filter, and only one possible m responds to a specific value of k under the condition (2.9). Under this requirement the corresponding phases of the RF frequency components can be written as

$$\begin{aligned} \phi_k^{RF} &= \phi_k - \phi_m = \phi_{01} + 2\pi\nu_k\tau_{01} - (\phi_{02} + 2\pi\nu_m\tau_{02}) = \\ &= \phi_0^{RF} + 2\pi f^{RF}\tau_0^{RF}, \end{aligned} \tag{2.10}$$

where ϕ_{01}, ϕ_{02} and τ_{01}, τ_{01} are carrier envelope phases and the initial pulse center positions of two FCs respectively, ϕ_0^{RF} is the carrier envelope phase and τ_0^{RF} is the initial pulse center position of the interferograms.

The output voltage of the detector can then be simplified to

$$U(t) \sim Re\{\sum_{k=0}^{K-1} H(f_k^{RF} - f_c^{RF})e^{i(2\pi f_k^{RF}t + \phi_k^{RF})}\}, \tag{2.11}$$

where $H(f^{RF} - f_c^{RF}) \approx G_k(\nu_k - \nu_c)G_m(\nu_m - \nu_c)$ is the RF spectrum of the interferograms, $f_c^{RF} = f_{ceo}^{RF} + \frac{\Delta f_r}{f_{r_1}}(\nu_c - f_{ceo_1})$ is a carrier frequency (center frequency) of interferograms.

If a DUT is introduced after one of the combs (as in Fig. 2.4(b)), then the shape of the corresponding comb will be changed according to the impulse response of a DUT $h(t)$ and resulting voltage will be modified as

$$U(t) \sim Re\{\sum_{k=0}^{K-1} \tilde{h}_k(t) H(f_k^{RF} - f_c^{RF}) e^{i(2\pi f_k^{RF} t + \phi_k^{RF})}\}, \tag{2.12}$$

where $\tilde{h}_k(t)$ is the impulse response of the individual k-th comb line. (2.12) represents a set of interferograms (Fig. 2.4(e)), which in the frequency domain will give a set of impulse responses separated by Δf_r.

Experimental implementation

One of the advantages of DCS is that it can be implemented on different platforms, for instance microcombs [160] or integrated mode-locked lasers [161] and various configurations, such as sweeping the comb repetition rate by tuning the RF source [162, 163]. One of the most popular options is to use electro-optic FCs [164]. In contrast to mode-locked lasers, electro-optic FCs do not rely on a cavity for constructing the mode spectrum, and therefore provide flexibility in setting the center frequency and spacing between the comb lines. Since electro-optic combs are fed by a single continuous wave laser, they provide mutual phase coherence in the DCS [164–167].

Figure 2.4(b) demonstrates an example of DCS based on electro-optic FCs. The laser is divided into two paths and feeds FCs, one of which is coupled in a DUT. The resulting beating is measured with a receiver and digitized with a real-time sampling oscilloscope. The oscilloscope has to be equipped with sufficient memory to capture the measurement data. It is important to note that the setup has to be synchronized in order to avoid additional DSP steps for compensating a drift in the repetition rate of the comb. In Ref. [165] the authors proposed an RF circuit included in the DCS setup, where the offset in repetition rate frequencies is extracted via a mixer. The signal at the output of the mixer is used as both external clock and trigger for the oscilloscope. In other words, the sampling clock of the digitizer has to be locked to the comb $f_{r_1} - f_{r_2}$ clock. In addition, an acousto-optic modulater (AOM) can be used for shifting away the downconverted center line of the comb from DC [165]. Considered DCS configuration (Fig. 2.4(b)) requires a calibration process, so in a reference experiment the DUT should be removed from the signal arm. This measurement then has to be subtracted from the one with the DUT in post-processing. For each interferogram, the spectral complex amplitude is recovered through a Fourier transform process, which includes conventional tools in Fourier analysis, such as zero padding or phase unwrapping.

2.2.5 Swept-wavelength interferometry (SWI)

Swept-wavelength interferometry (SWI) is one of the most popular experimental schemes for characterising SDM fibers. Various configurations of this technique are reviewed in [Paper G]. Chapter 5 of [168] provides a detailed mathematical description, experimental implementation examples and DSP steps for SWI. This chapter presents an overview of an operation principle, experimental issues and general post-processing steps for SWI.

Operation principle

There are many measurement techniques that can be united under the basis of SWI, as was discussed in the introductory chapter. Nuances of their implementation may depend on the application, but the defining element of all SWI systems is a frequency tunable source, which continuously sweeps the light in a given wavelength range. Unlike in traditional interferometry, where interference patterns are typically observed as a function of a spatial coordinate, the interferogram in SWI is captured as a function of the instantaneous optical frequency of a tunable source. The output of the sweeping source is split into two arms - a reference arm and a sample arm. The optical path length of the reference arm is usually fixed, and the sample arm may include multiple distinct paths. By performing a Fourier transform on the acquired interference pattern data, the impulse response of the sample can be extracted (Fig. 2.5).

As was mentioned above, the interferogram in SWI is captured as a function of the instantaneous optical frequency of a tunable source. This point can be confusing because it is common to refer to raw data acquired by a real-time oscilloscope as time domain data, while data that is Fourier transformed is referred as frequency domain data. In SWI, however, the roles of the time domain and the frequency domain are reversed since the signal is acquired as a function of the instantaneous frequency of the laser source as it sweeps, rather than as a function of time. Moreover, the instantaneous frequency of the laser is a function of the sweeping time. Hence, one can represent the fringes captured in SWI experiments as a two-dimensional function which depends on instantaneous frequency

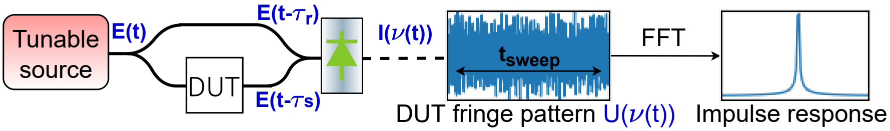

Figure 2.5: Swept wavelength interferometry implemented in a single mode optical fiber based on a Mach-Zehnder structure, showing extraction of the DUT impulse response function.

and sweeping time, which also define a size of the measurement window of the real-time oscilloscope (see Fig. 2.5).

Mathematical description

A comprehensive mathematical description of various SWI configurations, including SDM, is published in Chapter 5.1 and 5.2 of [168]. Here we consider the case of a simple interferometer based on a Mach-Zehnder geometry (Fig. 2.5). The output of the tunable laser is given as

$$E(t) = E_0 e^{-i\phi(t)} \hat{Q}, \tag{2.13}$$

where E_0 is a constant amplitude, $\hat{Q}$ is a unit polarization vector that is assumed to be constant throughout the laser sweep and $\phi(t)$ is the phase, which is related to the instantaneous frequency $\nu(t)$ of the laser as

$$\nu(t) = \frac{1}{2\pi} \frac{d\phi(t)}{dt}. \tag{2.14}$$

The instantaneous frequency $\nu(t)$ of the laser in the case of a linear frequency sweep is

$$\nu(t) = \nu_0 + \gamma t, \tag{2.15}$$

where γ is the sweep rate. Thus, by integrating (2.14), the phase is given by

$$\phi(t) = 2\pi(\nu_0 t + 0.5\gamma t^2). \tag{2.16}$$

The laser field $E(t)$ is split into two components $E(t - \tau_r)$ and $E(t - \tau_s)$ that propagate through different paths with the group delay times of the signals in the reference and sample arms τ_r and τ_s, respectively. For simplicity an equal splitting ratio is considered. When these two components of the optical field are recombined on a photodetector, interference results in a detector voltage given by

$$U(t) = |E(t-\tau_r) + E(t-\tau_s)|^2 \tag{2.17}$$

and the final result will be

$$U(t) = U_0(1 + \cos(2\pi\gamma t\tau_0 + \psi)), \tag{2.18}$$

where $\tau_0 = \tau_s - \tau_r$, U_0 is a constant that depends on the detector sensitivity and constant amplitude E_0, and ψ is a constant phase. The result can be interpreted as a sinusoidal output for a fixed-path-length interferometer and used for a further processing and extraction of the transfer function and impulse response. In SWI it is often more convenient to represent (2.18) as a function of the instantaneous optical frequency ν, rather than a function of time:

$$U(\nu) = U_0(1 + \cos(2\pi\nu\tau_0 + \xi)), \tag{2.19}$$

where $\xi = \psi - 2\pi\nu_0\tau_0$.

In case of nonlinear frequency tuning, (2.18) can be written in a more general form of

$$U(t) = U_0(1 + \cos(\phi(t) - \phi(t-\tau_0) + \psi)). \tag{2.20}$$

In [169] (2.20) is simplified by expanding $\phi(t-\tau_0)$ in a Taylor series and assuming that the instantaneous laser frequency does not change over a time interval equal to the relative delay between the interferometer arms. In this case the higher order terms in the expansion are negligible and

$$\phi(t-\tau_0) \approx 2\pi\nu(t)\tau_0, \tag{2.21}$$

so the phase difference is no longer an explicit function of time, but rather a function of the instantaneous optical frequency $\nu(t)$. After substitution of relation (2.21) in (2.20), an expression identical to (2.19) can be derived. However, in case of nonlinear tuning this equation must be applied carefully, since the fringe pattern is periodic in optical frequency, but may be aperiodical in time, whereas in the case of ideal linear tuning, the captured signal is periodic in both time and optical frequency.

Nonlinearity of the laser sweep and its tracking

As was mentioned in the previous section, the laser sweep is generally not perfectly linear. This leads to measurement errors and can artificially broaden the measured impulse response function of the DUT [169]. To overcome this issue, an auxiliary interferometer is usually introduced in the experimental setup, as indicated in Fig. 2.6(a). This interferometer assists in tracking the nonlinearity of the laser sweep, which can then be compensated [41, 169, 170]. One option is to linearize the nonlinear frequency sweep by extracting new sample points from the received signal of this additional interferometer. Another alternative is to use the auxiliary interferometer output as a clock signal to trigger the oscilloscope, which avoids the large number of interpolations required for resampling [171–173]. Using this signal as an external clock to sample the fringe pattern output by the measurement interferometer enables sampling at equal optical frequency steps $\Delta\nu_0 = 1/\tau_0$. This, however, is correct only when the instantaneous frequency of the laser does not change significantly over τ_0 (the slow tuning approximation criterion) [169]. Along with that, the trigger signal output can be used to measure the varying laser sweep rate throughout an acquisition, providing the sweep rate data required to perform the resampling.

Both approaches discussed above rely on the condition that the interferometer output signal is periodic in optical frequency. However, when the laser sweeping speed is high, the slow tuning approximation is not valid anymore. Usually such lasers have much larger nonlinearity of the sweep and one can face undesired variations in the sampling interval that arise when using a particular clock to trigger the sampling of an experimental data set. Such variations are referred as sampling errors in Ref [169].

All mentioned issues were alleviated after the development of DSP methods [168], but still lack absolute accuracy and suffer from a systematic error caused by a wavelength dependent fiber group delay. Owing to that, calibration of the delay arm and operation in a stable condition is required [171, 174]. Recently, a new approach was reported, where a FC can be used as a frequency "ruler" for such a calibration [175].

Experimental implementation

Figure 2.6(a) shows a general experimental setup for characterisation of photonic devices using SWI. A tunable laser sweeps across the mea-

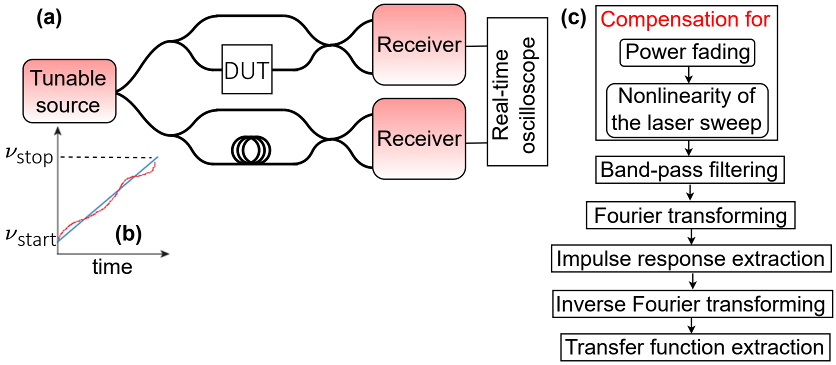

Figure 2.6: (a) Experimental setup for SWI implementation. (b) Principal sketch showing deviations (red) from the ideal linear dependence (blue) of laser's frequency on sweeping time. (c) DSP algorithm.

surement range and its output is split between an interferometer with a DUT and a reference interferometer assisting in tracking the nonlinearity of the laser tuning. Additional arms can be added to an experimental system for monitoring of power and polarisation fading. If the sweeping bandwidth is large enough, so that the laser experiences power fluctuations, it can assist in compensation for power fading during DSP. Finally, the signal is detected by receivers and digitized with an analog-to-digital converter (ADC).

Extraction of the transfer function and impulse response from the sampled photocurrents can be done with DSP steps shown in Fig. 2.6(c). The first DSP module is usually devoted to the compensation for the power fading and nonlinearity of the laser sweep [155]. Next, a band-pass filter is applied and the impulse response elements are found in the spectra obtained by Fourier transform at positions corresponding to fiber delays. Finally, the complex transfer function can be calculated with the inverse Fourier transform of all impulse response elements.

2.2.6 Comparison of SDM characterisation techniques

In the previous section, various measurement techniques for SDM characterisation were described and reviewed. All of them have their own advantages and limitations and can be applied in various situations, depending on purposes of measurement. Depending on the considered system, the performance parameters can also vary a lot and while some of the discussed methods are perfectly suitable for measurement of some devices, they can be inappropriate for others.

One important feature of SDM characterisation is that multiplexers at the input and demultiplexers at the output of the DUT should be included in the setup. Multiplexers and demultiplexers require fiber delays for separation of impulse responses from different cores in the time domain. If these delays are too large, it can be impossible to detect the transfer function from some of the fiber cores due to limited frequency resolution (limited range of time delays that can be captured by a specific measurement technique). Thus, a selection of fiber delays for a particular DUT should be made carefully.

S^2 imaging is capable of measurement of mode shapes and DGD extraction without any demultiplexer, while it requires a reasonably simple setup. However, even low amount of coupling between the modes becomes detrimental for signal analysis, which makes S^2 less suitable - or at least more complex - to characterise coupled SDM devices that have time-varying transfer functions. Moreover, the phase of the DUT is not measured in the simplest implementation of S^2 [143], making it impossible to extract a complex transfer function and calculate MDL. S^2 imaging can, however, be implemented inside a SWI, where the phase can be easily extracted [176].

In case of DH, with a setup similar to S^2, the reference beam is directed at an angle with respect to the signal, which may provide access to the phase information, even though the camera only records intensity. At the same time, DH possesses all the advantages of S^2 imaging, e.g, can assist in reconstruction of mode shapes.

The DCS is a powerful technique in terms of the resolution, measurement bandwidth and high sensitivity. Furthermore, DCS allows using both amplitude and phase information, making it possible to extract a complex transfer function of a DUT. DCS is also favorable for measurements of small dispersion values, which can be difficult to capture in short fibers [28, 164]. However, it has some limitations due to the discrete comb lines. Particularly, narrow band variations that fall between the comb lines or delays that are larger than the inverse repetition rate of the combs, cannot be measured using the DCS.

In SWI both amplitude and phase information is preserved, so the full complex transfer function can be extracted as well. Moreover, employing a tunable laser source enables achieving high SNR and spectral resolution. However, deviations from a linear frequency sweep and possible instability of the DUT during the sweep lead to measurement errors, which require a reference interferometer for monitoring and compensation. This complicates and increases the size of the setup. Implementation of SWI also requires a trade-off for sweeping speed and stability of the DUT.

With MIMO analysis, the equaliser taps can be used to approximate the transmission channel and estimate characteristics such as modal dispersion and MDL. However, in the presence of noise, MDL might be underestimated, which, though, can be corrected if the noise is known, as was performed in [177]. Another issue is that MIMO systems become impractical and costly for SDM-characterisation of fibers with the high number of modes.

The choice of an experimental technique for SDM characterisation is always a matter of trade-offs. The SWI and DCS enable capturing a full complex transfer function, but can not give the information about a mode shape that can be obtained from DH or S^2. Note that if the multiplexers and demultiplexers are used in the setup to handle the inputs and outputs of SDM fibers, measurement results will not correspond to the pure transfer function of the SDM fiber. The modes of the multiplexers are often different from those of transmission fibers and hence the issue is that using DCS or SWI it is not possible to measure SDM devices directly, but rather a concatenation of multiplexers, SDM device and demultiplexer. Hence, characterisation techniques that enable measurement of the optical field without demultiplexers are expected to provide more accurate results.

CHAPTER 3

Dual-Comb Swept-Wavelength Interferometry

This chapter expands the results published in [Paper A], [Paper B] and presents an experimental technique which combines dual-comb spectroscopy (DCS) and swept-wavelength interferometry (SWI) for photonic devices characterisation. The main concepts of dual-comb swept-wavelength interferometry (DC-SWI), its experimental implementation, DSP and measurement results are discussed in the following.

3.1 Principle

In the previous chapter DCS and SWI were described. DC-SWI, is a combination of these two techniques (Fig. 3.1). Similar to DCS, DC-SWI uses two FCs with repetition rates f_{r_1} and f_{r_2}, but instead of a fixed wavelength laser a swept laser acts as the seed laser to both combs. Therefore, the technique is able to measure the full optical bandwidth of the combs including the intermediate frequencies between comb lines. In contrast to SWI, the laser is not swept over the large bandwidth, but only covers the frequency range that corresponds to a repetition rate of the frequency comb. In principle, this corresponds to a set of coherent SWIs defined by the number of comb lines K. This practically increases the measurement speed K times compared to classic SWI and, compared to the DCS, provides better frequency resolution as it is set by the capture time of the digitizer, not the comb spacing. Moreover,

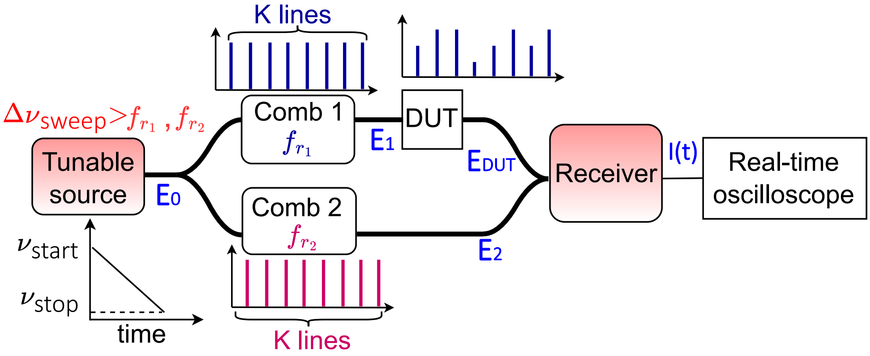

Figure 3.1: Principle of DC-SWI.

as the measurement trace corresponds to multiple parallel SWIs that experience the same laser sweep, we can take advantage of this to eliminate the sweep nonlinearity directly from the measurement without an external calibration interferometer. It can be a beneficial point since, as discussed in sections 2.2.5 and 2.2.6, the process of monitoring the laser's sweep nonlinearity and its compensation can be challenging and increases complexity.

There are additional details that have to be taken into account. First, it is important to operate with a sweeping bandwidth $\Delta\nu_{sweep} = \nu_{start} - \nu_{stop}$ larger than the frequency comb spacing in order to have an overlap between the detected spectral windows, so the transfer functions from neighboring lines can be coherently stitched at the DSP stage [178]. Similarly to static DCS, the number of comb lines K and spacing Δf_r limit the choice of sampling rate f_s, which should be no less than $K\Delta f_r$ in order to resolve all necessary spectral lines. At the same time, the number of samples N should reflect the sweeping time as $N = f_s t_{sweep}$, which determines the necessary memory of the digitizer in order to capture the whole interferogram, as was discussed in section 2.2.5.

3.2 Mathematical description

The output electrical field of a frequency sweeping source in single polarization case can be expressed as

$$E_0(t) = A \cdot e^{-i\phi(t)}, \tag{3.1}$$

where A is the constant amplitude of the field, $\phi(t)$ is the time-dependent phase connected with an instantaneous frequency $\nu(t)$ of the laser by (2.14). Similar to the case of SWI, the phase in case of linear wavelength tuning can be expressed by (2.16). However, as was mentioned in section 2.2.5, the laser sweep is never linear in practice and this can be accounted by adding a nonlinearity term in (2.15). Alternatively, the phase in (3.1) can be represented by linear and nonlinear components of the laser sweep as $\phi(t) = \phi_{Lin}(t) + \phi_{NL}(t)$.

After generating a comb with a repetition rate f_{r_1} from the swept laser the field becomes

$$E_1(t) = E_0(t) \sum_{k=0}^{K-1} e^{-2\pi i t \cdot k f_{r_1}}, \tag{3.2}$$

where $k = 0...K-1$ is the comb line number. Here we ignore the phase profile across the comb and assume for simplicity that the modulation introduces sidebands with equal power. The second comb with the repetition rate $f_{r_2} = f_{r_1} + \Delta f_r$ is

$$E_2(t) = E_0(t) \sum_{k=0}^{K-1} e^{-2\pi i t \cdot k (f_{r_1} + \Delta f_r)}. \tag{3.3}$$

The output field of the comb that passes through the DUT (assumed to be $E_1(t)$, without loss of generality), becomes the convolution of $E_1(t)$ with time-domain response of the DUT $h(t)$:

$$E_{DUT}(t) = E_1(t) * h(t). \tag{3.4}$$

For simplicity we limit the mathematical description to balanced detection, however, the technique is applied equally to the case when a coherent detector is used. The fields $E_1(t)$ and $E_{DUT}(t)$ beat on a balanced photodetector and the output photocurrent is given by:

$$I(t) = 2R \cdot Re\{E_{DUT}(t) E_2^{\dagger}(t)\}, \tag{3.5}$$

where R is the responsivity of the detector and $E_2^{\dagger}(t)$ is complex conjugate of the field $E_2(t)$.

In the ideal, linear-sweep case, (3.5) can be written as

$$I(t) \sim \sum_{k=0}^{K-1} \tilde{h}_k(t) e^{-2\pi i t \cdot k \Delta f_r}, \tag{3.6}$$

where $\tilde{h}_k(t)$ is the impulse response of the k-th comb line. In the frequency domain this will give

$$I(\omega) \sim \sum_{k=0}^{K-1} h_k(\omega - 2\pi k \Delta f_r) \tag{3.7}$$

which is a set of K impulse responses, where each impulse response is centered at a different optical frequency $\omega - 2\pi k \Delta f_r$.

If $h(t)$ is assumed to be a simple delay, so that $h(t) = \delta(t - T)$ and $E_{DUT}(t) = E_1(t - T)$ and nonlinearity of the laser sweep is taken into account as $\phi(t) = 2\pi(\nu_0 t + 0.5\gamma t^2) + \phi_{NL}(t)$, then (3.5) can be written as

$$\begin{aligned} I(t) = 2R \cdot Re\{Ae^{-i(2\pi\nu_0(t-T)+\pi\gamma(t-T)^2+\phi_{NL}(t-T))} \times \\ \times (\sum_{k=0}^{K-1} e^{-2\pi i(t-T)\cdot k f_{r_1}}) \times \\ Ae^{i(2\pi\nu_0 t+\pi\gamma t^2+\phi_{NL}(t))}(\sum_{k=0}^{K-1} e^{2\pi i t\cdot k(f_{r_1}+\Delta f_r)})\} \end{aligned} \tag{3.8}$$

and by taking the real part, the final expression for the photocurrent becomes

$$\begin{aligned} I(t) = 2R \cdot A^2 \sum_{k=0}^{K-1} \cos(2\pi(T\nu_0 - 0.5\gamma T^2 + Tkf_{r_1} + \\ + tk\Delta f_r + tT\gamma) + \phi_{NL}(t) - \phi_{NL}(t-T)). \end{aligned} \tag{3.9}$$

When nonlinearity of the laser tuning is negligible, the term $\phi_{NL}(t) - \phi_{NL}(t - T)$ will vanish. Moreover, one can neglect the constant terms independent of t and k and (3.9) can be simplified as

$$I(t) = 2R \cdot A^2 \sum_{k=0}^{K-1} \cos\left(2\pi(Tkf_{r_1} + tk\Delta f_r + tT\gamma)\right). \tag{3.10}$$

If the signal is sampled in time intervals Δt as $t = n\Delta t$, where $n = 1...N$ is the sample number and Δt is inverse to the sampling rate $f_s \geq K\Delta f_r$, (3.10) can be expressed as

$$I(n) = 2R \cdot A^2 \sum_{k=0}^{K-1} \cos\left(2\pi\left(Tkf_{r_1} + \frac{kn}{K} + n\Delta t T\gamma\right)\right), \tag{3.11}$$

which shows that the detected photocurrent contains K terms oscillating at different frequencies depending on comb line number k, and given by $k/K + T\gamma$ and offset in phase by Tkf_{r_1}. This generalizes the SWI result which is oscillations at frequency γT.

3.3 Experimental implementation

The experimental setup used in [Paper A] and [Paper B] is shown in Fig. 3.2. Two electro-optic FCs with 25.05 and 25.15 GHz repetition rates and 12 nm bandwidth (55 lines) each were used. The combs were configured with two phase modulators and one intensity modulator, with the arrangement described in detail in [165]. An Agilent laser acted as the seed, and swept over a 25.4 GHz bandwidth in 5 ms. The laser was preamplied before the comb generation to increase the comb power and thus the SNR of the DC-SWI system. A 25 MHz acousto-optic modulator was added for shifting away the downconverted center line of the comb from DC [165], which can be omitted when using a coherent receiver. A 25.15 GHz comb went through the DUT and 25.05 GHz comb acted as the local oscillator. The optical field was measured with a Finisar 25 GHz coherent receiver and digitized at 6.25 GS/s by Tektronix DSA 71604 real-time oscilloscope. The sampling clock of the oscilloscope was locked to the 100 MHz beat-signal of the comb clocks [165], as indicated by the dashed lines in Fig. 3.2. The oscilloscope is triggered by the sweeping laser to ensure that a measurement starts simultaneously with the sweep start.

Similar to DCS, DC-SWI requires a calibration process before measurements. Hence, to obtain a correct device characterisation, a measurement without the DUT has to be performed and then subtracted from the one with the DUT during the DSP.

The setup is flexible with respect to experimental additions. For instance, if the sweeping bandwidth is large enough, so the laser experiences power fluctuations, a power monitoring arm can be included, the data from which can assist in power calibration during the DSP. In our experiments it was not strictly necessary since the sweeping bandwidth, which reflects the repetition rate of the FCs, was small and there were no significant fluctuations in the power level during the sweep. Additionally, an auxiliary interferometer can be used for a comparison of the performance when different algorithms for laser sweep nonlinearity compensation are applied.

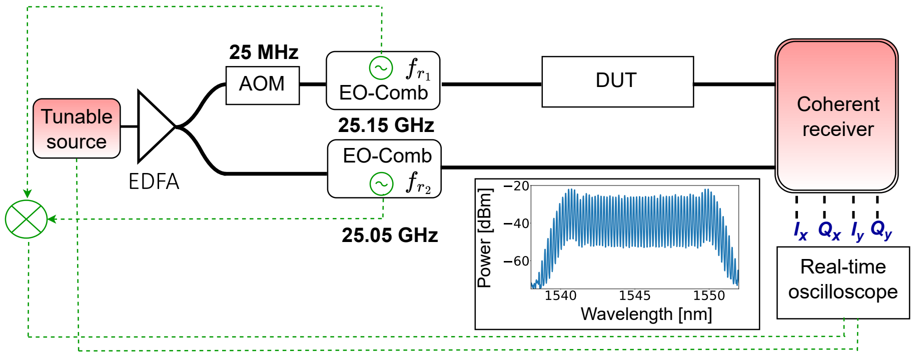

Figure 3.2: Experimental setup for characterisation measurements with DC-SWI. The black and green lines relate to optical and RF connections respectively. EDFA: erbium doped fiber amplifier, AOM: acousto-optic modulator, EO-comb: electro-optic frequency comb, DUT: device under test. Inset: Optical spectrum of the frequency comb with a frequency spacing of 25.15 GHz.

3.4 Digital signal processing

The signal processing is extensively presented in the DSP section of [Paper B] and the reader is refereed to this paper for more details. The DSP algorithm flow is shown in Fig. 3.3. It consists of several steps that resemble a combination of signal processing used for SWI and DCS.

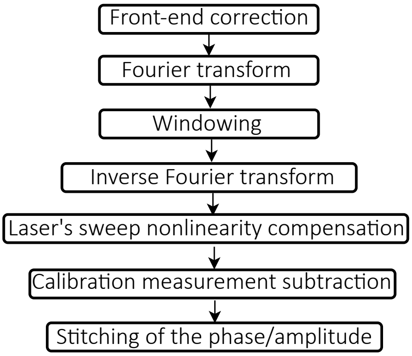

Figure 3.3: DC-SWI DSP flow.

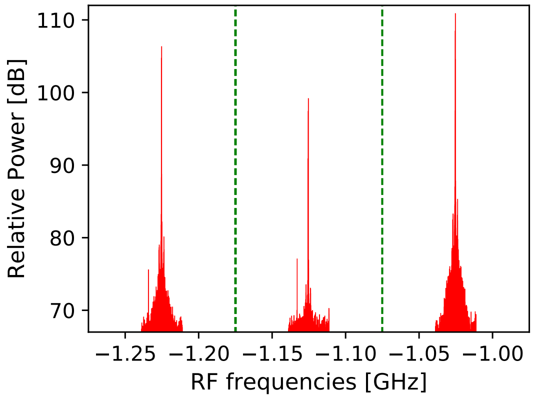

Figure 3.4: Zoomed-in image of the 12th, 13th and 14th comb lines after performing the windowing with selected bandwidth of 4 MHz. Vertical lines indicate the borders corresponding to 100 MHz spacing between the spectral lines.

3.4.1 Front-end correction and windowing

First, the raw measured signal is orthonormalized in order to make I and Q components strictly perpendicular. Note that this step is not necessary in the case when a heterodyne receiver is used, since there will be no 90-degree skew issues between I and Q components.

Second, a Fourier transform of the same length as the received data $I(n)$ is applied to the signal and the scan of each comb line is selected by band-pass filtering, producing parallel SWI scans, the amount of which is equivalent to the number of comb lines K. The performance of the measurement can be adjusted by this digital filtering, which yields an SNR vs frequency resolution trade-off, an aspect further discussed in Section 3.6. After the filtering procedure, the response windows are transformed back to the time domain. Fig. 3.4 demonstrates an example for this filtering for three comb lines with a filtering bandwidth of 4 MHz.

3.4.2 Laser's sweep nonlinearity compensation

The next step is to compensate for the laser's sweep nonlinearity in every comb window. This nonlinearity is extracted from the measured phases in every comb window that can be written as

$$\phi_k(t) = \phi_{Lin}(t) + \phi_{NL}(t) + \psi_k(t), \tag{3.12}$$

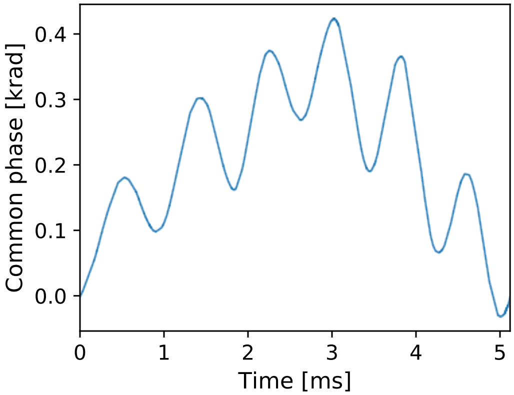

Figure 3.5: Common phase calculated from (3.13) with averaging over 45 comb windows.

where $\phi_{Lin}(t)$, $\phi_{NL}(t)$ are the linear and nonlinear parts of the laser's sweep, $\psi_k(t)$ accounts for a phase response of the DUT at different frequencies. The laser's phase component is the same for all the comb lines, which is why it is not indexed, whereas the phase responses of a DUT depend on wavelength and can be different in every comb window. The terms $\phi_{Lin}(t)$ and $\phi_{NL}(t)$ are the contributions that need to be calculated and removed from the complex signal to compensate for the laser's sweep nonlinearity. This can be done by transforming $\phi_k(t)$ in two steps. First, the term $\phi_{Lin}(t)$ should be removed by calculating and subtracting the average slope of the phases $\phi_k(t)$ with the derivative or fitting procedure. Next, the averaging of $\phi_{NL}(t)+\psi_k(t)$ over all K lines enables extraction of the common phase

$$\overline{\phi_k(t)} = \phi_{com}(t) = \phi_{NL}(t) + \frac{1}{K}\sum_{k=0}^{K-1}\psi_k(t). \tag{3.13}$$

As can be seen, when the second term in (3.13) is negligible relative to the first one, this common phase corresponds to the nonlinearity of the laser sweep $\phi_{NL}(t)$. This common phase is shown in Fig. 3.5. Moreover, as was discussed in [Paper B], even if the number of the comb lines K is small, the nonlinear phase component of the laser $\phi_{NL}(t)$ will be the dominant term in (3.13). Therefore, the nonlinear component of the sweep is defined by the common phase $\phi_{com}(t)$, which can then be subtracted from the measurement signal, alleviating the use of an additional interferometer in the setup to extract the nonlinearity of the frequency sweep.

The compensation procedure is flexible and can be performed using a common phase calculated only from a part of measured spectral windows or a set of particular windows if the measured DUT has drastic changes in particular comb scans. As an example of such selection, Fig. 3.7(c) demonstrates calculated phase profiles of a 22 m SMF. These curves are extracted from the same measurement, but using different number of spectral windows during nonlinearity compensation. The results are further discussed in section 3.5.1. After the compensation, calibration of each line with respect to measurement without a DUT is performed.

3.4.3 Stitching of the amplitudes and phases

Finally, all K traces have to be stitched via the overlap regions in order to produce the broadband full-field transfer function. Stitching of the amplitudes and phases is carried out in a similar way and schematically shown in Fig. 3.6 for two neighboring phases that have the overlap regions ϕ_k^{over} and ϕ_{k+1}^{over} (inset in Fig. 3.6 (a)). In [Paper B] the stitching procedure was carried out through moving the subsequent phases with respect to each other on the level difference Δ. These phases were averaged and subtracted to find the difference between them:

$$\Delta\phi = \overline{\phi_k^{over}} - \overline{\phi_{k+1}^{over}}. \tag{3.14}$$

The subsequent phase ϕ_{k+1} was then moved by $\Delta\phi$ with respect to ϕ_k. This can be written as

$$\phi_{k+1}^{new} = \phi_{k+1} + \Delta\phi. \tag{3.15}$$

Finally, the phase arrays have to be stitched with each other in the overlap point. The resulting phase array is demonstrated in Fig. 3.6 (b). This procedure, though, can be easily done by stitching the phases/amplitudes straightaway in the overlap point.

The stitching procedure, however, can be tricky. The main issue relates to the uncertainty of the level difference calculation when phases or amplitudes traces have different magnitude in neighboring spectral windows. This usually happens when stitching neighboring phases with the one at the edges of the bandwidth because the comb lines there have lower SNR, and thus, more noise. To avoid errors during the stitching one can vary the window where the stitching procedure starts or filter out the noise before the procedure. Another important detail for stitching is

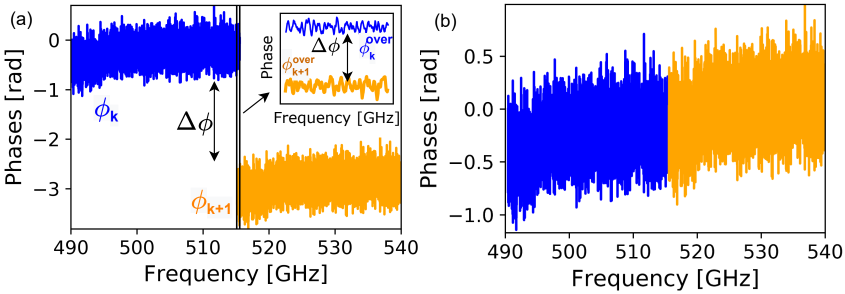

Figure 3.6: (a) Phases from two neighboring comb windows. Inset: overlap region. (b) Result of the phase stitching: phase ϕ_{k+1} is moved up on $\Delta\phi$.

the number of points in the overlap region. One can try to increase the sweeping bandwidth in order to make an overlap between the comb cans larger, which can also improve the stitching.

3.5 Experimental results

In [Paper B] several measurements using applied filters on a Finisar 1000S Waveshaper were shown in order to demonstrate the capabilities of the proposed technique. In this section characterisations of the transfer function obtained using DC-SWI for SMF and 3CCF are presented.

3.5.1 Characterisation of a SMF

As a first example, a simple measurement of a 22 m SMF is presented. The experimental setup described in section 3.3 was used for the characterisation.

Figure 3.7 shows the amplitude (a) and the phase (b) of the transfer function of the 22 m SMF. The amplitude profile is constant, as expected, while exhibits noise fluctuations about 1 dB due to limited SNR. The phase profile is a parabolic function, from which the quadratic dispersion β_2 parameter can be extracted as β_2 = -21.14 ps^2/km at λ = 1545 nm, which agrees well with the β_2 expectations for SMFs.

Fig. 3.7(c) shows several phase curves that are calculated with slightly different compensation of the laser sweep nonlinearity. Different colors indicate how many comb line windows K were used for calculation of the common phase. It can be seen that the resulted phase profiles are very similar and β_2 parameters for all the cases are in a good agreement

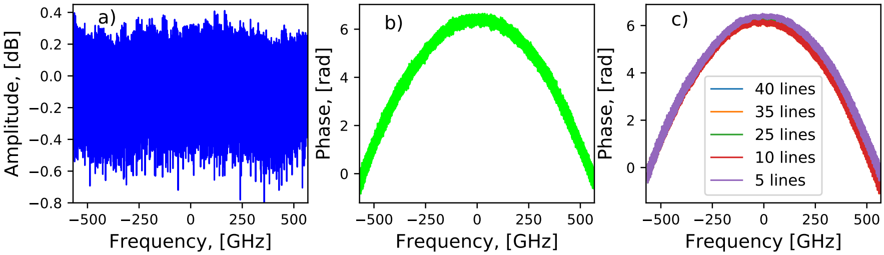

Figure 3.7: Stitched (a) amplitudes and (b) phases of the transfer function of SMF extracted from 45 comb lines. (c) Phase profiles obtained after the subtraction of the common phase calculated by averaging nonlinear laser phase components from the different number of windows.

with the one calculated for the case when all the comb windows phases were used for averaging (Fig. 3.7(b)). This result points out that during the DSP a flexible selection of comb spectral windows for common phase calculation can be performed.

3.5.2 Characterisation of three coupled-core fiber (3CCF)

In this section characterisation results of a 1.6 km 3CCF manufactured by Sumitomo Electric Industries are shown and discussed. These findings are mainly summaries of [Paper A] and more details can be found there.

The experimental setup for 3CCF characterisation is the same as demonstrated in Fig. 3.2 with addition of fan-in/out devices for coupling the light into the cores of the 3CCF and handle outputs from multiple cores. The fan-in/out devices are based on ultrafast laser-inscribed 3D waveguides in a boro-aluminosilicate glass [179]. We also added delay fibers of 20 and 40 m at the output of the 3CCF in order to separate impulse responses of different cores in the time domain. The length of these delays was chosen to be larger than the impulse response of a single core of the 3CCF. All 3 outputs of the 3CCF were then combined using 3-dB couplers and sent to a coherent receiver.

Figure 3.8 shows the magnitude of the 3CCF's transfer function over 1.1 THz comb bandwidth. The illustrated data is calculated as a sum of magnitudes of the respective X- and Y-polarizations and normalized by the total power from all the cores. Each plot corresponds to a different input fiber core. For all inputs, around 10 dB variations in maximum/minimum transmission is observed. Core 2 has a slightly higher

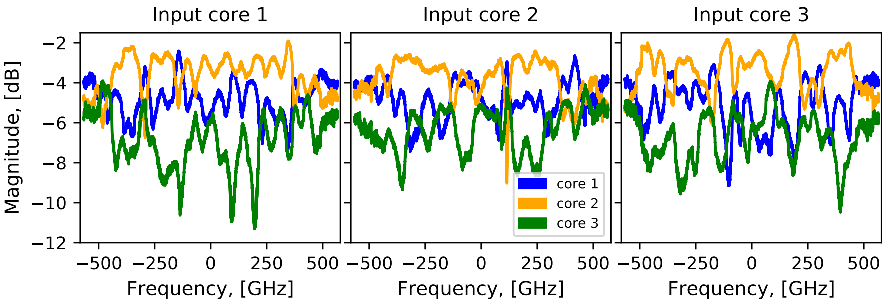

Figure 3.8: Stitched magnitudes of the transfer function extracted from 45 comb lines with light entering the different cores.

power than the other cores, which is likely due to different losses in the fan in/out devices.

Figure 3.9 represents the total power impulse responses for each fiber input core calculated as a sum of impulse responses corresponding to output cores and then normalized by its maximum value. Possible reasons for a noisy behavior (fluctuations as a function of frequency) of the curves are reflections from fan in/out connectors or discrepancies in the phase stitching. Using values of estimated RMS widths of the impulse responses, $T_{RMS_1} = 18.9$ ps, $T_{RMS_2} = 18.6$ ps and $T_{RMS_3} = 18.5$ ps, DMGD of every fiber core can be calculated as $DMGD_i = T_{RMS_i}/\sqrt{L}$, where L is a fiber length and i is a fiber core number. Corresponding DMGDs are $\mathrm{DMGD}_1 = 14.94$ ps$/\sqrt{\mathrm{km}}$, $\mathrm{DMGD}_2 = 14.65$ ps$/\sqrt{\mathrm{km}}$ and $\mathrm{DMGD}_3 = 14.62$ ps$/\sqrt{\mathrm{km}}$, which are in a good agreement with properties of the CCFs that were published in [180]. These results are also consistent with previously reported values of DMGD for the 3CCF [181] and other CCFs [182].

Note that the elements of the transfer matrix were not measured simultaneously. An optical switch was used to select input core of the 3CCF during the experiment, so only 3 elements were captured per measurement shot. Input core delays can be added to enable a single-shot measurement of all inputs and outputs and this is a possible future extension of this experiment.

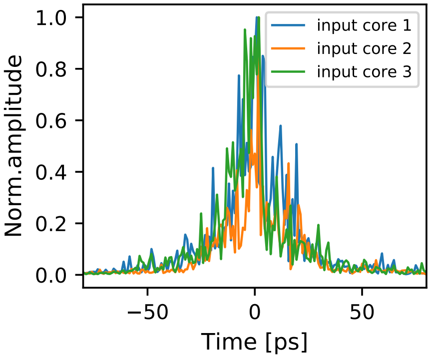

Figure 3.9: Total power impulse responses of a 1.6 km 3CCF.

3.6 Discussion of performance

In this section performance characteristics, different trade-offs and competitive sides of DC-SWI are discussed.

3.6.1 Time resolution

Assuming perfect stitching and compensation for sweep nonlinearity, the time resolution, or minimum time delay δt that can be measured in DC-SWI is the inverse comb bandwidth $\Delta\nu$:

$$\delta t = \frac{1}{\Delta\nu}. \tag{3.16}$$

The comb bandwidth $\Delta\nu$, in turn, relates to the number of used spectral lines and a comb repetition rate as $\Delta\nu = Kf_r$. Consequently, employing broader FCs improves the temporal resolution.

In the presented setup 50 comb lines with 25.15 GHz repetition rate were used, so the time resolution can be estimated as $\delta t \approx 0.8$ ps. This time resolution also can be reached using a static DCS or conventional SWI, since the bandwidth $\Delta\nu$ in (3.16) will be the same.

3.6.2 SNR and the frequency resolution

SNR is one of the most important parameters in optical communication systems. As was discussed in [183], in DCS-based measurement schemes SNR scales per spectral line of the comb as $1/K$, while the shot-noise limited SNR in SWI will be defined only by the output power of the tunable source and the bandwidth of the detector [184]. In DC-SWI a flexible trade-off between SNR and spectral resolution is possible at the windowing stage of DSP: by selecting the desired interval around responses and cutting off unnecessary frequencies, SNR can be increased. The SNR, however, can significantly degrade when SDM devices with high core count are characterised since the number of measurement channels is increased. An appropriate choice of the power coupling ratio between reference and DUT arms of the measurement interferometer should then be considered.

The frequency resolution is the minimum frequency difference between two distinct transfer function features one can distinguish. It is related to the longest delay that can be measured. In DC-SWI experiment the frequency resolution can be selected by bandpass filtering around the individual spectral line of the RF comb in the DSP. In this windowing process the number of points m may decrease if only a part of the spectral window is kept, depending on the width of the impulse response. It can then be defined more generally as

$$\delta\nu = \frac{\Delta\nu}{K \cdot m} = \frac{K \cdot f_r}{K \cdot m} = \frac{f_r}{m}. \tag{3.17}$$

This value can be then used to calculate maximum delay time that is possible to measure, which is the inverse frequency resolution:

$$\delta T = \frac{1}{\delta\nu}. \tag{3.18}$$

In all experiments presented in this thesis, one comb line scan contained 511 998 points before windowing, so the best possible frequency resolution was $\delta\nu = 49.121$ kHz and the maximum delay time is 20.4 μs. Hence, the presented setup is capable of characterisation of DUTs with delays range from 0.8 ps to 20.4 μs, which is a benefit of DC-SWI because, as was pointed out in section 2.2.6, the spectral resolution in static DCS techniques is limited and measuring long delays can therefore be challenging.

A key advantage of DC-SWI is that one can more easily decide which trade-offs are desired during the experiment and DSP. Different comb sources and tunable lasers with various speed can be used, which also influence the capabilities of the setup and ultimate performance of the system.

CHAPTER 4

Channel models

The transfer matrix characterisation can assist not only in gaining important information about optical fibers, but also in building channel models that realistically describe their properties. A channel model can be defined as an input-output model for a given signal and is useful for estimating the transmission system performance (i.e. channel capacity) and optimising system parameters. The purpose of modeling is often seen as creating a strategy for simulating a transfer function of a fiber because the transfer function can be used to extract all parameters of the system under study. Channel models also assist in developing and testing modulation formats, efficient transmission and detection schemes as well as in the design of photonic devices.

This chapter starts from a short review of channel models for fiber optic communication and then provides a theoretical description of the proposed linear channel models for CCFs and examples of the simulation results for a 3CCF and 4CCFs. These channel models include deterministic static models for ideal CCFs and random coupling models, where the frequency dependence of the coupling coefficients and time-drift effects are taken into account.

4.1 Overview of Gaussian noise channel models

The NLSE is the principal equation describing how the propagation is guided in the optical fibers. As was mentioned in the previous chapters, it is a time-dependent nonlinear differential partial equation, which cannot be solved analytically in the general case. The split-step Fourier method [66] is used to solve it numerically by dividing a fiber into short pieces, such that linear and nonlinear impairments can be applied separately. The situation becomes much more complicated when SDM fibers are investigated since one has to consider a set of coupled NLSEs that include random mode/core coupling and random phase noise from the channels. In optical communication, discrete-time channel models for which the channel output is an explicit function of the channel input are desirable to use. Such information-theory friendly channel models are reviewed in [87] and in the following subsections two most commonly used models for fiber optic communication systems are described.

4.1.1 The additive white Gaussian noise model

The additive white Gaussian noise (AWGN) channel is the simplest model, which states that the output signal $\mathbf{Y}$ is defined by the input signal $\mathbf{X}$ and the random vector $\mathbf{Z}$ as

$$\mathbf{Y} = \mathbf{X} + \mathbf{Z}, \tag{4.1}$$

where $\mathbf{Z}$ is a circularly symmetric, complex, white, Gaussian random sequence, independent of $\mathbf{X}$. Input $\mathbf{X}$ contains independent identically distributed (i.i.d.) symbols, drawn from the same constellation, and have a given average transmitted power. From the equation above it can be seen why the model is called *additive* - this is because the received signal $\mathbf{Y}$ is equal to the sum of transmitted signal $\mathbf{X}$ and noise $\mathbf{Z}$. *White* refers to the idea that the noise has uniform power spectral density across the whole frequency band for the information system. It is an analogy to the white color, which is composed of all frequencies in the visible spectrum. Lastly, it is *Gaussian* since it has a normal distribution in the time domain with an average time domain value of zero.

The AWGN channel is accurate for modeling the back-to-back case in fiber optic communications. Even if this model does not consider other phenomena except AWGN, analyzing the performance assuming the AWGN model can provide insights for the system design. Moreover, its simplicity and control capabilities allow deriving theoretical performance limits. The AWGN model is also reliable when the amplified spontaneous emission (ASE) noise is the dominant impairment in the system, or if the other impairments can be compensated with DSP. Hence, the AWGN channel is a very popular model for design and test of fiber optic systems, including SDM fibers.

4.1.2 The Gaussian noise model

In fiber optic links where the accumulated dispersion is large and nonlinear effects are weak, the joint effect of GVD and the Kerr effect can be approximated by additive Gaussian noise [185]. Such systems can be described through the Gaussian noise model, which belongs to the family of AWGN channels. The additive noise $\mathbf{Z}$ in this case is given as

$$\mathbf{Z} = \tilde{\mathbf{Z}}\sqrt{P_{ASE} + \eta P^3}, \tag{4.2}$$

where $\tilde{\mathbf{Z}}$ are i.i.d. zero-mean unit-variance circularly symmetric complex Gaussian random variables, P_{ASE} and η are real, non-negative constants, and $P = \mathbb{E}[[X]^2]$ is the average transmitted power. The value P_{ASE} represents the total ASE noise of the optical amplifiers for the investigated channel and η quantifies the nonlinear interference. Several expressions for η coefficient have been proposed. For example, [185] gives the equation for η in case of distributed amplification and wavelength-division multiplexed signals. Ref. [186] provides the expression in case of dual polarization and single channel transmission over several lumped amplifier spans.

It has been shown that the Gaussian noise model is conservative, as it overestimates the nonlinear interference power [121], however, it is a convenient tool for predicting system performance. Its prediction accuracy depends on system parameters and has been validated through both simulation [121] and experiments [187]. As the nonlinear interference noise depends on the transmitted modulation format [188], the enhanced, ergodic Gaussian noise model [189] was proposed. This ergodic Gaussian noise model takes into account the dependency of the nonlinear interference power on different modulation formats and was then also developed for SDM fibers in [123].

4.2 Deterministic static models

Modeling of CCFs has to take into consideration the principal phenomenon in such fibers - coupling between the cores/modes. When designing a model, it is always useful to have a benchmark by investigating an ideal, unperturbed fiber. This model is referred as deterministic in this thesis. Deterministic static models are based on the assumption that mode coupling is constant over time and describe SDM fibers without perturbations. These models usually apply CMT [96] for characterising coupling effects and other parameters in SDM fibers. Moreover, using this approach it is possible to analyse supermodes [101, 190], which can be described as a superposition of modes from isolated cores. This is an important aspect of studies since the supermodes, being spatial eigenmodes, propagate without shape distortion in an unperturbed fiber.

Some of the most important works that have been done on supermodes are mentioned in Section 1.2.2. One of the aspects that was absent in these works is a consideration of the polarization. CMT-based deterministic static models accounting for polarization multiplexing were proposed in [Paper C] for a 3CCF and in [Paper D] for a 4CCF. This type of the model is referred as the vector model, while the former case, where the polarization of the modes was disregarded, is referred as the scalar model. As both scalar and vector models were presented in [Paper C] and [Paper D], the aim of this section is to summarize and extend the theory provided in the papers, and give a comprehensive analytical derivation of expressions for the supermodes and their propagation constants in a 3CCF and 4CCF in terms of scalar and vector models.

Supermodes $\vec{s}_k$ and their propagation constants β_{s_k} strongly depend on the core count D, geometry and the refractive indices of the core n_1 and the cladding n_2 of the studied fiber. In general, the calculation algorithm always starts from defining the $D \times D$ ($2D \times 2D$ in the vector case) frequency-dependent coupling matrix $\mathbf{M}(\omega)$, which describes the coupling between the cores/modes. To build this matrix, one needs to calculate its elements - the coupling coefficients, which depend on the fiber geometry and frequency. When dealing with the vector model, it is also necessary to take into account the birefringence. Once the coupling matrix is found, the supermodes and their propagation constants can be calculated as eigenvectors and eigenvalues of $\mathbf{M}(\omega)$. The algorithm at the end of this section summarizes all the steps for calculations, while the following subsections provide more details on every step.

(a)

	core 1	core 2	core 3	...	core D
core 1	β	c_{12}	c_{13}	...	c_{1D}
core 2	c_{21}	β	c_{23}	...	c_{2D}
core 3	c_{31}	c_{32}	β	...	c_{3D}
...	...	...	...	...	...
core D	c_{D1}	c_{D2}	c_{D3}	...	β

(b)

	core 1	core 2	core 3	...	core D
core 1	B_1	C_{12}	C_{13}	...	C_{1D}
core 2	C_{21}	B_2	C_{23}	...	C_{2D}
core 3	C_{31}	C_{32}	B_3	...	C_{3D}
...	...	...	...	...	...
core D	C_{D1}	C_{D2}	C_{D3}	...	B_D

Figure 4.1: A structure of the coupling matrix in (a) scalar and (b) vector cases. In the scalar case, the interaction between the cores is described by the coupling coefficients c_{pq}, while in the vector case it is described by 2×2 matrices $\mathbf{C}_{pq}$ describing the coupling between the mode's polarizations.

4.2.1 Coupling matrix and coupling coefficients

In CMT, mode coupling along a fiber with multiple cores/modes in the scalar case is described by the following equation [101]:

$$\frac{d}{dz}\vec{A} = -j\vec{A}\mathbf{M}, \tag{4.3}$$

where $\vec{A} = [A_1, ..., A_D]$ is the modal amplitude vector and $\mathbf{M}$ is a $D \times D$ coupling matrix, which contains propagation constants of the single mode β and coefficients c_{pq} defining the mode coupling from the p^{th} core/mode to the q^{th} core/mode, where $p, q = 1...D$. A structure of such coupling matrix $\mathbf{M}$ is shown in Fig. 4.1(a). Note that the coupling matrix will strongly depend on the chosen core enumeration and if the way of enumeration is changed, the coupling coefficients can change their places in the matrix. In case of the vector model, when polarization of the modes is taken into account, the modal amplitude vector will be of the form $\vec{A} = [A_{1_x}, A_{1_y}, ..., A_{D_x}, A_{D_y}]$ and every coupling coefficient will be substituted by 2×2 matrix describing the coupling between the modes' polarizations as well. Most importantly, one has to take into account the birefringence described by the matrices $\mathbf{B}_p$, which is discussed in Section 4.2.2. The resulting coupling matrix $\mathbf{M}$ will have $2D \times 2D$ dimensions (Fig. 4.1(b)).

In the simplest case the coupling of p^{th} core/mode to the q^{th} core/mode

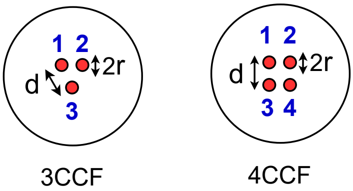

Figure 4.2: Geometry of the modeled 3CCF and 4CCF. Here d is the core pitch, r is the core radius. Enumeration of the cores are indicated by blue numbers.

is identical to the inverse coupling, so $c_{pq} = c_{qp}$. Assuming a step-index fiber and the weakly-guiding approximation, the coupling coefficients can be written as [96]

$$c_{pq} = \sqrt{\frac{n_1^2 - n_2^2}{n_1^2}} \cdot \frac{1}{r} \cdot \frac{U^2}{V^3} \frac{K_0(Wd/r)}{K_1^2(W)}, \tag{4.4}$$

where r is the core radius, d is a core pitch, K_0 and K_1 are the modified Bessel functions of the second kind of order 0 and 1 and V is the normalized frequency given by

$$V = \frac{2\pi r}{\lambda_0}\sqrt{n_1^2 - n_2^2}. \tag{4.5}$$

The refractive index for the core n_1 is obtained from the Sellmeier equation for fused silica [191]. The refractive index function for the cladding n_2 can be calculated using the refractive index difference Δ as $n_2 = n_1(1-\Delta)$. For a given V, the parameters U and W can be found by solving the equation system

$$\begin{cases} U \cdot K_0(W)J_1(U) = W \cdot K_1(W)J_0(U) \\ U^2 + W^2 = V^2 \end{cases}, \tag{4.6}$$

where $J_0(U)$ and $J_1(U)$ are the Bessel functions of the first kind of orders 0 and 1. The solution of the equation system can be efficiently found using the *fsolve* function of the scipy.optimize module in Python (see the supplementary materials with the codes in Ref. [28] of [Paper C]) or with other root solvers. As coupling coefficients depend on the V parameter, they are frequency dependent, $c_{pq}(\omega)$. Further in the text they will be denoted as c_{pq} and the frequency dependence sign will be omitted for simplicity.

Table 4.1: Parameters of the 3CCF and the 4CCF with the structure shown in Fig. 4.2.

	3CCF [Paper A, C]	4CCF-1 [Paper D]	4CCF-2 [Paper F], [113]
Core radii r [μm]	4.75	4.75	4.75
Core pitch d [μm]	22.5	22.5	25.4
Index difference Δ [%]	0.44	0.44	0.44
Fiber length L [km]	1.6	-	69.2

Table 4.2: Coupling matrices derived in case of the scalar model for the 3CCF and the 4CCF with the geometry shown in Fig. 4.2.

	3CCF	4CCF
Coupling matrices	$\begin{pmatrix} \beta & c & c \\ c & \beta & c \\ c & c & \beta \end{pmatrix}$	$\begin{pmatrix} \beta & c_1 & c_1 & c_2 \\ c_1 & \beta & c_2 & c_1 \\ c_1 & c_2 & \beta & c_1 \\ c_2 & c_1 & c_1 & \beta \end{pmatrix}$

In [Paper C] and [Paper D] we studied the 3CCF and 4CCF with the geometry and core enumeration shown in Fig. 4.2. The parameters of these fibers are listed in Table 4.1. In case of the 3CCF the distance between all the cores is the same. Thus, all the coupling coefficients will be the same in the scalar and simplified vector cases and will be simply denoted as c. For the 4CCF there are two types of coupling coefficients, since the neighboring cores (cores 1-2, 2-4, 4-3, etc.) have the core pitch d, while the cores placed on the diagonal (cores 1-4, 2-3) have the pitch $\sqrt{2}d$. The coupling coefficients between the neighboring cores are denoted as c_1, while c_2 are the coefficients describing the coupling between the cores on the diagonal. The corresponding coupling matrices for both fibers in case of the scalar and simplified vector models are listed in Tables 4.2, 4.3. As coupling coefficients and birefringence are frequency dependent, there is a natural dependence on frequency for the coupling matrix $\mathbf{M}(\omega)$. Similarly to coupling coefficients it will further be denoted as $\mathbf{M}$ for simplicity. As was mentioned, the supermodes and their propagation constants can be found as the eigenvectors and eigenvalues of the coupling matrix $\mathbf{M}$. The calculation is presented in Section 4.2.3.

Table 4.3: Coupling matrices derived in case of the simplified vector model for the 3CCF and the 4CCF with the geometry shown in Fig. 4.2.

	Coupling matrices
3CCF	$\begin{pmatrix} -\frac{b}{2} & \frac{\sqrt{3}b}{2} & c & 0 & c & 0 \\ \frac{\sqrt{3}b}{2} & \frac{b}{2} & 0 & c & 0 & c \\ c & 0 & -\frac{b}{2} & -\frac{\sqrt{3}b}{2} & c & 0 \\ 0 & c & -\frac{\sqrt{3}b}{2} & \frac{b}{2} & 0 & c \\ c & 0 & c & 0 & b & 0 \\ 0 & c & 0 & c & 0 & -b \end{pmatrix}$
4CCF	$\begin{pmatrix} 0 & b_2 & c_1 & 0 & c_1 & 0 & c_2 & 0 \\ b_2 & 0 & 0 & c_1 & 0 & c_1 & 0 & c_2 \\ c_1 & 0 & 0 & -b_2 & c_2 & 0 & c_1 & 0 \\ 0 & c_1 & -b_2 & 0 & 0 & c_2 & 0 & c_1 \\ c_1 & 0 & c_2 & 0 & 0 & -b_2 & c_1 & 0 \\ 0 & c_1 & 0 & c_2 & -b_2 & 0 & 0 & c_1 \\ c_2 & 0 & c_1 & 0 & c_1 & 0 & 0 & b_2 \\ 0 & c_2 & 0 & c_1 & 0 & c_1 & b_2 & 0 \end{pmatrix}$

The solution to (4.3) can be formally written as

$$\vec{A}(z) = \vec{A}_0 \exp(j\mathbf{M}z) = \vec{A}_0\mathbf{T}, \tag{4.7}$$

where exp denotes the matrix exponential, $\mathbf{T} = \exp(j\mathbf{M}z)$ is the transfer matrix and $\vec{A}_0$ is the input amplitude vector. Eq. (4.7) gives the channel model for the unperturbed fiber and provides the opportunity to simulate the transmission and see effects of the coupling. Algorithm 1 at the end of Section 4.2.2 summarizes all the steps that are necessary for calculation of the transfer matrix $\mathbf{T}$ of an idealized CCF.

4.2.2 Birefringence

The vector model described in [Paper C] and [Paper D] is based on the concept of form birefringence [192]. Note that in these papers we introduced the simplified vector model, where the birefringence in coupling

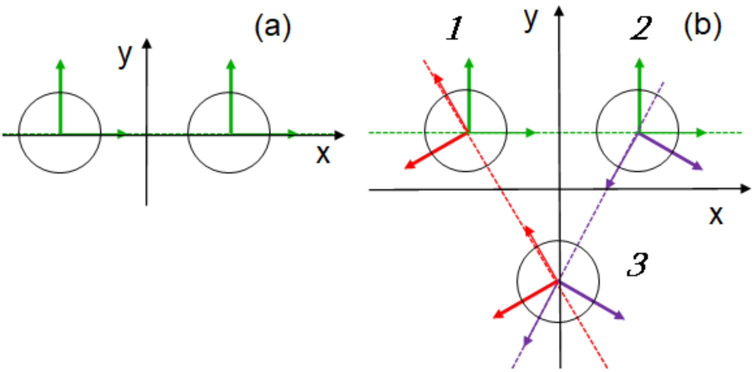

Figure 4.3: Illustration of birefringence axes in (a) a 2CCF and (b) a ring-array structured 3CCF, which manifests a combination of the structure shown in (a) with its two ±120-rotated two coupled-core fiber (2CCF) instances. The numbers $1, 2, 3$ show the enumeration of the cores.

coefficients was neglected for simplicity as it is a very small contribution [192]. In this section, the expanded vector model with consideration of all polarization corrections is shown.

In case when the polarization of the modes is taken into account, the coupling matrix $\mathbf{M}$ should be transformed to a $2D \times 2D$ matrix as shown in Fig. 4.1 (b). It will now contain parameters of the birefringence axes, b_x and b_y and polarization corrections to the coupling coefficients. The coupling coefficients will be now inside of the 2×2 matrices $\mathbf{C}_{pq}$ that characterise the coupling between the cores. Here it is again assumed that the coupling associated with all the cores is identical and orthogonal polarizations between modes do not couple.

The birefringence matrix describing birefringence effects from a neighboring core along the x-axis as in Fig. 4.3 (a)) can be expressed as

$$\mathbf{B} = \begin{pmatrix} b_x & 0 \\ 0 & b_y \end{pmatrix} \tag{4.8}$$

and we assume for symmetry reasons that $b_y = -b_x = b$. The birefringence b is given by [192]

$$b(\omega) = \Delta^2 \beta \cdot \frac{4U^2 W}{V^4} \frac{K_0(W)}{K_1(W)} \times \\ \times \left[\frac{I_1(W)}{K_1(W)} - \frac{I_2(W)}{K_0(W)} \right] K_2(W d_m / r). \tag{4.9}$$

As can be seen, when the cores are placed along one line, they have the same birefringence axes (2CCF case, Fig. 4.3 (a)). However, when there are other cores that are placed in the cladding, one has to project the birefringence from the other cores to the neighboring cores (as shown, for example, in Fig. 4.3 (b)) with the rotation matrix $\mathbf{R}(\phi)$:

$$\mathbf{R}(\phi) = \begin{pmatrix} \cos\phi & \sin\phi \\ -\sin\phi & \cos\phi \end{pmatrix}. \tag{4.10}$$

The rotation is also applied when the coupling coefficient matrices $\mathbf{C}_{pq}$ are built from $\mathbf{C}$, which is given by

$$\mathbf{C} = \begin{pmatrix} c_{pq_x} & 0 \\ 0 & c_{pq_y} \end{pmatrix} \tag{4.11}$$

The coupling coefficient c_{pq_x} can be found with (4.4), while c_{pq_y} is calculated with the polarization correction δc as [192]

$$c_{pq_y} = c_{pq_x} - \delta c, \tag{4.12}$$

where δc is calculated as [192]

$$\delta c = 2\Delta W \frac{K_2(Wd_m/r)}{K_0(Wd_m/r)}(I_1(W)K_0(W) - I_2(W)K_1(W))c_{pq_x}, \tag{4.13}$$

where $\Delta = 1 - n_2/n_1$ is the refractive index difference, $K_2(Wd_m/r)$ is the modified Bessel function of the second kind of order 2 and $I_1(W)$, $I_2(W)$ are the modified Bessel functions of the first kind of orders 1 and 2. Note that in the simplified vector model shown in [Paper C] and [Paper D] $c_{pq_x} = c_{pq_y} = c_{pq}$.

The subsections below will show the formation of birefringence matrices $\mathbf{B}_p$ and coupling coefficient matrices $\mathbf{C}_{pq}$ for the 3CCF and 4CCF shown in Fig. 4.2.

3CCF

In the vector model, the coupling matrix for the 3CCF in Fig. 4.2 can be written in the form

$$\mathbf{M} = \begin{pmatrix} \mathbf{B}_1 & \mathbf{C}_{12} & \mathbf{C}_{13} \\ \mathbf{C}_{21} & \mathbf{B}_2 & \mathbf{C}_{23} \\ \mathbf{C}_{31} & \mathbf{C}_{32} & \mathbf{B}_3 \end{pmatrix}. \tag{4.14}$$

The paragraphs below show the calculation of all the matrix components.

The birefringence for a 3CCF with a ring-array structure can be described using a superposition of birefringences from pairwise linear-array structures as shown in Fig. 4.3. When the third core is placed around two other cores, one has to project the birefringence from the third core to the neighboring cores (as shown in Fig. 4.3 (b)) with the rotation matrix $\mathbf{R}(\phi)$ given by (4.10). The birefringence matrix for each core can then be calculated as the contribution from its two neighbors as

$$\mathbf{B}_1 = \mathbf{B} + \mathbf{R}(-120^\circ) \cdot \mathbf{B} \cdot \mathbf{R}(120^\circ) \tag{4.15}$$

$$\mathbf{B}_2 = \mathbf{B} + \mathbf{R}(120^\circ) \cdot \mathbf{B} \cdot \mathbf{R}(-120^\circ) \tag{4.16}$$

$$\mathbf{B}_3 = \mathbf{R}(-120^\circ) \cdot \mathbf{B} \cdot \mathbf{R}(120^\circ) + \mathbf{R}(120^\circ) \cdot \mathbf{B} \cdot \mathbf{R}(-120^\circ) \tag{4.17}$$

The coupling coefficients matrices are found in the same way, rotating the matrix $\mathbf{C}$ by ±120°:

$$\mathbf{C}_{12} = \mathbf{C}_{21} = \mathbf{C} \tag{4.18}$$

$$\mathbf{C}_{13} = \mathbf{C}_{31} = \mathbf{R}(-120^\circ) \cdot \mathbf{C} \cdot \mathbf{R}(120^\circ) \tag{4.19}$$

$$\mathbf{C}_{23} = \mathbf{C}_{32} = \mathbf{R}(120^\circ) \cdot \mathbf{C} \cdot \mathbf{R}(-120^\circ) \tag{4.20}$$

As was mentioned in Section 4.2.1, the coupling coefficients will be the same in the scalar and simplified vector cases as the distance between the cores is the same. Here, though, we take into account the polarization corrections and denote the coupling coefficients associated with x- and y- polarizations as c_x and c_y respectively. The resulting coupling matrix will take form

$$\mathbf{M} = \begin{pmatrix} \frac{-b}{2} & \frac{\sqrt{3}b}{2} & c_x & 0 & \frac{c_x+3c_y}{4} & \frac{\sqrt{3}(c_y-c_x)}{4} \\ \frac{\sqrt{3}b}{2} & \frac{b}{2} & 0 & c_y & \frac{\sqrt{3}(c_y-c_x)}{4} & \frac{3c_x+c_y}{4} \\ c_x & 0 & \frac{-b}{2} & \frac{-\sqrt{3}b}{2} & \frac{c_x+3c_y}{4} & \frac{\sqrt{3}(c_x-c_y)}{4} \\ 0 & c_y & \frac{-\sqrt{3}b}{2} & \frac{b}{2} & \frac{\sqrt{3}(c_x-c_y)}{4} & \frac{3c_x+c_y}{4} \\ \frac{c_x+3c_y}{4} & \frac{\sqrt{3}(c_y-c_x)}{4} & \frac{c_x+3c_y}{4} & \frac{\sqrt{3}(c_x-c_y)}{4} & b & 0 \\ \frac{\sqrt{3}(c_y-c_x)}{4} & \frac{3c_x+c_y}{4} & \frac{\sqrt{3}(c_x-c_y)}{4} & \frac{3c_x+c_y}{4} & 0 & -b \end{pmatrix} \tag{4.21}$$

In in the simplified vector case, when $c_x = c_y = c$, the coupling matrix will take a simpler form shown in Table 4.3.

4CCF

In the vector model, the coupling matrix for the 4CCF shown in Fig. 4.2 can be written in the form

$$\mathbf{M} = \begin{pmatrix} \mathbf{B}_1 & \mathbf{C}_{12} & \mathbf{C}_{13} & \mathbf{C}_{14} \\ \mathbf{C}_{21} & \mathbf{B}_2 & \mathbf{C}_{23} & \mathbf{C}_{24} \\ \mathbf{C}_{31} & \mathbf{C}_{32} & \mathbf{B}_3 & \mathbf{C}_{34} \\ \mathbf{C}_{41} & \mathbf{C}_{42} & \mathbf{C}_{43} & \mathbf{B}_4 \end{pmatrix}. \tag{4.22}$$

The paragraphs below show the calculation of all the matrix components.

The birefringence for a 4CCF can be described using a superposition of birefringences from pairwise linear-array structures as shown in Fig. 4.4. It should be noted that in this case there will be two types of birefringence matrices, representing the adjacent cores

$$\mathbf{B} = \begin{pmatrix} -b_1 & 0 \\ 0 & b_1 \end{pmatrix} \tag{4.23}$$

and the diagonal cores

$$\mathbf{B}' = \begin{pmatrix} -b_2 & 0 \\ 0 & b_2 \end{pmatrix}. \tag{4.24}$$

The birefringence matrix for each core can then be calculated as the contribution from its three neighbors as

$$\mathbf{B}_1 = \mathbf{B} + \mathbf{R}(-90°) \cdot \mathbf{B} \cdot \mathbf{R}(90°) + \mathbf{R}(45°) \cdot \mathbf{B}' \cdot \mathbf{R}(-45°) \tag{4.25}$$

$$\mathbf{B}_2 = \mathbf{R}(90°) \cdot \mathbf{B} \cdot \mathbf{R}(-90°) + \mathbf{B} + \mathbf{R}(135°) \cdot \mathbf{B}' \cdot \mathbf{R}(-135°) \tag{4.26}$$

$$\mathbf{B}_3 = \mathbf{R}(-90°) \cdot \mathbf{B} \cdot \mathbf{R}(90°) + \mathbf{B} + \mathbf{R}(-45°) \cdot \mathbf{B}' \cdot \mathbf{R}(45°) \tag{4.27}$$

$$\mathbf{B}_4 = \mathbf{R}(90°) \cdot \mathbf{B} \cdot \mathbf{R}(-90°) + \mathbf{B} + \mathbf{R}(225°) \cdot \mathbf{B}' \cdot \mathbf{R}(-225°) \tag{4.28}$$

The contribution from the adjacent cores **B** will cancel out, and the final birefringence matrices become

$$\mathbf{B_1} = \mathbf{B_4} = -\mathbf{B_2} = -\mathbf{B_3} = \begin{pmatrix} 0 & b_2 \\ b_2 & 0 \end{pmatrix}. \tag{4.29}$$

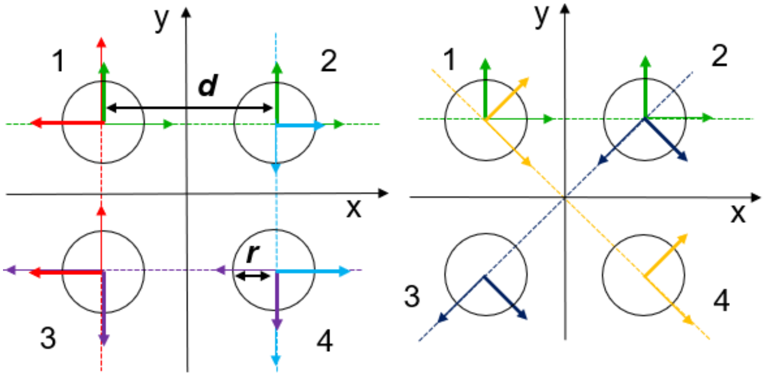

Figure 4.4: Illustration of birefringence axes in a 4CCF, which manifests a combination of the 2CCF structure (green axes) with its $-90°$ (illustration on the left) and $-135°$ (illustration on the right) degree-rotated instances. The numbers $1, 2, 3, 4$ relate to the enumeration of the cores, d is the core pitch between the nearest cores, r is a core radii.

The coupling coefficients matrices will be also of two types, corresponding to the neighboring cores

$$\mathbf{C} = \begin{pmatrix} c_{1_x} & 0 \\ 0 & c_{1_y} \end{pmatrix} \tag{4.30}$$

and the diagonal cores

$$\mathbf{C}' = \begin{pmatrix} c_{2_x} & 0 \\ 0 & c_{2_y} \end{pmatrix}. \tag{4.31}$$

The coupling coefficients matrices are found in the same way, rotating the matrices $\mathbf{C}$ and $\mathbf{C}'$ by $\pm 90°$ and $\pm 135°$:

$$\mathbf{C}_{12} = \mathbf{C}_{21} = \mathbf{C} \tag{4.32}$$

$$\mathbf{C}_{13} = \mathbf{C}_{31} = \mathbf{R}(-90°) \cdot \mathbf{C} \cdot \mathbf{R}(90°) \tag{4.33}$$

$$\mathbf{C}_{14} = \mathbf{C}_{41} = \mathbf{R}(45°) \cdot \mathbf{C}' \cdot \mathbf{R}(-45°) \tag{4.34}$$

$$\mathbf{C}_{23} = \mathbf{C}_{32} = \mathbf{R}(135°) \cdot \mathbf{C}' \cdot \mathbf{R}(-135°) \tag{4.35}$$

$$\mathbf{C}_{24} = \mathbf{C}_{42} = \mathbf{R}(90^\circ) \cdot \mathbf{C} \cdot \mathbf{R}(-90^\circ) \tag{4.36}$$

$$\mathbf{C}_{34} = \mathbf{C}_{43} = \mathbf{R}(-90^\circ) \cdot \mathbf{C} \cdot \mathbf{R}(90^\circ) \tag{4.37}$$

The resulting coupling matrix will then take form

$$\mathbf{M} = \begin{pmatrix} 0 & b_2 & c_{1_x} & 0 & c_{1_y} & 0 & \frac{c_{2_x}+c_{2_y}}{2} & \frac{c_{2_y}-c_{2_x}}{2} \\ b_2 & 0 & 0 & c_{1_y} & 0 & c_{1_x} & \frac{c_{2_y}-c_{2_x}}{2} & \frac{c_{2_x}+c_{2_y}}{2} \\ c_{1_x} & 0 & 0 & -b_2 & \frac{c_{2_x}+c_{2_y}}{2} & \frac{c_{2_x}-c_{2_y}}{2} & c_{1_y} & 0 \\ 0 & c_{1_y} & -b_2 & 0 & \frac{c_{2_x}-c_{2_y}}{2} & \frac{c_{2_x}+c_{2_y}}{2} & 0 & c_{1_x} \\ c_{1_y} & 0 & \frac{c_{2_x}+c_{2_y}}{2} & \frac{c_{2_x}-c_{2_y}}{2} & 0 & -b_2 & c_{1_y} & 0 \\ 0 & c_{1_x} & \frac{c_{2_x}-c_{2_y}}{2} & \frac{c_{2_x}+c_{2_y}}{2} & -b_2 & 0 & 0 & c_{1_x} \\ \frac{c_{2_x}+c_{2_y}}{2} & \frac{c_{2_y}-c_{2_x}}{2} & c_{1_y} & 0 & c_{1_y} & 0 & 0 & b_2 \\ \frac{c_{2_y}-c_{2_x}}{2} & \frac{c_{2_x}+c_{2_y}}{2} & 0 & c_{1_x} & 0 & c_{1_x} & b_2 & 0 \end{pmatrix} \tag{4.38}$$

In in the simplified vector case, when $c_{1_x} = c_{1_y} = c_1$ and $c_{2_x} = c_{2_y} = c_2$, the coupling matrix will take a simpler form shown in Table 4.3.

Algorithm 1 Calculation of transfer matrix $\mathbf{T}$ of an unperturbed CCF

```
Input: $r$, $d$, $n_1$, $n_2$ and frequency/wavelength
1: Calculate V-parameter with (4.5)
2. Calculate U and W with (4.6)
3: Calculate $c_{pq}$ ($^*c_{pq_x}$) using (4.4)
4: *Calculate $c_{pq_y}$ using (4.12) and (4.13)
5: *Calculate $\mathbf{C}_{pq}$
6: *Calculate $b$ using (4.9)
7: *Calculate $\mathbf{B}_p$
8: Form $\mathbf{M}$ as in Fig. 4.1
9: Calculate $\mathbf{T} = \exp(j\mathbf{M}z)$
10: Repeat for other frequencies/wavelengths if necessary
Output: $\mathbf{T}$
*the steps necessary for the vector model
```

4.2.3 Supermodes, their propagation constants and group delays

The supermodes $\vec{s}_k$ and their propagation constants β_{s_k} can be found by solving the eigenvalue problem for the coupling matrix $\mathbf{M}$. Algorithms

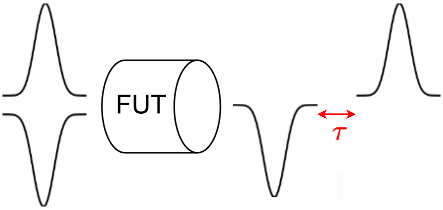

Figure 4.5: Explanation of the group delays τ_k of the supermodes in case when two supermodes propagate through a fiber under test (FUT).

for eigendecomposition include the power algorithm and the QR algorithm [193]. The results in this thesis were obtained in analytical form using Wolfram Mathematica and Python with *simpy* and *linalg* modules, where the eigenvectors and eigenvalues were found numerically as well.

Another important characteristic of the supermodes of CCFs are their GDs. The GDs can be understood as the time delay between the supermodes at the output of the fiber (Fig. 4.5) and they are related to the GDS, which is necessary to know when calculating the number of taps for a MIMO equalizer. The GDs per fiber length can be calculated as the first derivative of $\beta_{s_k}(\omega)$ with respect to ω

$$\tau_k = \frac{d\beta_{s_k}(\omega)}{d\omega}, \tag{4.39}$$

which will give the GDs for a full fiber if multiplied by the fiber length. It also can be found as the eigenvalues of the delay operator [70]:

$$\mathbf{D} = -j\mathbf{T}^{\dagger}\frac{d\mathbf{T}}{d\omega}. \tag{4.40}$$

The calculation below shows the supermodes, their propagation constants and GDs for both 3CCF and 4CCF for the simplified and expanded vector models. Analytical calculation can be found in the first 4 files in Ref. [194] and all the generated figures with numerical results are accessible in the last file with a Jupiter notebook in the same reference.

3CCF

Propagation constants of the supermodes are found as the eigenvalues of the coupling matrix 4.21:

$$\beta_{s_1} = -b + \frac{c_x - 3c_y}{2} \tag{4.41}$$

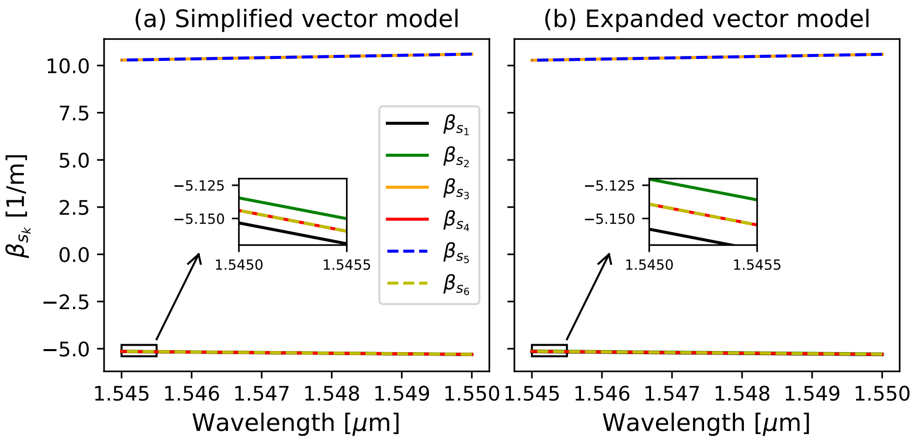

Figure 4.6: Propagation constants β_{s_k} of the supermodes of the 3CCF in case of the simplified and expanded vector models.

$$\beta_{s_2} = b + \frac{c_y - 3c_x}{2} \tag{4.42}$$

$$\beta_{s_{3,4}} = \beta_{s_{5,6}} = \frac{c_x + c_y \pm \psi}{4}, \tag{4.43}$$

where $\psi = \sqrt{16b^2 + 13c_x^2 + 10c_xc_y + 13c_y^2 + 16b(c_y - c_x)}$. As can be seen, when $c_x = c_y = c$, the equations above correspond to the simpler case presented in [Paper C], where the propagation constants were found to be

$$\beta_{s_{1,2}} = -(c \pm b) \tag{4.44}$$

and

$$\beta_{s_{3,4}} = \beta_{s_{5,6}} = \frac{c \pm \sqrt{4b^2 + 9c^2}}{2}. \tag{4.45}$$

Fig. 4.6 demonstrates the calculated propagation constants b_{s_k} of the 3CCF in case of the simplified and expanded vector models. As can be seen, the difference between the two cases is not significant: both results demonstrate two groups of b_{s_k} and accounting for the polarization effects in coupling coefficients (Fig. 4.6 (b)) results in slightly larger splitting of the eigenvalues inside the second group.

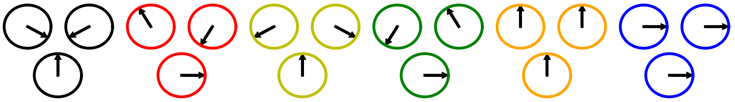

Figure 4.7: Supermodes of the 3CCF in case of the simplified vector model. Colors mark corresponding eigenvalues β_{s_k} shown in Fig. 4.6.

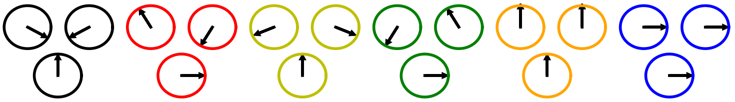

Figure 4.8: Supermodes of the 3CCF in case of the expanded vector model. Colors mark corresponding eigenvalues β_{s_k} shown in Fig. 4.6.

Supermodes are calculated as the eigenvectors of the coupling matrix (4.21):

$$\vec{s}_{1,2} = \left\{ \frac{\sqrt{3}}{2}, -\frac{1}{2}, -\frac{\sqrt{3}}{2}, -\frac{1}{2}, 0, 1 \right\}, \left\{ -\frac{1}{2}, -\frac{\sqrt{3}}{2}, -\frac{1}{2}, \frac{\sqrt{3}}{2}, 1, 0 \right\}, \tag{4.46}$$

$$\begin{aligned}\vec{s}_{3,4} = \Bigg\{ & \frac{4b - 5c_x - c_y \mp \psi}{4\sqrt{3}(c_x + c_y)}, \frac{4b - c_x + 3c_y \mp \psi}{4(c_x + c_y)}, \\ & \qquad \frac{-4b + 5c_x + c_y \pm \psi}{4\sqrt{3}(c_x + c_y)}, \frac{4b - c_x + 3c_y \mp \psi)}{4(c_x + c_y)}, 0, 1 \Bigg\},\end{aligned} \tag{4.47}$$

$$\begin{aligned}\vec{s}_{5,6} = \Bigg\{ & \frac{-4b + 3c_x - c_y \mp \psi}{4(c_x + c_y)}, \frac{4b + c_x + 5c_y \pm \psi}{4\sqrt{3}(c_x + c_y)}, \\ & \qquad \frac{-4b + 3c_x - c_y \mp \psi}{4(c_x + c_y)}, \frac{-4b - c_x - 5c_y \mp \psi)}{4\sqrt{3}(c_x + c_y)}, 1, 0 \Bigg\}.\end{aligned} \tag{4.48}$$

and shown in Fig. 4.8, where arrows denote the direction of electrical field. Every supermode is represented by 6 coordinates, where every pair corresponds to each fiber core. This means that the first 2 components of every supermode are the coordinates of the arrow end in the first core, the third and fourth components are the coordinates of the arrow end in

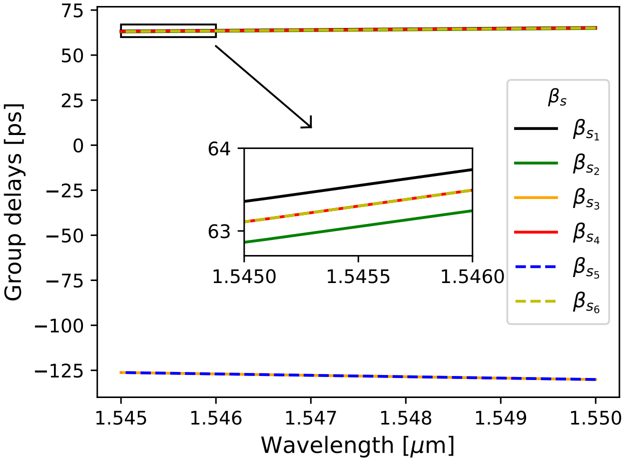

Figure 4.9: Calculated GDs of the supermodes in the unperturbed 3CCF.

the second core and the fifth and sixth components are the coordinates of the arrow end in the third core. The center of each core has coordinates (0;0). The supermodes are plot for $c_x = 5.159$ 1/m, $c_y = 5.149$ 1/m and $b = 0.0094$ 1/m, which are calculated at $\lambda = 1545.49$ nm with (4.4), (4.12) and (4.9) respectively.

It can be seen that by setting $c_x = c_y = c$, the results will correspond to the supermodes obtained in the simplified vector model in [Paper C]:

$$\vec{s}_{1,2} = \left\{ \frac{\sqrt{3}}{2}, -\frac{1}{2}, -\frac{\sqrt{3}}{2}, -\frac{1}{2}, 0, 1 \right\}, \left\{ -\frac{1}{2}, -\frac{\sqrt{3}}{2}, -\frac{1}{2}, \frac{\sqrt{3}}{2}, 1, 0 \right\}, \tag{4.49}$$

$$\vec{s}_{3,4} = \left\{ \frac{2b - 3c \mp \sqrt{4b^2 + 9c^2}}{4\sqrt{3}c}, \frac{2b + c \mp \sqrt{4b^2 + 9c^2}}{4c}, \right. \\ \left. \frac{-2b + 3c \pm \sqrt{4b^2 + 9c^2}}{4\sqrt{3}c}, \frac{2b + c \mp \sqrt{4b^2 + 9c^2})}{4c}, 0, 1 \right\}, \tag{4.50}$$

$$\vec{s}_{5,6} = \left\{ \frac{-2b + c \mp \sqrt{4b^2 + 9c^2}}{4c}, \frac{2b + 3c \pm \sqrt{4b^2 + 9c^2}}{4\sqrt{3}c}, \right. \\ \left. \frac{-2b + c \mp \sqrt{4b^2 + 9c^2}}{4c}, \frac{-2b - 3c \mp \sqrt{4b^2 + 9c^2})}{4\sqrt{3}c}, 1, 0 \right\}. \tag{4.51}$$

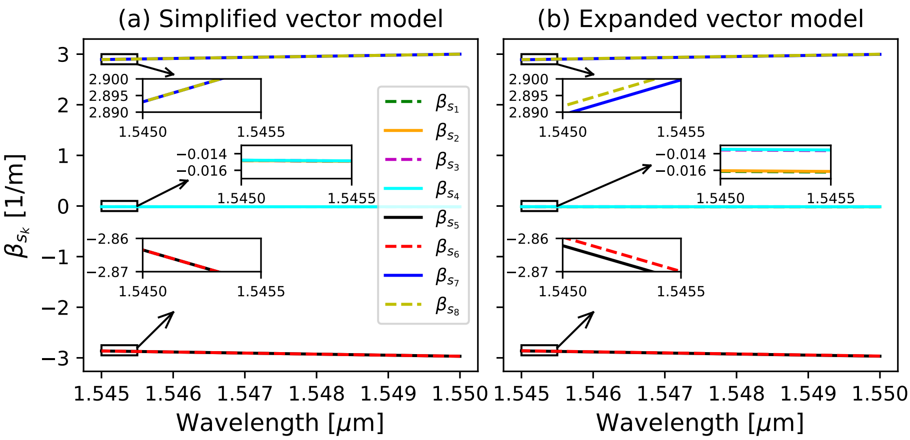

Figure 4.10: Propagation constants β_{s_k} of the supermodes of the 4CCF-2 for the simplified and expanded vector models.

These supermodes are shown in Fig. 4.7. It can be seen that they are identical to ones in Fig. 4.8, demonstrating that the polarization corrections to the coupling coefficients are indeed small contributions and do not impact the eigenvectors shape.

The GDs of the 3CCF are found by differentiating propagation constants (4.41)-(4.43) with respect to frequencies, as in (4.39), and multiplying the result by the fiber length, L=1.6 km. The calculated GDs are shown in Fig. 4.9. As propagation constants of the supermodes β_{s_k} do not exhibit significant differences between the simplified and expanded models, only the expanded vector model is illustrated for simplicity. It can be seen that the GDs form two groups. The GDs of two degenerate supermodes that have the highest propagation constants are grouped at the bottom of the graph, in contrast to the other four GDs showed in the inset. The GDs do not change over the given interval. In [Paper C] we calculated the GDs of the 3CCF in a larger wavelength interval, where a slight linear variation in GDs was present.

4CCF

In case of the 4CCF, the coupling matrix in the expanded vector model will have an even more complicated form than for the 3CCF, since there are two types of coupling coefficients, which in case of x- and y-polarizations will split in four types (4.38). This makes the analytical solution of the eigenvalue problem complicated and bulky. This section,

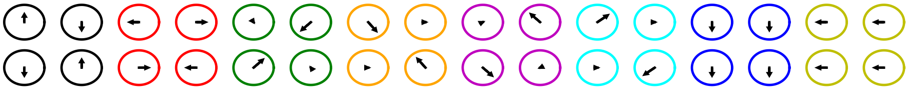

Figure 4.11: Supermodes of the 4CCF-2 in case of the simplified vector model. Colors mark corresponding eigenvalues β_{s_k} shown in Fig. 4.10.

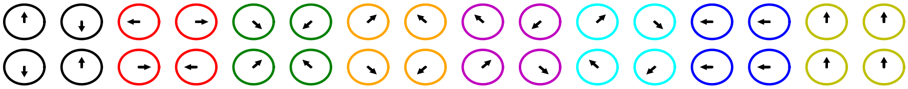

Figure 4.12: Supermodes of the 4CCF-2 calculated numerically in case of the expanded vector model. Colors mark corresponding eigenvalues β_{s_k} shown in Fig. 4.10.

thus, shows the analytical calculation results for the supermodes in the simplified vector model and numerical calculation of the supermodes in the expanded vector model. The comprehensive analytical calculation for the both simplified and expanded vector models can be found in Ref. [194].

Propagation constants of the 4CCF in the simplified vector case can be found as eigenvalues of the coupling matrix shown in Table 4.3:

$$\beta_{s_{1,3}} = \beta_{s_{2,4}} = \mp b_2 - c_2, \tag{4.52}$$

$$\beta_{s_{5,7}} = \beta_{s_{6,8}} = c_2 \mp \sqrt{b_2^2 + 4c_1^2} \tag{4.53}$$

and are shown in Fig. 4.10 for 4CCF-2, which also demonstrates numerically calculated eigenvalues in case of the expanded vector model. As can be seen, both results demonstrate three groups of b_{s_k} and accounting for the polarization effects in coupling coefficients (Fig. 4.10 (b)) results in splitting of the eigenvalues inside every group.

The supermodes are the eigenvectors of the coupling matrix given in Table 4.3 and calculated to be

$$\vec{s}_{1,2} = \left\{0, 0, -1, -1, 1, 1, 0, 0\right\}, \left\{1, -1, 0, 0, 0, 0, -1, 1\right\}, \tag{4.54}$$

$$\vec{s}_{3,4} = \left\{0, 0, -1, 1, 1, -1, 0, 0\right\}, \left\{1, 1, 0, 0, 0, 0, -1, -1\right\}, \tag{4.55}$$

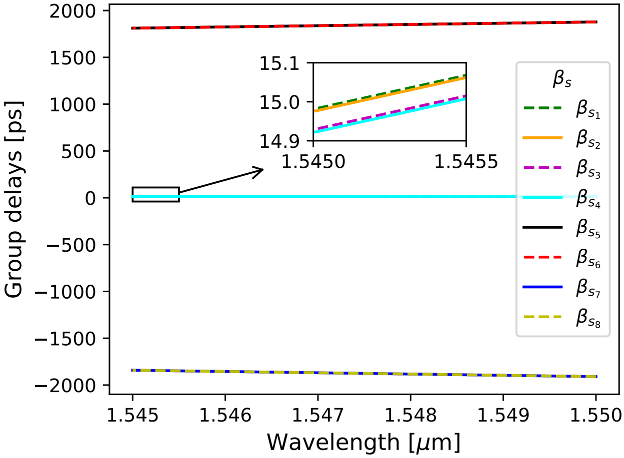

Figure 4.13: Calculated GDs of the supermodes in the unperturbed 4CCF-2 in case of the simplified vector model.

$$\vec{s}_{5,7} = \left\{0, \pm 1, \mp\frac{b_2}{2c_1}, \frac{-\sqrt{b_2^2+4c_1^2}}{2c_1}, \mp\frac{b_2}{2c_1}, \frac{-\sqrt{b_2^2+4c_1^2)}}{2c_1}, 0, \pm 1\right\}, \tag{4.56}$$

$$\vec{s}_{6,8} = \left\{-1, 0, \frac{\pm\sqrt{b_2^2+4c_1^2}}{2c_1}, \frac{b_2}{2c_1}, \frac{\pm\sqrt{b_2^2+4c_1^2)}}{2c_1}, \frac{b_2}{2c_1}, -1, 0\right\} \tag{4.57}$$

and shown in Fig. 4.11 for 4CCF-2. The supermodes are plot for $c_1 = 1.492$ 1/m, and $b_2 = 2.67 \cdot 10^{-5}$ 1/m, which are calculated at $\lambda = 1550$ nm with (4.4), and (4.9) respectively. Fig. 4.12 shows numerically calculated supermodes of 4CCF-2 in case of the expanded vector model. It is notable that the first two supermodes look the same, while the last two have 90° rotated fields. The other four supermodes exhibit non zero fields in the diagonal cores, in contrast to the simplified vector model case.

The GDs are found by differentiating the propagation constants (4.52)-(4.53) with respect to frequencies, as in (4.39), and multiplying the result by the fiber length, $L = 69.2$ km. The calculated GDs of the 4CCF-2 are shown in Fig. 4.13. Note that there is an error in color marking in Fig. 2 in [Paper D], where the GDs of the 4CCF-1 were calculated. The colors for the first and third GDs groups should be reversed.

The Algorithm 2 below summarizes all the discussed steps for calculations of the supermodes and their propagation constants.

```
**Algorithm 2** Calculation of supermodes $\vec{s}_k$ and their propagation constants $\beta_{s_k}$
Input: $r$, $d$, $n_1$, $n_2$ and frequency/wavelength
1: Follow steps 1-8 of Algorithm 1 to form $\mathbf{M}$
2: Find the eigenvalues $\beta_{s_k}$ of $\mathbf{M}$
3: Find the eigenvectors $\vec{s}_k$ of $\mathbf{M}$
4: Repeat for other frequencies/wavelengths if necessary
Output: $\vec{s}_k$ and $\beta_{s_k}$
```

4.3 Random coupling models

The core separation and ellipticity in a realistic CCF will vary by small amounts over the length of the fiber due to manufacturing imperfections, causing small variations in the core coupling and birefringence parameters, which results in a randomized core coupling and phase delay between the modes of the coupled cores. An accurate model for CCFs has to include this random mode coupling. It is, thus, unrealistic to assume that the transfer matrix $\mathbf{T} = \exp(j\mathbf{M}z)$ is constant over the full fiber length L, as was done in the deterministic model in Section 4.2. However, this matrix can be considered constant over a short length of the fiber, which is called the coupling length. This length is different for different CCFs and can be calculated from measured GDS or impulse response of the fiber. The model can then be performed by building the fiber of length L from constant coupling parts, where every piece is also subjected to random perturbations. This approximation implies that the fiber under study can be concatenated by N constant coupling parts, in between of which effects of random mode coupling are taken into account as shown in Fig. 4.14. The following sections present a theoretical description of realistic models for such a fiber with random coupling along its length. The models are proposed for the static and dynamic cases. The former include only frequency-dependent effects originated from coupling and the latter takes into account time-varying effects. The equations that will be described in this section hold both in the scalar and vector models. In case of the vector model it is necessary to substitute D with $2D$ in (4.59), (4.60), (4.65), (4.66), (4.70), (4.72)-(4.74).

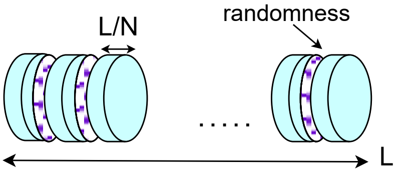

Figure 4.14: Illustration of the general idea of random coupling model.

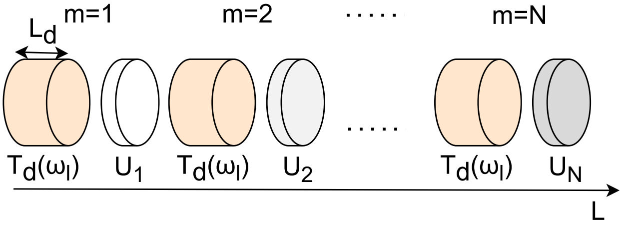

Figure 4.15: Illustration of the static random coupling model schematics.

4.3.1 Static random coupling model

Random propagation in a CCF that supports D modes ($2D$ modes in polarization-multiplexed case) can be modeled by using the aforementioned concatenation rule that originates from PMD calculus [195]. The method is illustrated in Fig. 4.14 and 4.15. A piece of length L_d of an ideal CCF is represented by the delay matrix $\mathbf{T_d}$:

$$\mathbf{T_d}(\omega_l) = \exp\left(j\mathbf{M}(\omega_l)L_d\right), \tag{4.58}$$

which is similar to the transfer function for ideal fiber of length L_d from (4.7) and defined for a set of $l = 0...s-1$ frequencies.

The length of one concatenation, L_d, is always constant, but it is possible to investigate the effect of changing its length. This is studied in [Paper C], where we analysed a 1.6 km 3CCF by changing the number of concatenations N, which, in turn corresponded to different L_d. It is important to note though, that the model of a real fiber has to be built on (4.58) with its real correlation length, which corresponds to the length of one concatenation piece, L_d. This, in turn, will correspond to a specific number of concatenations $N = L/L_d$. Thus, to model a real fiber, one has to calculate an appropriate N knowing the correlation length of the fiber. For this, the GDS of the investigated fiber has to be measured. GDS can also be estimated from the expression for GDS defined in

[Paper C]:

$$\langle GDS^2 \rangle = \frac{N}{D} \sum_{k=1}^{D} \tau_k^2, \tag{4.59}$$

where τ_k are the eigenvalues of the delay operator that can be calculated using the deterministic model presented in the previous section with (4.39). Thus, in order to define a reasonable number of concatenations N, one can relate the total measured GDS for the fiber $\langle GDS^2 \rangle$ and its ideal GDS per piece:

$$N = \langle GDS^2 \rangle D / \sum_{k=1}^{D} \tau_k^2. \tag{4.60}$$

Random perturbations in CCFs can be considered and modeled in various ways [106]. As mentioned above, the randomness in real CCFs is likely a variation in core size and separations along the fiber due to manufacturing imperfections. This can be modeled by introducing a random unitary matrix $\mathbf{U}$. For symmetry reasons we argue that $\mathbf{U}$ should have the Haar distribution [196], and can be realized using QR-factorization [197]. The matrices $\mathbf{U}$ are calculated for every concatenation and placed between the sections described by $\mathbf{T_d}(\omega_l)$ as indicated in Fig. 4.15.

The total transfer matrix can be then found as

$$\mathbf{T_{tot}}(\omega_l) = \prod_{m=0}^{N-1} \mathbf{T_d}(\omega_l) \cdot \mathbf{U}_{N-m} \quad \forall\, l = 0...s-1. \tag{4.61}$$

The Algorithm 3 summarizes the steps discussed above for the transfer matrix calculation. Examples of the model application can be found in Section 4.3.4.

4.3.2 Time drift model

The aim of introducing a time-dependent part in the model is to take time drift effects in CCFs into account. The origin of the time drift can be temperature fluctuations along the fibers, mechanical movements, or other time-varying effects.

In the previous section, for the static random coupling model, it was assumed that the perturbations are modeled by a random unitary matrix

```
Algorithm 3 Calculation of transfer matrix $\mathbf{T_{tot}}(\omega_l)$
Input: $r$, $d$, $n_1$, $n_2$, $n$ and set of frequencies/wavelengths
1: Follow steps 1-8 of Algorithm 1 to form $\mathbf{M}(\omega_l)$
2: Choose/calculate $N$ with (4.60)
3: Calculate $\mathbf{T_d}(\omega_l)$ with (4.58)
4: Generate $\mathbf{U}_m$, $\forall\ m = 1...N$ using algorithm [197]
5: Calculate $\mathbf{T_{tot}}(\omega_l)$ using (4.61)
Output: $\mathbf{T_{tot}}(\omega_l)$, $l = 0...s-1$
```

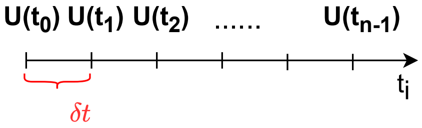

Figure 4.16: Illustration of the time drift model: matrices at different time instances $i = 0...n-1$ separated by δt.

$\mathbf{U}_m$ which was constant for a chosen concatenation m. Assume now that $\mathbf{U}$ is a $D \times D$ ($2D \times 2D$) unitary transfer matrix and changes with time as

$$\mathbf{U}(t_i) = \exp(j\mathbf{H}_{i-1}\gamma)\mathbf{U}(t_{i-1}) = \mathbf{\Delta U} \cdot \mathbf{U}(t_{i-1}), \tag{4.62}$$

where $\mathbf{H}_i$ is a $D \times D$ ($2D \times 2D$) Hermitian matrix, $\gamma = \sqrt{\delta t/T_D}$ is a numerical parameter describing the scaling factor of the standard deviation of $\mathbf{H}_i$ and controlling how correlated $\mathbf{U}(t_{i-1})$ and $\mathbf{U}(t_i)$ are. The decorrelation time T_D is unique for each fiber installation and should be measured, δt is a short time period.

The idea of the model is illustrated in Fig. 4.16, showing a time scale divided by n discrete time points separated by δt. Each time instance corresponds to a matrix $\mathbf{U}(t_i)$, $i = 0....n-1$, which has a recursive structure, as can be seen from (4.62).

The steps for calculation of the time drift matrices $\mathbf{U}(t_i)$ are summarized in Algorithm 4. First, we choose an arbitrary, small number γ and the number of time points n. Next, we generate a random unitary matrix $\mathbf{U}(t_0)$ corresponding to an initial state in the same manner as in [197]. After that, we generate a $D \times D$ ($2D \times 2D$) matrix $\mathbf{R}$, which has complex normally distributed elements r_{sp} with $\mathcal{N}(0,1)$. Using this result, the matrix $\mathbf{H}$ is then calculated and plugged in to the matrix exponential to form $\mathbf{\Delta U}$, which represents how the initial matrix changes

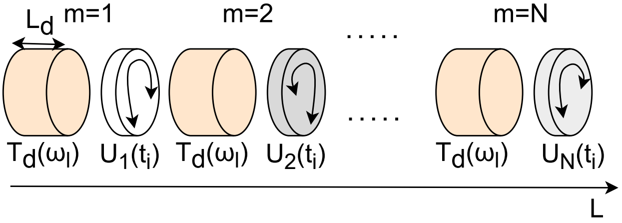

Figure 4.17: Illustration of the dynamic random coupling model schematics.

over the interval δt. In the last step, the time drift matrix is calculated using the initial state matrix and matrix $\mathbf{\Delta U}$.

Algorithm 4 Generation of time drift matrices $\mathbf{U}(t_i)$

```
**Input**: $\gamma$, $n$
1: Generate $\mathbf{U}(t_0)$ using algorithm in [197]
2: Generate $\mathbf{R}_i = \{r_{sp} \in \mathbb{C}^{D \times D}, r_{sp} \sim \mathcal{N}(0,1)\}$
3: Calculate $\mathbf{H}_i = \frac{\mathbf{R}_i + \mathbf{R}^\dagger{}_i}{2}$
4: Calculate $\mathbf{\Delta U} = \exp(j\mathbf{H}_i\gamma)$
5: Calculate $\mathbf{U}(t_{i+1}) = \mathbf{\Delta U} \cdot \mathbf{U}(t_i)$
6: Repeat the steps 2-6 $\forall\ i = 1...n-1$.
**Output**: $\mathbf{U}(t_i)$, $i = 0...n-1$
```

4.3.3 Dynamic random coupling model

The aim of the dynamic model is to incorporate the time drift model into the static random coupling model described in Section 4.3.1. Instead of using one randomly generated unitary matrix $\mathbf{U}_m$ for each fiber piece, we define a set of matrices $\mathbf{U}_m(t)$, which are generated according to Algoritm 4 at every concatenation m (Fig. 4.17). The total transfer function can be then calculated as

$$\mathbf{T_{tot}}(\omega_l, t_i) = \prod_{m=0}^{N-1} \mathbf{T_d}_{N-m}(\omega_l) \cdot \mathbf{U}_{N-m}(t_i). \tag{4.63}$$

The resulting $\mathbf{T_{tot}}$ will represent a transfer matrix at every frequency l and time instance i, which is illustrated in Fig. 4.18. It is important to note that this model assumes the time drift is much slower than any group delay. The Algorithm 5 summarizes the steps for the transfer

Algorithm 5 Calculation of transfer matrix $\mathbf{T_{tot}}(\omega_l, t_i)$

```
Input: $r$, $d$, $n_1$, $n_2$, $l$, $n$ and set of frequencies/wavelengths
1: Follow steps 1-3 of Algorithm 3 to form $\mathbf{T_d}(\omega_l)$
2: Generate a set of matrices $\mathbf{U}_m(t_i)$ $\forall\ m = 1...N$ using Algorithm 4
3: Calculate $\mathbf{T_{tot}}(\omega_l, t_i)$ using (4.63)
Output: $\mathbf{T_{tot}}(\omega_l, t_i)$, $i = 0...n-1, l = 0...s-1$
```

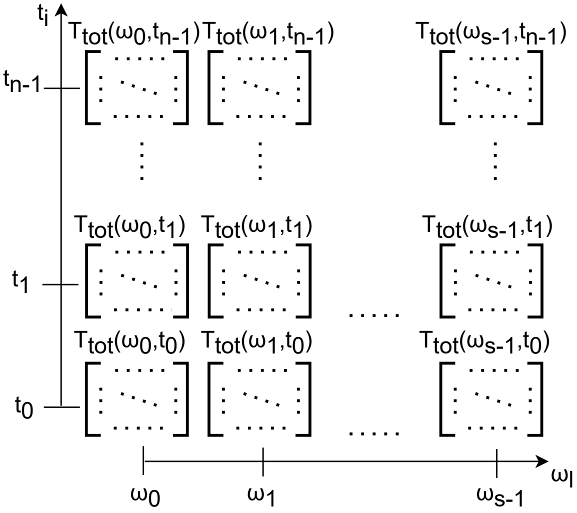

Figure 4.18: Representation of the dynamic model output: $n \times s \times D \times D$ array of the transfer matrix $\mathbf{T_{tot}}$.

matrix $\mathbf{T_{tot}}(\omega_l, t_i)$ calculation. Examples of the model application can be found in Section 4.3.4.

4.3.4 Application of the random coupling models for the analysis of CCFs

There are numerous effects and properties of the CCFs that can be studied with the presented models. The subsections below demonstrate an overview of the investigated characteristics in the 3CCF with the geometrical parameters listed in Table 4.1. All the results are obtained with the expanded vector model. The simulation parameters for all calculations are listed in Table 4.4, unless specified otherwise. Note that the number of concatenations $N = 22$ indicated in Table 4.4 is calculated to model a real 3CCF characterised in [Paper A]. As the ideal GDS is known from

Table 4.4: Simulation parameters of the 3CCF used in Section 4.3.4.

Simulation parameters	Values
Wavelength range λ [μm]	1.545-1.550
Number of concatenations N	22
Number of frequency points s	500
Number of time points n	500
Time drift parameter γ	0.001

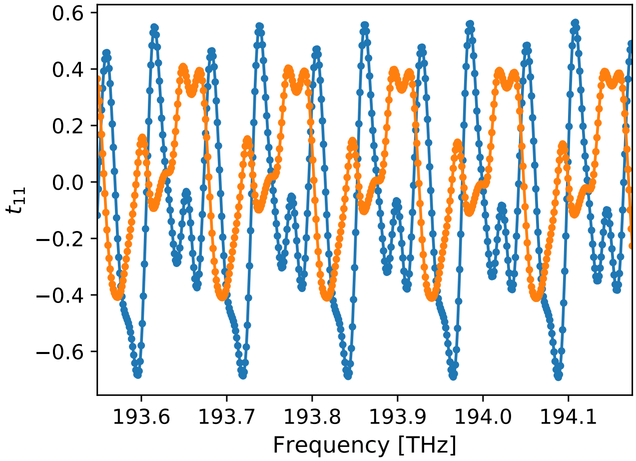

Figure 4.19: Real (blue) and imaginary (orange) parts of the element t_{11} of a transfer matrix $\mathbf{T_{tot}}(\omega_l)$.

the calculation in Section 4.2.3 and experimental GDS was estimated to be 14.6 $ps/\sqrt{km}$ in [Paper A], N and L_d can be easily calculated with (4.60).

Transfer function

The transfer matrix of a CCF can be calculated according to Algorithm 3 when there is no time dependence and with Algorithm 5 for the dynamic model. The transfer function is the basis for calculating other characteristics, as it contains all the information about fiber under study. The investigation of the transfer matrix elements can also give insights about the propagation inside the fiber, for example, the rate of frequency/time variations, periodicity, etc.

As an example, Fig. 4.19 demonstrates real and imaginary parts of

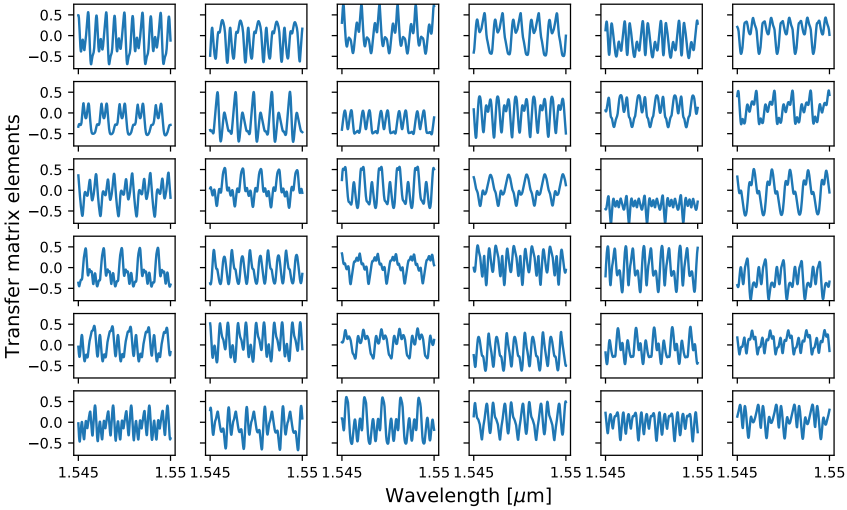

Figure 4.20: A 6×6 transfer matrix $\mathbf{T_{tot}}(\omega_l)$ of the 3CCF. Only real part is shown for clarity.

the first element t_{11} of the transfer matrix of the 3CCF calculated with (4.61). The fact that all N concatenations have the same length causes the curve to be (artificially) periodic in frequency. The period in this case is related to the inverse GDS of each element. The full transfer matrix of the 3CCF is shown in Fig. 4.20. It can be seen that all its elements exhibit periodic behavior, similarly to t_{11} shown in Fig. 4.19. This result can be also compared with the experimental magnitude of the 3CCF's transfer function shown in Fig. 3.8. As can be observed, the experimental data manifests similar behavior. In [Paper C] we investigated how the behavior of t_{11} will change with different N for the same fiber length and the reader is referred to this paper for more details on this case.

Group delays

The GDs in a fiber with random coupling can be found by calculating the eigenvalues of the delay operator $\mathbf{D}$ similar to (4.40):

$$\mathbf{D} = -j\mathbf{T}^{\dagger}_{\mathbf{tot}}\frac{d\mathbf{T_{tot}}}{d\omega}. \tag{4.64}$$

The GDs for one realization of the transfer matrix are illustrated by red lines in Fig. 4.21. It can be seen that they show periodic behavior and do not cross. As was discussed in [94], the delay operator $\mathbf{D}$ can be

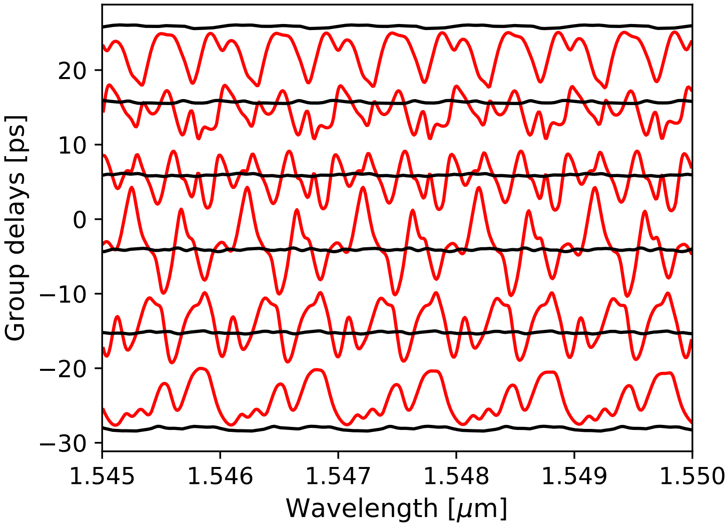

Figure 4.21: The GDs of the 3CCF calculated for 1 transfer matrix realization (red curves) and averaged over 500 realizations (black curves).

modeled as a random Gaussian matrix, and since the probability for such a matrix to have two identical eigenvalues is negligibly small, the GDs do not coincide. In [Paper C] we investigated the GDs of the 3CCF in case of 1 transfer matrix realization for various number of concatenations N. It was shown that when $N = 1$ and $N = 2$ the GDs remain constant over the frequency range, while showing periodic random behavior at large N. In [Paper D] we studied the GDs of the 4CCF-1, where we kept the length of one concatenation L_d constant, while changing N and observed the same type of behavior for the GDs. In [Paper F] we studied GDs of the 4CCF-2 and showed that the behavior agrees well with what has been reported in experiment [198] for a 4CCF with the same parameters.

The black lines in Fig. 4.21 show the GDs calculated as average over 500 realizations of the transfer matrix. Notably, their values are constant over the wavelength span, similarly to the GDs in the unperturbed case shown in Fig. 4.9. As was shown in [Paper C], taking into account the birefringence effects does not change the GDs in an unperturbed 3CCF significantly, since in CCFs the magnitude of birefringence is much smaller than the coupling, $b << c_{pq}$. However, in the 3CCF subject to random perturbations, the GDs become more polarization dependent and change much more significantly. Moreover, when we increased N, they became distinct in contrast to the ideal case, when they formed 2

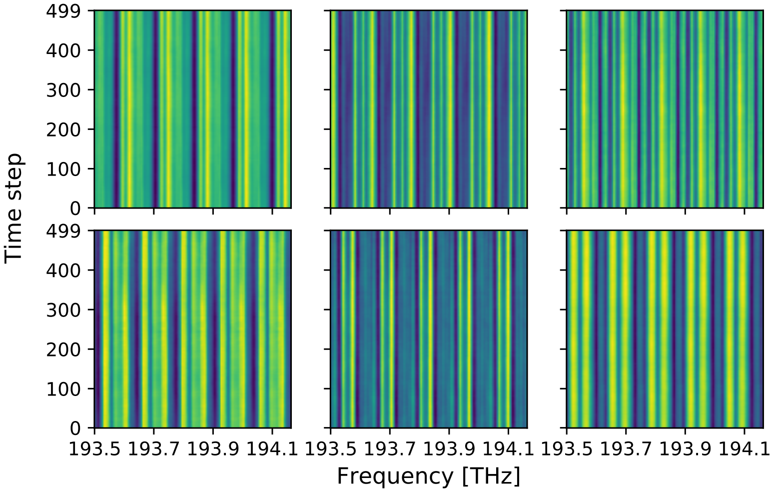

Figure 4.22: Frequency and time evolution of all six GDs of the 3CCF calculated for 1 transfer matrix realization at $\gamma = 0.001$. Color scale from blue to yellow indicate minimum to maximum values respectively for every GD.

groups.

Fig. 4.22 shows dynamic behavior of the 3CCF's GDs. The time dependence of the GDs manifests a random, but periodic behavior, similarly to frequency dependence. However, how fast the GDs will change with time is defined by the γ parameter. Evidently, the smaller the γ parameter, the less drastic changes in time the GDs will experience. Dynamic behavior of the GDs was also studied in [Paper F] for the 4CCF-2.

Group delay spread

As was discussed in the previous chapters, GDS quantifies the modal dispersion and defines the required number of filter taps in a MIMO receiver DSP, which is necessary to uncouple the signals after transmission. GDS was defined by Ho and Kahn as the difference between maximum and minimum GDs [94], while the formula derived in Ref. [95] relates the GDS to the fiber geometry and to the statistical properties of the structural fiber perturbations. In [Paper C] we proposed to use the average

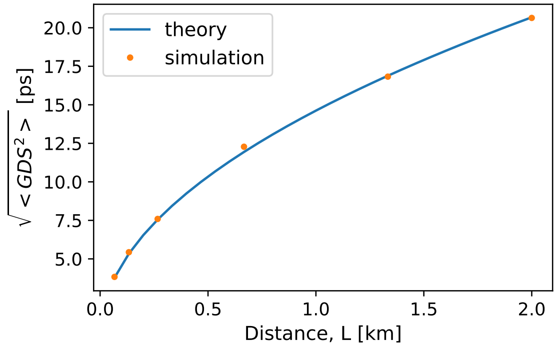

Figure 4.23: Calculated dependence of averaged GDS on propagation distance in the 3CCF.

of the squared eigenvalues $\tau_{\mathrm{tot},k}$ of the delay operator (GDs), i.e.

$$\langle GDS^2 \rangle = \frac{1}{D} \sum_{k=1}^{D} \langle \tau_{\mathrm{tot},k}^2 \rangle. \tag{4.65}$$

In a concatenation of N, D-dimensional delay matrices, this can be calculated exactly as [94]

$$\langle GDS^2 \rangle = \sum_{m=1}^{N} \sum_{k=1}^{D} \frac{\langle \tau_{km}^2 \rangle}{D}, \tag{4.66}$$

where τ_{km} denotes the k^{th} eigenvalue of the delay operator of element m. In the ideal case of an unperturbed CCF discussed in Section 4.2, GDS can be evaluated by (4.59). The benefits of using this metric for GDS is twofold: (i) it scales exactly linearly with fiber length and, (ii) it equals the RMS intensity impulse response averaged over all modes, as was shown in [Paper C]:

$$\langle T_{RMS}^2 \rangle_{theory} = \langle GDS^2 \rangle + T_{RMS_0}^2, \tag{4.67}$$

where T_{RMS_0} is the RMS width of the input Gaussian pulse. It also should be noted that this relation for GDS is closely related to the mean-square length of the generalized PMD vector defined in [108].

Calculation of the GDS was discussed in [Paper C] and [Paper D], where we investigated how it scales with distance in the 4CCF-1. Fig. 4.23 shows calculated GDS for the 3CCF. The theoretical curve is calculated with (4.59), while the simulation graph was obtained with (4.66). It is clearly seen that the curves are in good agreement and manifest a square root behavior on propagation distance, as expected for CCFs.

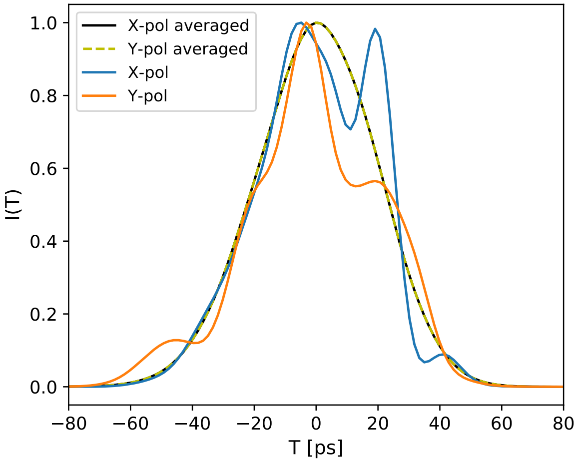

Figure 4.24: Normalized total power IIR calculated for the 3CCF. Blue and orange lines are related to the instances where a 8-ps Gaussian pulse is injected to x- and y-polarizations of the first core for a single realization. The black and yellow curves are the IIRs averaged over 200 realizations.

Impulse response

The impulse response of a fiber can be studied in simulations by exciting each of the core by a short Gaussian pulse and observing the received intensities in each of the cores and polarizations. A Gaussian pulse in time domain can be expressed as

$$u(T) = \exp(-\frac{T^2}{2T_0^2}), \tag{4.68}$$

where T is the time coordinate and T_0 is the 1/e half-width of the pulse power.

If a pulse enters a fiber, the output complex amplitude can be expressed as

$$\vec{A}(T) = \mathcal{F}^{-1}[\mathbf{T_{tot}}(\omega)\vec{A_0}\mathcal{F}[u(T)]], \tag{4.69}$$

where $\mathcal{F}[x]$ is the Fourier transform of x. The total power IIR then can be calculated as $I(T) = \vec{A}^H(T)\vec{A}(T)$.

The total power IIRs calculated for light coupled to the first 3CCF's core are shown in Fig. 4.24. Blue and orange lines denote the IIRs calculated when a 8 ps Gaussian pulse is injected to x- and y-polarizations

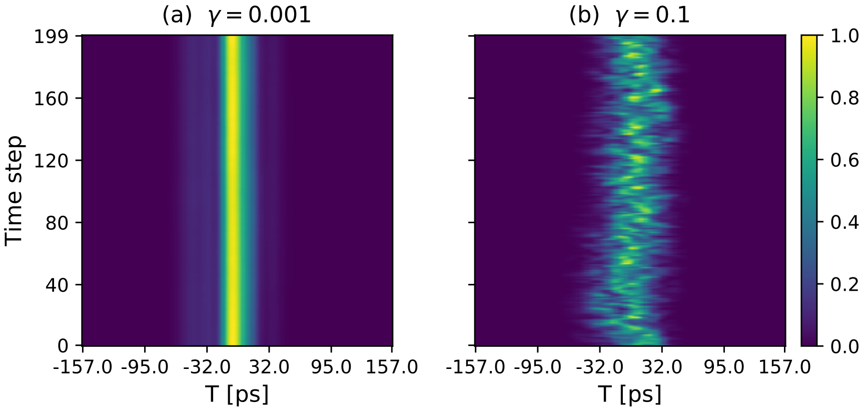

Figure 4.25: Dynamic evolution of the normalized total power IIR at (a) $\gamma = 0.001$ and (b) $\gamma = 0.1$.

respectively. The total power IIRs averaged over 200 realizations are shown by the black and yellow curves. The RMS width of the averaged impulse response agrees with the measured result in [Paper A], showing that the way of calculation of L_d for a specific CCF in the proposed random coupling model is accurate. It is evident that the polarization of the input state impacts the shape of the IIR, while on average the Gaussian shape is retained. This illustrates the importance of birefringence effects when analysing real-time behavior or single measurements. The same conclusions were obtained in [Paper C], and [Paper D], [Paper F] for 4CCF-1 and 4CCF-2.

In [Paper C] we investigated how the IIR of the 3CCF changes with number of fiber concatenations N. For $N = 1$ there are two distinct peaks separated by 183 ps, which corresponds to a GDS defined as the difference between maximum and minimum GDs [94] and agrees well with calculation presented in Section 4.2.3. As we increase the number of concatenations, there appear more peaks that move closer to the central position and the impulse response starts to be Gaussian-shaped at $N = 20$, which almost corresponds to the chosen length of one concatenation, L_d, in this Section. We also studied the dependence of the RMS width on the number of concatenations N. The results showed good agreement with theoretical estimates defined by (4.67).

The time evolution of the normalized total power IIRs calculated for two different γ parameters is shown in Fig. 4.25. The IIRs are calculated when a 8 ps Gaussian pulse enters X-polarization of the first core. The

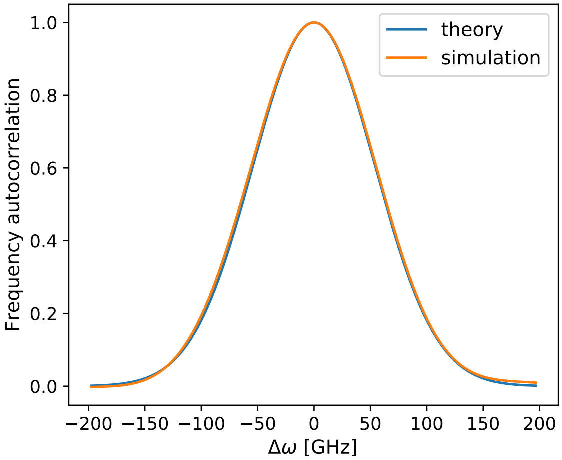

Figure 4.26: Theoretical and modeled frequency ACFs of the 3CCF.

value of γ parameter controls how fast IIR evolves. It can be seen that the IIR at $\gamma = 0.1$ in Fig. 4.25 (b) experience fast changes during the propagation, while the IIR in Fig. 4.25 (a) for $\gamma = 0.001$ shows a stable behavior with much slower decorrelation. The dynamic behavior of the IIR was also studied for 4CCF-2 in [Paper F], where the change in the shape of the responses can be also observed.

Frequency and time autocorrelation functions

The similarity between transfer matrices at various discrete points is quantified through the correlation coefficient $\alpha \in [0, 1]$, where $\alpha = 0$ indicates that two matrices are completely uncorrelated (independent) and the highest correlation corresponds to $\alpha = 1$.

The frequency ACF can be calculated as

$$\alpha_\omega(\Delta\omega) = \frac{1}{D} Tr\{< \mathbf{T}^{\dagger}_{\mathbf{tot}}(\omega' + \Delta\omega)\mathbf{T}_{\mathbf{tot}}(\omega') >\}, \tag{4.70}$$

where ω' is a chosen frequency at which the ACF is calculated, $\Delta\omega = \omega_l - \omega'$, and Tr is the trace operation and triangular brackets refer to the averaging over realizations of calculation of $\mathbf{T}^{\dagger}_{\mathbf{tot}}(\omega' + \Delta\omega)\mathbf{T}_{\mathbf{tot}}(\omega')$.

The analytical expression for the frequency ACF is derived in Appendix of [Paper F] as

$$\alpha_{\omega_{th}}(\Delta\omega) = \exp(-\langle GDS^2 \rangle \frac{\Delta\omega^2}{2}). \tag{4.71}$$

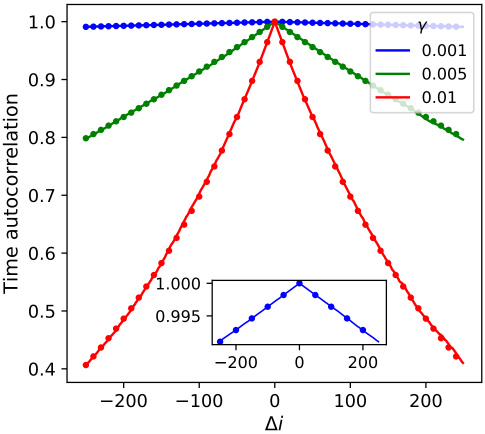

Figure 4.27: Time ACFs of the 3CCF for different γ parameters. The theoretical curves are indicated by dots. Inset shows zoomed in version of the time ACF for $\gamma = 0.001$.

Fig. 4.26 represents analytical and simulated frequency ACFs of the 3CCF. The simulation was performed over the wavelength range [1545, 1545.5] nm and averaged over 200 realizations. There is a good agreement between the modeling result calculated using (4.70) and the analytical curve obtained from (4.71). The frequency ACF for 4CCF-2 was investigated in [Paper F] and showed similar behavior and good agreement between theory and simulation.

The ACF in time is defined as

$$\alpha_t(\Delta t) = \frac{1}{D} Tr\{< \mathbf{T}^{\dagger}_{\mathbf{tot}}(t' + \Delta t)\mathbf{T}_{\mathbf{tot}}(t') >\}, \tag{4.72}$$

where t' is a chosen time point at which ACF is calculated and $\Delta t = t_i - t'$. As $t_i = i \cdot \delta t$, then $\Delta t = \delta t(i - i') = \delta t \Delta i$.

Let us consider $\delta t = 1$ for simplicity, then the above equation can be rewritten for the time step as

$$\alpha_t(\Delta i) = \frac{1}{D} Tr\{< \mathbf{T}^{\dagger}_{\mathbf{tot}}(i' + \Delta i)\mathbf{T}_{\mathbf{tot}}(i') >\}. \tag{4.73}$$

and the analytical result can be found as

$$\alpha_{t_{th}}(\Delta i) = \exp(-\gamma^2 |\Delta i| \frac{D}{2} N), \tag{4.74}$$

which is derived in Appendix of [Paper F].

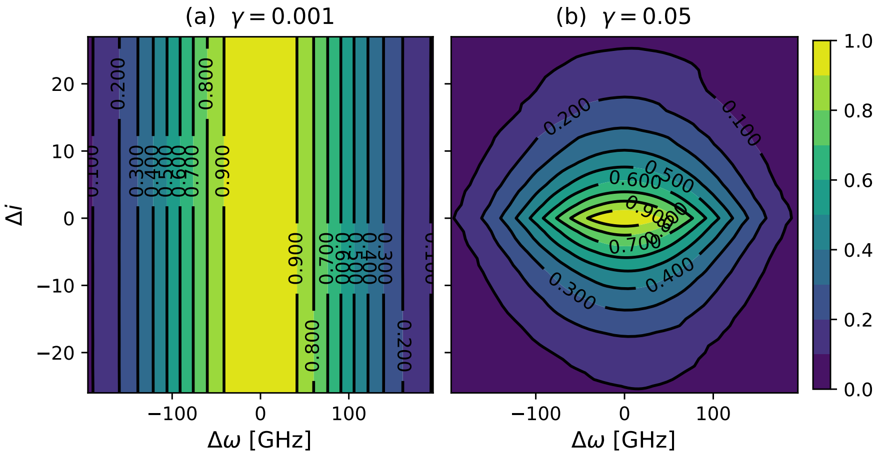

Figure 4.28: 2D ACF of the 3CCF calculated at (a) $\gamma = 0.001$ and (b) $\gamma = 0.05$.

Fig. 4.27 demonstrates time ACFs of the 3CCF for different γ parameters. Simulated curves are calculated according to (4.73) and averaged over 200 realizations of transfer matrices. Theoretical curves are calculated with (4.74) and show good agreement with the simulation. As expected, the functions at higher γ parameter exhibit faster decorrelation, while the ACF at $\gamma = 0.001$ shows smooth behavior close to linear dependence.

Another way of looking on time and frequency ACFs is 2D ACF, which can be calculated as

$$\alpha_{2D}(\Delta\omega, \Delta i) = \alpha_\omega(\Delta\omega)\alpha_t^\top(\Delta i). \tag{4.75}$$

Fig. 4.28 show 2D ACFs of the 3CCF calculated with (4.75) for $\gamma = 0.001$ and $\gamma = 0.05$ respectively. Simulation was performed using the wavelength range of [1545,1545.3] nm with 100 points, and the result was averaged over 100 realizations. As can be seen, this is just another representation of the ACF discussed above. Estimated 2D ACF can help to investigate necessary parameters of the model in both time and frequency and connect them to the properties of the real, installed fiber.

4.3.5 Final remarks

The simulations presented in the previous section show a good agreement with the theoretical and experimental results for the 3CCF obtained

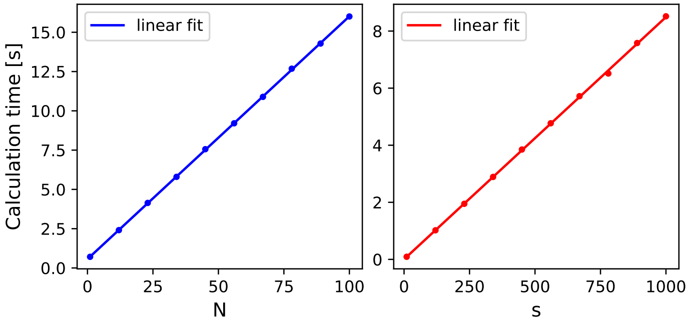

Figure 4.29: Computational time of the 3CCF's transfer function in the vector case of the static random coupling model depending on the number of concatenations N and frequency points s.

in [Paper A], while the simulation results on the 4CCF-2 discussed in [Paper F] also agree well with the theory and experimental data [113,198]. This highlights the applicability of proposed random coupling models for various purposes in fiber optic communication.

It should be noted that the computational complexity for the performed simulations grows linearly with the increasing number of concatenations, N, frequency s, and time n points, as shown in Fig. 4.29. The number of dimensions D also impacts the computational time. Hence, modeling of long CCF links with a high core count might be time-consuming. Averaging operations over many realizations might also take a long time. It is thus desirable to use an optimized code structure for testing and following the calculation. The simplest thing is setting up a logger in the simulation code, which assists in keeping track of the calculation steps, timing and helps with possible debugging. An example of such logger can be found in the file with the used functions in Ref. 22 of [Paper F].

CHAPTER 5

Future outlook

There are numerous research topics related to this thesis that can be investigated in later work. We will likely see that SDM fibers will be commercially deployed in the future and while the best platform is still undecided, CCFs are very promising candidates. Thus, modeling and characterisation will become more and more important because we will try to optimise fibers and devices even further to approach the data capacity limits. The purpose of this chapter is to briefly discuss research opportunities that are particularly connected to the work presented in Papers A-F.

Some of the advanced experimental techniques for SDM systems characterisation were discussed in Chapter 2. While extensively described DCS and SWI represent many advantages, we show in [Paper A] and [Paper B] that it is beneficial to use a combination of these two schemes, DC-SWI. Application of the tunable laser source that sweeps over the comb repetition rate provides fast and accurate full-field characterisation measurements without any additional interferometer for laser sweep nonlinearity compensation. The experimental results in [Paper B] demonstrate that DC-SWI enables extraction of transfer functions in a good agreement with the applied filters. These results show that DC-SWI can be used as a tool for measuring the amplitude and phase of the transfer function and extracting the parameters of interest for various samples. Possible research opportunities of DC-SWI unite DCS and SWI practical applications and can include metrology, optical imaging, *etc.* Moreover, the findings of [Paper A] demonstrate that DC-SWI is a promising method for characterising complex DUTs with rapid changes in transfer matrix elements. One of the possible applications in the future can be a combination of DC-SWI with an imaging experimental technique in order to obtain not only the full complex transfer function, but also information about the mode shape.

Additional investigations can be carried out to improve the DC-SWI implementation in terms of the scanning speed of the intermediate frequencies. The simplest way is to use a faster tunable laser. Another scenario is to employ an arbitrary waveform generator to produce a frequency sweep in the electrical domain, similar to the arrangement in [199], which might provide more linear tuning and much higher measurement speed.

Another important application of the DC-SWI lies in the domain of channel modeling for systems based on SDM. Information gained from characterisation measurements can be used in building the theoretical description of the fiber optic channel model. In Chapter 4 the effects of random coupling and their modeling in strongly coupled fibers were discussed. Existing and proposed models in Papers C-F can comprehensively describe many propagation properties, however, the a priori knowledge on time-frame changes of transfer matrix elements in a considered fiber can improve the models. The ultimate goal can be establishing even more realistic dynamic channel models that include many rapidly changing events such as phase noise and nonlinear impairments.

The proposed channel models can be applied further to test MIMO equalizers in various dynamic links as has been done in [Paper E]. As a possible novelty, the equalizer can be also tested for various frequencies with the model presented in [Paper F]. As the frequency range and the time fluctuations rate can be easily changed in the proposed model, it brings a lot of flexibility in the test process. This can be especially relevant for modelling of long-haul real-time transmission experiments [113, 114].

CHAPTER 6

Summary of papers

Paper A
Characterisation of a Coupled-Core Fiber Using Dual-Comb Swept-Wavelength Interferometry
Presented at European Conference on Optical Communication (ECOC), Bordeaux, France, Sep, 2021.

In this paper we demonstrate transfer function measurements of the three coupled-core fiber performed with the DC-SWI, which is described in detail in [Paper B]. Using the extracted RMS-widths from the impulse response functions, values of DMGDs for every core is estimated.

My contribution: I constructed a part of the setup, carried out measurements, DSP and experimental analysis, prepared the figures and wrote the paper. I presented the results at ECOC 2021.

Paper B
Dual-Comb Swept-Wavelength Interferometry: Theory and Experiment
Journal of Lightwave Technology, vol. 40, no. 19, pp. 6508-6516, Oct, 2022

In this article we comprehensively describe a measurement technique which combines DCS and SWI, and demonstrate characterisation measurements over 1.25 THz bandwidth performed with the frequency resolution superior to the DCS. Experimental advantages are gained by using a tunable laser source in order to sweep over the the frequency comb spacing and capture all intermediate frequencies. Moreover, employed DSP algorithms enable compensation of the laser sweep without any external interferometer.

My contribution: I constructed a part of the setup, carried out measurements, DSP and experimental analysis, prepared the figures and wrote the paper.

Paper C

Modeling of 3-Coupled-Core Fiber: Comparison Between Scalar and Vector Random Coupling Models

Journal of Lightwave Technology, vol. 42, no. 2, pp. 793-801, Jan, 2024

In this work we present for the first time, to the best of our knowledge, a comparative analysis between scalar and vector models for a 3CCF. We derive for the first time an analytically tractable vector model of the supermodes for an unperturbed 3CCF, accounting for the birefringence from the presence of nearby cores. The model is extended to account for the effects of random mode coupling and analyze the impulse response as well GDs in a 3CCF by using the concatenated waveplate model. Comparisons with measured impulse responses [Paper A] then enable an estimate of the correlation length of the fiber.

My contribution: I implemented and analyzed the model, carried out simulations and calculations, prepared the figures and wrote the paper.

Paper D

Analysis of the Scalar and Vector Random Coupling Models For a Four Coupled-Core Fiber

European Conference on Optical Communication (ECOC), Glasgow, UK, Oct. 2023

In this work we present a comparative analysis of the scalar and vector random coupling models for a 4CCF in the ideal case and random coupling regime. We show for the first time, to the best of our knowledge, analytically calculated supermodes and their propagation constants for a 4CCF in a polarization multiplexed case.

My contribution: I implemented and analyzed the model, carried out simulations and calculations, prepared the figures and wrote the paper.

Paper E
Circuit Implementation of Pilot-Based Dynamic MIMO Equalization for Coupled-Core Fibers
Optical Fiber Communications Conference, San Diego, March 2024

In this article we explore ASIC implementation for pilot-based MIMO equalizers for coupled-core transmission, considering chip area scaling trends and performance impact of time-dependent drift. Our channel model was central in the simulations of the equalizer performance.

My contribution: I implemented and analyzed the time-drift model used to test the equalizer.

Paper F
Dynamic Model For Coupled-Core Fibers
Journal of Lightwave Technology, submitted

In this article we design a dynamic (time dependent) model for CCFs, which contains a static frequency dependent part presented in [Paper C] and time-drift part used in [Paper E]. Simulation and analytical results for impulse response, group delays and autocorrelation functions are shown for a 4CCF.

My contribution: I implemented and analyzed the model, carried out simulations and calculations, prepared the figures and wrote the paper.

References

[1] B. I. Hirschowitz, "Photography through the fiber gastroscope," *The American journal of digestive diseases*, vol. 8, no. 5, pp. 389–395, 1963.

[2] R. S. Kerdock and D. H. Wolaver, "Atlanta fiber system experiment: results of the atlanta experiment," *The Bell System Technical Journal*, vol. 57, no. 6, pp. 1857–1879, 1978.

[3] C. E. Shannon, "A mathematical theory of communication," *The Bell System Technical Journal*, vol. 27, no. 3, pp. 379–423, 1948.

[4] R. Ryf, A. Sierra, R.-J. Essiambre, A. H. Gnauck, S. Randel, M. Esmaeelpour, S. Mumtaz, P. J. Winzer, R. Delbue, P. Pupalaikis, A. Sureka, T. Hayashi, T. Taru, and T. Sasaki, "Coherent 1200-km 6 × 6 MIMO mode-multiplexed transmission over 3-core microstructured fiber," in *37th European Conference and Exposition on Optical Communications*, 2011, p. Th.13.C.1.

[5] N. K. Fontaine, R. Ryf, H. Chen, A. V. Benitez, J. E. A. Lopez, R. A. Correa, B. Guan, B. Ercan, R. P. Scott, S. J. B. Yoo, L. Grüner-Nielsen, Y. Sun, and R. J. Lingle, "30×30 MIMO transmission over 15 spatial modes," in *Optical Fiber Communication Conference Post Deadline Papers*, 2015, p. Th5C.1.

[6] T. Hayashi, T. Sakamoto, Y. Yamada, R. Ryf, R.-J. Essiambre, N. Fontaine, M. Mazur, H. Chen, and T. Hasegawa, "Randomly-

coupled multi-core fiber technology," *Proceedings of the IEEE*, vol. 110, no. 11, pp. 1786–1803, 2022.

[7] K.-P. Ho and J. M. Kahn, "Mode coupling and its impact on spatially multiplexed systems," in *Optical Fiber Telecommunications*, 6th ed. Boston: Academic Press, 2013, pp. 491–568.

[8] F. P. Kapron, D. B. Keck, and R. D. Maurer, "Radiation losses in glass optical waveguides," *Applied Physics Letters*, vol. 17, no. 10, pp. 423–425, 1970.

[9] E. Chinnock, L. Cohen, W. Holden, R. Standley, and D. Keck, "The length dependence of pulse spreading in the CGW-Bell-10 optical fiber," *Proceedings of the IEEE*, vol. 61, no. 10, pp. 1499–1500, 1973.

[10] L. G. Cohen, P. Kaiser, J. B. Mac Chesney, P. B. O'Connor, and H. M. Presby, "Transmission properties of a low-loss near-parabolic-index fiber," *Applied Physics Letters*, vol. 26, no. 8, pp. 472–474, 1975.

[11] L. G. Cohen and H. M. Presby, "Shuttle pulse measurements of pulse spreading in a low loss graded-index fiber," *Applied Optics*, vol. 14, no. 6, pp. 1361–1363, 1975.

[12] D. Gloge, E. L. Chinnock, and T. P. Lee, "GaAs Twin-Laser Setup to Measure Mode and Material Dispersion in Optical Fibers," *Applied Optics*, vol. 13, no. 2, pp. 261–263, 1974.

[13] L. G. Cohen and C. Lin, "Pulse delay measurements in the zero material dispersion wavelength region for optical fibers," *Applied Optics*, vol. 16, no. 12, pp. 3136–3139, 1977.

[14] L. Cohen and C. Lin, "A universal fiber-optic (UFO) measurement system based on a near-IR fiber Raman laser," *IEEE Journal of Quantum Electronics*, vol. 14, no. 11, pp. 855–859, 1978.

[15] C. Lin, A. R. Tynes, A. Tomita, P. L. Liu, and D. L. Philen, "Chromatic dispersion measurements in single-mode fibers using picosecond InGaAsP injection lasers in the 1.2- to 1.5-μm spectral region," *The Bell System Technical Journal*, vol. 62, no. 2, pp. 457–462, 1983.

[16] K. Mori, T. Morioka, and M. Saruwatari, “Group velocity dispersion measurement using supercontinuum picosecond pulses generated in an optical fibre,” *Electron. Lett*, vol. 29, no. 12, pp. 987–989, 1993.

[17] N. Nishizawa, A. Muto, and T. Goto, “Measurement of chromatic dispersion of optical fibers using wavelength-tunable soliton pulses,” *Japanese Journal of Applied Physics*, vol. 39, no. 8, pp. 4990–4992, 2000.

[18] M. Mazur, N. K. Fontaine, R. Ryf, H. Chen, and A. Blanco-Redondo, “Impulse response measurement of a few-mode fiber using superconducting nanowire single-photon detectors,” in *European Conference on Optical Communication (ECOC)*, 2021, p. Tu3A.3.

[19] C. Baker, Y. Lu, and X. Bao, “Chromatic-dispersion measurement by modulation phase-shift method using a Kerr phase-interrogator,” *Optics Express*, vol. 22, no. 19, pp. 22 314–22 319, 2014.

[20] W. Wieser, B. R. Biedermann, T. Klein, C. M. Eigenwillig, and R. Huber, “Ultra-rapid dispersion measurement in optical fibers,” *Optics Express*, vol. 17, no. 25, pp. 22 871–22 878, 2009.

[21] F. Devaux, Y. Sorel, and J. Kerdiles, “Simple measurement of fiber dispersion and of chirp parameter of intensity modulated light emitter,” *Journal of Lightwave Technology*, vol. 11, no. 12, pp. 1937–1940, 1993.

[22] C. Mazzali, D. Grosz, and H. Fragnito, “Simple method for measuring dispersion and nonlinear coefficient near the zero dispersion wavelength of optical fibers,” *IEEE Photonics Technology Letters*, vol. 11, no. 2, pp. 251–253, 1999.

[23] L. F. Mollenauer, P. V. Mamyshev, and M. J. Neubelt, “Method for facile and accurate measurement of optical fiber dispersion maps,” *Optics Letters*, vol. 21, no. 21, pp. 1724–1726, 1996.

[24] A. L. Schawlow and C. H. Townes, “Infrared and optical masers,” *Physical Review*, vol. 112, pp. 1940–1949, Dec 1958.

[25] T. H. Mainman, “Stimulated optical radiation in ruby,” *Nature*, vol. 187, no. 4736, pp. 493–494, 1960.

[26] A. Javan, W. R. Bennett, and D. R. Herriott, “Population inversion and continuous optical maser oscillation in a gas discharge containing a He-Ne mixture,” *Physical Review Letters*, vol. 6, pp. 106–110, 1961.

[27] L. E. Hargrove, R. L. Fork, and M. A. Pollack, “Locking of He-Ne laser modes induced by synchronous intracavity modulation,” *Applied Physics Letters*, vol. 5, no. 1, pp. 4–5, 1964.

[28] V. Durán, P. A. Andrekson, and V. Torres-Company, “Electro-optic dual-comb interferometry over 40 nm bandwidth,” *Optics Letters*, vol. 41, no. 18, p. 4190, 2016.

[29] A. Ishizawa, T. Nishikawa, M. Yan, G. Millot, H. Gotoh, T. Hänsch, and N. Picqué, “Optical frequency combs of multi-GHz line-spacing for real-time multi-heterodyne spectroscopy,” in *Conference on Lasers and Electro-Optics (CLEO)*, 2015, p. SW1G.7.

[30] D. A. Long, A. J. Fleisher, K. O. Douglass, S. E. Maxwell, K. Bielska, J. T. Hodges, and D. F. Plusquellic, “Multiheterodyne spectroscopy with optical frequency combs generated from a continuous-wave laser,” *Optics Letters*, vol. 39, no. 9, pp. 2688–2690, 2014.

[31] V. R. Supradeepa, C. M. Long, D. E. Leaird, and A. M. Weiner, “Fast characterization of dispersion and dispersion slope of optical fiber links using spectral interferometry with frequency combs,” *IEEE Photonics Technology Letters*, vol. 22, no. 3, pp. 155–157, 2010.

[32] M. Soriano-Amat, “Time-expanded phase-sensitive optical time-domain reflectometry,” *Light: Science & Applications*, no. 10, pp. 1–12, 2021.

[33] A. Asahara, T. Adachi, S. Akiyama, and K. Minoshima, “Spatiotemporal characterization of optical vortex light-wave using hyperspectral dual-comb imaging,” in *Conference on Lasers and Electro-Optics (CLEO)*, 2020, p. STu4N.6.

[34] M. Mazur, N. K. Fontaine, S. Corteselli, H. Chen, L. Dallachiesa, T. Hayashi, H. Sakuma, T. Hasegawa, R. Ryf, and D. T. Neilson, "Comparison of transfer matrix stability between a 110 km 7-core coupled-core multi-core fiber and single-mode fiber," in *Optical Fiber Communications Conference and Exhibition (OFC)*, 2022, p. M1E.2.

[35] D. R. Carlson, D. D. Hickstein, and S. B. Papp, "Broadband, electro-optic, dual-comb spectrometer for linear and nonlinear measurements," *Optics Express*, vol. 28, no. 20, pp. 29 148–29 154, 2020.

[36] E. L. Teleanu, V. Durán, and V. Torres-Company, "Electro-optic dual-comb interferometer for high-speed vibrometry," *Optics Express*, vol. 25, no. 14, pp. 16 427–16 436, 2017.

[37] P. Martín-Mateos, F. U. Khan, and O. E. Bonilla-Manrique, "Direct hyperspectral dual-comb imaging," *Optica*, vol. 7, no. 3, pp. 199–202, 2020.

[38] C. Poole, N. Bergano, R. Wagner, and H. Schulte, "Polarization dispersion and principal states in a 147-km undersea lightwave cable," *Journal of Lightwave Technology*, vol. 6, no. 7, pp. 1185–1190, 1988.

[39] B. Heffner, "Automated measurement of polarization mode dispersion using jones matrix eigenanalysis," *IEEE Photonics Technology Letters*, vol. 4, no. 9, pp. 1066–1069, 1992.

[40] W. Eickhoff and R. Ulrich, "Optical frequency domain reflectometry in single-mode fiber," *Applied Physics Letters*, vol. 39, no. 9, pp. 693–695, 1981.

[41] B. J. Soller, D. K. Gifford, M. S. Wolfe, and M. E. Froggatt, "High resolution optical frequency domain reflectometry for characterization of components and assemblies," *Optics Express*, vol. 13, no. 2, pp. 666–674, 2005.

[42] J. von der Weid, R. Passy, G. Mussi, and N. Gisin, "On the characterization of optical fiber network components with optical frequency domain reflectometry," *Journal of Lightwave Technology*, vol. 15, no. 7, pp. 1131–1141, 1997.

[43] M. Froggatt and J. Moore, "High-spatial-resolution distributed strain measurement in optical fiber with Rayleigh scatter," *Applied Optics*, vol. 37, no. 10, pp. 1735–1740, 1998.

[44] D. K. Gifford, M. E. Froggatt, and S. T. Kreger, "High precision, high sensitivity distributed displacement and temperature measurements using OFDR-based phase tracking," in *21st International Conference on Optical Fiber Sensors*, vol. 7753, 2011, pp. 536–539.

[45] D.-P. Zhou, Z. Qin, W. Li, L. Chen, and X. Bao, "Distributed vibration sensing with time-resolved optical frequency-domain reflectometry," *Optics Express*, vol. 20, no. 12, pp. 13 138–13 145, 2012.

[46] R. Veronese, N. K. Fontaine, H. Chen, M. Mazur, R. Ryf, M. Santagiustina, A. Galtarossa, and L. Palmieri, "Experimental characterization of group and phase delays induced by bending and twisting in multi-core fibers," *Opt. Lett.*, vol. 46, no. 11, pp. 2674–2677, Jun 2021.

[47] E. Baumann, F. R. Giorgetta, I. Coddington, L. C. Sinclair, K. Knabe, W. C. Swann, and N. R. Newbury, "Comb-calibrated frequency-modulated continuous-wave ladar for absolute distance measurements," *Optics Letters*, vol. 38, no. 12, pp. 2026–2028, 2013.

[48] L. E. Smith, M. Bonesi, R. Smallwood, S. J. Matcher, and S. MacNeil, "Using swept-source optical coherence tomography to monitor the formation of neo-epidermis in tissue-engineered skin," *Journal of Tissue Engineering and Regenerative Medicine*, vol. 4, no. 8, pp. 652–658, 2010.

[49] N. K. Fontaine, R. Ryf, M. A. Mestre, B. Guan, X. Palou, S. Randel, Y. Sun, L. Grüner-Nielsen, R. V. Jensen, and R. Lingle, "Characterization of space-division multiplexing systems using a swept-wavelength interferometer," in *Optical Fiber Communication Conference*, 2013, p. OW1K.2.

[50] J. van Weerdenburg, S. Rommel, J. M. D. Mendinueta, W. Klaus, J. Sakaguchi, J. J. Vegas Olmos, T. Koonen, Y. Awaji, I. T. Monroy, C. Okonkwo, and N. Wada, "Enhanced modal dispersion estimation enabled by chromatic dispersion compensation in optical

vector network analysis," *Journal of Lightwave Technology*, vol. 37, no. 16, pp. 4001–4007, 2019.

[51] J. Carpenter, B. J. Eggleton, and J. Schröder, "Reconfigurable spatially-diverse optical vector network analyzer," *Optics Express*, vol. 22, no. 3, pp. 2706–2713, 2014.

[52] M. Mazur, N. K. Fontaine, R. Ryf, H. Chen, D. T. Neilson, M. Bigot-Astruc, F. Achten, P. Sillard, A. Amezcua-Correa, J. Schröder, and J. Carpenter, "Characterization of long multimode fiber links using digital holography," in *Optical Fiber Communication Conference (OFC)*, 2019, p. W4C.5.

[53] J. Bohn, J. Carpenter, S. Gross, M. Withford, and J. Schröder, "Characterization of laser inscribed on-chip photonic lanterns with different core distances," in *European Conference on Optical Communication (ECOC)*, 2015, p. P.1.14.

[54] S. Rommel, J. M. D. Mendinueta, W. Klaus, J. Sakaguchi, J. J. V. Olmos, Y. Awaji, I. T. Monroy, and N. Wada, "Few-mode fiber, splice and SDM component characterization by spatially-diverse optical vector network analysis," *Optics Express*, vol. 25, no. 19, pp. 22 347–22 361, 2017.

[55] D. Gabor, "A new microscopic principle," *Nature*, vol. 161, no. 4098, pp. 777–778, 1948.

[56] T. Kubota, "48 Years with holography," *Optical Review*, vol. 21, no. 6, pp. 883–892, 2014.

[57] J. W. Goodman and R. W. Lawrence, "Digital image formation from electronically detected holograms," *Applied Physics Letters*, vol. 11, no. 3, pp. 77–79, 1967.

[58] T. Tahara, X. Quan, R. Otani, Y. Takaki, and O. Matoba, "Digital holography and its multidimensional imaging applications: a review," *Microscopy*, vol. 67, no. 2, pp. 55–67, 2018.

[59] S. van der Heide, B. van Esch, M. van den Hout, T. Bradley, A. M. Velazquez-Benitez, N. K. Fontaine, R. Ryf, H. Chen, M. Mazur, J. E. Antonio-Lopez, J. C. Alvarado-Zacarias, R. Amezcua-Correa, and C. Okonkwo, "Optical field characterization using off-axis digital holography," in *Optical Fiber Communications Conference and Exhibition (OFC)*, 2022, p. M3Z.6.

[60] J. C. Alvarado-Zacarias, N. K. Fontaine, R. Ryf, H. Chen, S. van der Heide, J. E. Antonio-Lopez, S. Wittek, G. Li, C. Okonkwo, M. Bigot-Astruc, A. Amezcua-Correa, P. Sillard, and R. Amezcua-Correa, "Assembly and characterization of a multimode edfa using digital holography," in *Optical Fiber Communication Conference (OFC)*, 2020, p. Th1H.6.

[61] S. P. van der Heide, "Space-division multiplexed optical transmission enabled by advanced digital signal processing," Ph.D. thesis, Eindhoven University of Technology, 2022.

[62] E. Biglieri, J. Proakis, and S. Shamai, "Fading channels: information-theoretic and communications aspects," *IEEE Transactions on Information Theory*, vol. 44, no. 6, pp. 2619–2692, 1998.

[63] A. Al-Kinani, C.-X. Wang, L. Zhou, and W. Zhang, "Optical wireless communication channel measurements and models," *IEEE Communications Surveys & Tutorials*, vol. 20, no. 3, pp. 1939–1962, 2018.

[64] E. Agrell and M. Karlsson, "Power-efficient modulation formats in coherent transmission systems," *Journal of Lightwave Technology*, vol. 27, no. 22, pp. 5115–5126, 2009.

[65] T. Mizuochi, K. Kubo, H. Yoshida, H. Fujita, H. Tagami, M. Akita, and K. Motoshima, "Next generation fec for optical transmission systems," in *Optical Fiber Communication Conference*, 2003, p. ThN1.

[66] G. P. Agrawal, *Nonlinear Fiber Optics*, 5th ed. Springer, 2013.

[67] R. Mears, L. Reekie, I. Jauncey, and D. Payne, "Low-noise erbium-doped fibre amplifier operating at 1.54 micrometers," *Electronics Letters*, vol. 23, no. 19, pp. 1026–1028, 1987.

[68] S. C. Rashleigh and R. Ulrich, "Polarization mode dispersion in single-mode fibers," *Opt. Lett.*, vol. 3, no. 2, pp. 60–62, Aug 1978.

[69] C. D. Poole and R. E. Wagner, "Phenomenological approach to polarisation dispersion in long single-mode fibres," *Electronics Letters*, vol. 22, pp. 1029–1030, 1986.

[70] H. Kogelnik, R. M. Jopson, and L. E. Nelson, "Polarization-mode dispersion," in *Optical Fiber Telecommunications IV-B*, 4th ed. Academic Press, 2002, pp. 725–861.

[71] G. Foschini and C. Poole, "Statistical theory of polarization dispersion in single mode fibers," *Journal of Lightwave Technology*, vol. 9, no. 11, pp. 1439–1456, 1991.

[72] M. Brodsky, N. J. Frigo, M. Boroditsky, and M. Tur, "Polarization mode dispersion of installed fibers," *J. Lightwave Technol.*, vol. 24, no. 12, pp. 4584–4599, Dec 2006.

[73] N. Gisin and B. Huttner, "Combined effects of polarization mode dispersion and polarization dependent losses in optical fibers," *Optics Communications*, vol. 142, no. 1, pp. 119–125, 1997.

[74] F. Curti, B. Daino, Q. Mao, F. Matera, and C. Someda, "Concatenation of polarisation dispersion in single-mode fibres," *Electronics Letters*, vol. 25, pp. 290–292(2), February 1989.

[75] N. Gisin and J. Pellaux, "Polarization mode dispersion: time versus frequency domains," *Optics Communications*, vol. 89, no. 2, pp. 316–323, 1992.

[76] M. Karlsson and J. Brentel, "Autocorrelation function of the polarization-mode dispersion vector," *Opt. Lett.*, vol. 24, no. 14, pp. 939–941, Jul 1999. [Online]. Available: https://opg.optica.org/ol/abstract.cfm?URI=ol-24-14-939

[77] M. Karlsson, "Probability density functions of the differential group delay in optical fiber communication systems," *J. Lightwave Technol.*, vol. 19, no. 3, p. 324, Mar 2001.

[78] R. C. Jones, "A new calculus for the treatment of optical systemsi. description and discussion of the calculus," *J. Opt. Soc. Am.*, vol. 31, no. 7, pp. 488–493, Jul 1941.

[79] S. Betti, F. Curti, G. De Marchis, and E. Iannone, "A novel multilevel coherent optical system: 4-quadrature signaling," *Journal of Lightwave Technology*, vol. 9, no. 4, pp. 514–523, 1991.

[80] R. Cusani, E. Iannone, A. Salonico, and M. Todaro, "An efficient multilevel coherent optical system: M-4Q-QAM," *Journal of Lightwave Technology*, vol. 10, no. 6, pp. 777–786, 1992.

[81] M. Karlsson, “Four-dimensional rotations in coherent optical communications,” *J. Lightwave Technol.*, vol. 32, no. 6, pp. 1246–1257, Mar 2014.

[82] M. Shtaif, “Performance degradation in coherent polarization multiplexed systems as a result of polarization dependent loss,” *Opt. Express*, vol. 16, no. 18, pp. 13 918–13 932, Sep 2008.

[83] K. Kikuchi, “Polarization-demultiplexing algorithm in the digital coherent receiver,” in *2008 Digest of the IEEE/LEOS Summer Topical Meetings*, 2008, pp. 101–102.

[84] S. J. Savory, “Digital filters for coherent optical receivers,” *Opt. Express*, vol. 16, no. 2, pp. 804–817, Jan 2008.

[85] C. Czegledi, M. Karlsson, E. Agrell, and P. Johanisson, “Polarization drift channel model for coherent fibre-optic systems,” *Sci Rep.*, vol. 6, no. 21217, pp. 1–11, Apr. 2016.

[86] C. B. Czegledi, “Modeling and compensation of polarization effects in fiber-optic communication systems,” Ph.D. thesis, Chalmers University of Technology, 2018.

[87] E. Agrell, G. Durisi, and P. Johannisson, “Information-theory-friendly models for fiber-optic channels: A primer,” in *2015 IEEE Information Theory Workshop (ITW)*, 2015, pp. 1–5.

[88] X. Shen, J. M. Kahn, and M. A. Horowitz, “Compensation for multimode fiber dispersion by adaptive optics,” *Optics Letters*, vol. 30, no. 22, pp. 2985–2987, 2005.

[89] S. Fan and J. M. Kahn, “Principal modes in multimode waveguides,” *Optics Letters*, vol. 30, no. 2, pp. 135–137, 2005.

[90] M. B. Shemirani, W. Mao, R. A. Panicker, and J. M. Kahn, “Principal modes in graded-index multimode fiber in presence of spatial- and polarization-mode coupling,” *Journal of Lightwave Technology*, vol. 27, no. 10, pp. 1248–1261, 2009.

[91] J. Carpenter, B. J. Eggleton, and J. Schröder, “Observation of eisenbud-wigner-smith states as principal modes in multimode fibre,” *Nature Photonics*, vol. 9, pp. 751–757, 2015.

[92] K.-P. Ho and J. M. Kahn, “Mode-dependent loss and gain: statistics and effect on mode-division multiplexing,” *Optics Express*, vol. 19, no. 17, pp. 16 612–16 635, 2011.

[93] J. M. Kahn, K.-P. Ho, and M. B. Shemirani, “Mode coupling effects in multi-mode fibers,” in *Optical Fiber Communication Conference*, 2012.

[94] K.-P. Ho and J. M. Kahn, “Statistics of group delays in multimode fiber with strong mode coupling,” *Journal of Lightwave Technology*, vol. 29, no. 21, pp. 3119–3128, 2011.

[95] C. Antonelli, A. Mecozzi, M. Shtaif, and P. J. Winzer, “Modeling and performance metrics of MIMO-SDM systems with different amplification schemes in the presence of mode-dependent loss,” *Opt. Express*, vol. 23, no. 3, pp. 2203–2219, Feb 2015.

[96] A. W. Snyder, “Coupled-mode theory for optical fibers,” *Journal of the Optical Society of America*, vol. 62, no. 11, pp. 1267–1277, 1972.

[97] A. Yariv, “Coupled-mode theory for guided-wave optics,” *IEEE Journal of Quantum Electronics*, vol. 9, no. 9, pp. 919–933, 1973.

[98] H. Renner, “Supermodes of optical fibre couplers,” *Optics Communications*, vol. 94, no. 6, pp. 574–588, 1992.

[99] K. S. Chiang, “Intermodal dispersion in two-core optical fibers,” *Opt. Lett.*, vol. 20, no. 9, pp. 997–999, May 1995.

[100] C. Guan, L. Yuan, Q. Dai, and F. Tian, “Supermodes analysis for linear-core-array microstructured fiber,” *Journal of Lightwave Technology*, vol. 27, no. 11, pp. 1741–1745, 2009.

[101] C. Xia, N. Bai, I. Ozdur, X. Zhou, and G. Li, “Supermodes for optical transmission,” *Optics Express*, vol. 19, no. 17, pp. 16 653–16 664, 2011.

[102] C. Xia, M. A. Eftekhar, R. A. Correa, J. E. Antonio-Lopez, A. Schülzgen, D. Christodoulides, and G. Li, “Supermodes in coupled multi-core waveguide structures,” *IEEE Journal of Selected Topics in Quantum Electronics*, vol. 22, no. 2, pp. 196–207, 2016.

[103] W. Ren, Z. Tan, and G. Ren, “Analytical formulation of supermodes in multicore fibers with hexagonally distributed cores,” *IEEE Photonics Journal*, vol. 7, no. 1, pp. 1–11, 2015.

[104] Z. Li, J. Liu, C. Xia, Z. Hou, and G. Zhou, “Supermode characteristics of nested multiple hollow-core anti-resonant fibers,” *Photonics*, vol. 9, no. 11, pp. 816–835, Oct 2022.

[105] B. J. Ávila, J. N. Hernández, S. M. T. Rodríguez, and B. M. Rodríguez-Lara, “Symmetric supermodes in cyclic multicore fibers,” *OSA Continuum*, vol. 2, no. 3, pp. 515–522, Mar 2019.

[106] K. Saitoh, “Multi-core fiber technology for SDM: Coupling mechanisms and design,” *Journal of Lightwave Technology*, vol. 40, no. 5, pp. 1527–1543, 2022.

[107] T. Fujisawa and K. Saitoh, “Group delay spread analysis of strongly coupled 3-core fibers: an effect of bending and twisting,” *Optics Express*, vol. 24, no. 9, pp. 9583–9591, 2016.

[108] C. Antonelli, A. Mecozzi, M. Shtaif, and P. J. Winzer, “Stokes-space analysis of modal dispersion in fibers with multiple mode transmission,” *Optics Express*, vol. 20, no. 11, pp. 11 718–11 733, 2012.

[109] C. Antonelli, A. Mecozzi, M. Shtaif, N. K. Fontaine, H. Chen, and R. Ryf, “Stokes-space analysis of modal dispersion of SDM fibers with mode-dependent loss: Theory and experiments,” *Journal of Lightwave Technology*, vol. 38, no. 7, pp. 1668–1677, 2020.

[110] A. M. Ortiz, C. García-Meca, F. J. Fraile-Peláez, F. Cortés-Juan, and R. L. Sáez, “Ultra-short pulse propagation model for multicore fibers based on local modes,” *Scientific Reports*, vol. 7, no. 16457, pp. 1–14, 2017.

[111] J. Yammine, A. Tandjè, M. Dossou, L. Bigot, and E. R. Andresen, “Time-dependence of the transmission matrix of a specialty few-mode fiber,” *APL Photonics*, vol. 4, no. 2, pp. 022 904–1–022 904–11, Feb 2019.

[112] K. Choutagunta, I. Roberts, and J. M. Kahn, “Efficient quantification and simulation of modal dynamics in multimode fiber links,” *J. Lightwave Technol.*, vol. 37, no. 8, pp. 1813–1825, Apr 2019.

[113] M. Mazur, R. Ryf, N. K. Fontaine, A. Marotta, E. Börjeson, L. Dallachiesa, H. Chen, T. Hayashi, T. Nagashima, T. Nakanishi, T. Morishima, F. Graziosi, L. Palmieri, D. T. Neilson, P. Larsson-Edefors, A. Mecozzi, and C. Antonelli, "Real-time mimo transmission over field-deployed coupled-core multi-core fibers," in *Proc. Opt. Fiber Commun. Conf*, 2022, p. Th4B.8.

[114] S. Beppu, M. Kikuta, K. Igarashi, H. Mukai, M. Shigihara, Y. Saito, D. Soma, H. Takahashi, N. Yoshikane, T. Tsuritani, I. Morita, and M. Suzuki, "Long-haul coupled 4-core fiber transmission over 7,200 km with real-time mimo dsp," *Journal of Lightwave Technology*, vol. 40, no. 6, pp. 1640–1649, 2022.

[115] R. Yadav, F. A. Barbosa, and F. M. Ferreira, "Modal dynamics for space-division multiplexing in multi-mode fibers," *J. Lightw. Technol*, 2024, early access.

[116] M. Sorokina and S. Turitsyn, "Regeneration limit of classical shannon capacity," *Nature Communications*, vol. 5, no. 3861, pp. 1–6, 2014.

[117] A. Bononi, R. Dar, M. Secondini, P. Serena, and P. Poggiolini, *Fiber Nonlinearity and Optical System Performance.* Cham: Springer International Publishing, 2020, pp. 287–351.

[118] E. Agrell, A. Alvarado, G. Durisi, and M. Karlsson, "Capacity of a nonlinear optical channel with finite memory," *Journal of Lightwave Technology*, vol. 32, no. 16, pp. 2862–2876, 2014.

[119] F. Poletti and P. Horak, "Description of ultrashort pulse propagation in multimode optical fibers," *J. Opt. Soc. Am. B*, vol. 25, no. 10, pp. 1645–1654, Oct 2008.

[120] C. Antonelli, A. Mecozzi, and M. Shtaif, "Modeling of linear and nonlinear coupling in multiple-mode fiber optic transmission with mimo signal processing," in *2012 Conference Record of the Forty Sixth Asilomar Conference on Signals, Systems and Computers (ASILOMAR)*, 2012, pp. 645–649.

[121] P. Poggiolini, G. Bosco, A. Carena, V. Curri, Y. Jiang, and F. Forghieri, "The GN-model of fiber non-linear propagation and its applications," *Journal of Lightwave Technology*, vol. 32, no. 4, pp. 694–721, 2014.

[122] G. Rademacher and K. Petermann, “Nonlinear Gaussian noise model for multimode fibers with space-division multiplexing,” *J. Lightwave Technol.*, vol. 34, no. 9, pp. 2280–2287, May 2016.

[123] P. Serena, C. Lasagni, A. Bononi, C. Antonelli, and A. Mecozzi, “The ergodic GN model for space-division multiplexing with strong mode coupling,” *Journal of Lightwave Technology*, vol. 40, no. 10, pp. 3263–3276, 2022.

[124] P. Serena, “Modeling of nonlinear distortion in space-division multiplexing,” in *2023 Optical Fiber Communications Conference and Exhibition (OFC)*, 2023, pp. 1–38.

[125] S. K. Turitsyn, J. E. Prilepsky, S. T. Le, S. Wahls, L. L. Frumin, M. Kamalian, and S. A. Derevyanko, “Nonlinear fourier transform for optical data processing and transmission: advances and perspectives,” *Optica*, vol. 4, no. 3, pp. 307–322, Mar 2017.

[126] P. Arora and S. Kumar, “Nonlinear impairments in fiber optic communication systems: Analytical review,” in *Futuristic Trends in Network and Communication Technologies*, P. K. Singh, M. Paprzycki, B. Bhargava, J. K. Chhabra, N. C. Kaushal, and Y. Kumar, Eds. Singapore: Springer Singapore, 2019, pp. 28–44.

[127] G. Keiser, *Optical Signal Attenuation and Dispersion.* Springer Singapore, 2021, pp. 93–145.

[128] G. P. Agrawal, *Fiber-Optic Communication Systems*, 5th ed. Wiley, 2021.

[129] J. N. Damask, *Polarization Optics in Telecommunications.* Springer, 2004.

[130] Y. Yamada, T. Sakamoto, M. Wada, S. Nozoe, Y. Sagae, Y. Yamashita, H. Izumita, K. Nakajima, and H. Tanioka, “Spatial mode dispersion control in a coupled mcf using high density cabling parameters,” in *Optical Fiber Communication Conference (OFC) 2020*, 2020, p. M4C.5.

[131] T. Hayashi, T. Nagashima, T. Nakanishi, T. Morishima, R. Kawawada, A. Mecozzi, and C. Antonelli, “Field-deployed multicore fiber testbed,” in *2019 24th OptoElectronics and Communications Conference (OECC) and 2019 International Conference on Photonics in Switching and Computing (PSC)*, 2019, pp. 1–3.

[132] T. Sakamoto, T. Mori, T. Yamamoto, and S. Tomita, "Differential mode delay managed transmission line for wide-band wdm-mimo system," in *Optical Fiber Communication Conference*, 2012, p. OM2D.1.

[133] P. Sillard, D. Molin, M. Bigot-Astruc, A. Amezcua-Correa, K. de Jongh, and F. Achten, "DMGD-compensated links," in *Optical Fiber Communication Conference*, 2017, p. Tu2J.4.

[134] R. Ryf, N. K. Fontaine, S. Wittek, K. Choutagunta, M. Mazur, H. Chen, J. Carlos Alvarado-Zacarias, R. Amezcua-Correa, M. Capuzzo, R. Kopf, A. Tate, H. Safar, C. Bolle, D. T. Neilson, E. Burrows, K. Kim, M. Bigot-Astruc, F. Achten, P. Sillard, A. Amezcua-Correa, J. M. Kahn, J. Schröder, and J. Carpenter, "High-spectral-efficiency mode-multiplexed transmission over graded-index multimode fiber," in *European Conference on Optical Communication (ECOC)*, 2018, p. Th3B.1.

[135] X. Zhao and F. Choa, "Demonstration of 10-Gb/s transmissions over a 1.5-km-long multimode fiber using equalization techniques," *IEEE Photonics Technology Letters*, vol. 14, no. 8, pp. 1187–1189, 2002.

[136] C. Antonelli and A. Mecozzi, "Near-zero modal-dispersion (nemo) coupled-core multi-core fibers," *J. Lightwave Technol.*, vol. 39, no. 23, pp. 7517–7528, Dec 2021.

[137] T. Mori, T. Sakamoto, M. Wada, T. Yamamoto, F. Yamamoto, and K. Nakajima, "Experimental verification of signal quality difference induced by differential modal loss and modal crosstalk on optical mimo transmission and its compensation by equipartition multiplexing," *Journal of Lightwave Technology*, vol. 34, no. 3, pp. 918–927, 2016.

[138] K. Shibahara, T. Mizuno, D. Lee, and Y. Miyamoto, "Signal processing techniques for DMD and MDL mitigation in dense SDM transmissions," in *Optical Fiber Communication Conference*, 2017, p. M2D.3.

[139] G. Rademacher, R. S. Luís, B. J. Puttnam, R. Ryf, S. van der Heide, T. A. Eriksson, N. K. Fontaine, H. Chen, R.-J. Essiambre, Y. Awaji, and H. Furukawa, "A comparative study of few-mode

fiber and coupled-core multi-core fiber transmission," *J. Lightwave Technol.*, vol. 40, no. 6, pp. 1590–1596, Mar 2022.

[140] T. Hasegawa and T. Hayashi, "Measurement of mode dependent loss of randomly-coupled multi-core fiber using scrambling method," in *26th Optoelectronics and Communications Conference*, 2021, p. T2C.2.

[141] R. S. B. Ospina, C. Okonkwo, and D. A. A. Mello, "DSP-based mode-dependent loss and gain estimation in coupled SDM transmission," in *Optical Fiber Communications Conference and Exhibition (OFC)*, 2020, p. W2A.47.

[142] K. Shibahara, T. Mizuno, D. Lee, and Y. Miyamoto, "Advanced MIMO signal processing techniques enabling long-haul dense SDM transmissions," *Journal of Lightwave Technology*, vol. 36, no. 2, pp. 336–348, 2018.

[143] J. W. Nicholson, A. D. Yablon, S. Ramachandran, and S. Ghalmi, "Spatially and spectrally resolved imaging of modal content in large-mode-area fibers," *Optics Express*, vol. 16, no. 10, pp. 7233–7243, 2008.

[144] S. Ramachandran, J. Nicholson, S. Ghalmi, and M. Yan, "Measurement of multipath interference in the coherent crosstalk regime," *IEEE Photonics Technology Letters*, vol. 15, no. 8, pp. 1171–1173, 2003.

[145] J. W. Nicholson, A. D. Yablon, J. M. Fini, and M. D. Mermelstein, "Measuring the modal content of large-mode-area fibers," *IEEE Journal of Selected Topics in Quantum Electronics*, vol. 15, no. 1, pp. 61–70, 2009.

[146] J. Bromage, J. M. Fini, C. Dorrer, and J. D. Zuegel, "Characterization and optimization of Yb-doped photonic-crystal fiber rod amplifiers using spatially resolved spectral interferometry," *Applied Optics*, vol. 50, no. 14, pp. 2001–2007, 2011.

[147] J. M. Fini, J. W. Nicholson, R. S. Windeler, E. M. Monberg, L. Meng, B. Mangan, A. DeSantolo, and F. V. DiMarcello, "Low-loss hollow-core fibers with improved single-modedness," *Optics Express*, vol. 21, no. 5, pp. 6233–6242, 2013.

[148] J. Kerttula, V. Filippov, V. Ustimchik, Y. Chamorovskiy, and O. G. Okhotnikov, “Mode evolution in long tapered fibers with high tapering ratio,” *Optics Express*, vol. 20, no. 23, pp. 25 461–25 470, 2012.

[149] J. F. Bauters, M. L. Davenport, M. J. R. Heck, J. K. Doylend, A. Chen, A. W. Fang, and J. E. Bowers, “Silicon on ultra-low-loss waveguide photonic integration platform,” *Optics Express*, vol. 21, no. 1, pp. 544–555, 2013.

[150] J. Nicholson, L. Meng, J. Fini, R. Windeler, A. DeSantolo, E. Monberg, F. DiMarcello, Y. Dulashko, M. Hassan, and R. Ortiz, “Measuring higher-order modes in a low-loss, hollow-core, photonic-bandgap fiber,” *Optics Express*, vol. 20, no. 18, pp. 20 494–20 505, 2012.

[151] J. W. Nicholson, J. M. Fini, A. M. DeSantolo, X. Liu, K. Feder, P. S. Westbrook, V. R. Supradeepa, E. Monberg, F. DiMarcello, R. Ortiz, C. Headley, and D. J. DiGiovanni, “Scaling the effective area of higher-order-mode erbium-doped fiber amplifiers,” *Optics Express*, vol. 20, no. 22, pp. 24 575–24 584, 2012.

[152] C. Jollivet, D. Flamm, M. Duparré, and A. Schülzgen, “Detailed Characterization of Optical Fibers by Combining S^2 Imaging With Correlation Filter Mode Analysis,” *Journal of Lightwave Technology*, vol. 32, no. 6, pp. 1068–1074, 2014.

[153] M. Plöschner, T. Tyc, and T. Čižmár, “Seeing through chaos in multimode fibres,” *Nature Photonics*, vol. 9, no. 8, pp. 529–535, 2015.

[154] N. K. Fontaine, R. Ryf, H. Chen, D. T. Neilson, K. Kim, and J. Carpenter, “Laguerre-Gaussian mode sorter,” *Nature Communications*, vol. 10, no. 1, p. 1865, 2019.

[155] C. Okonkwo, M. Van Den Hout, S. van der Heide, and J. van Weerdenburg, “Fibre device estimation techniques for SDM transmission,” in *European Conference on Optical Communication (ECOC)*, 2021, p. We1C2.1.

[156] I. Coddington, N. Newbury, and W. Swann, “Dual-comb spectroscopy,” *Optica*, vol. 3, no. 4, pp. 414–426, 2016.

[157] A. Parriaux, K. Hammani, and G. Millot, “Electro-optic frequency combs,” *Advances in Optics and Photonics*, vol. 12, no. 1, pp. 223–287, 2020.

[158] I. R. Salgado, “Microcombs for ultrafast optical interferometryg,” Ph.D. thesis, Chalmers University of Technology, 2023.

[159] H. Yu, K. Ni, Q. Zhou, X. Li, X. Wang, and G. Wu, “Digital error correction of dual-comb interferometer without external optical referencing information,” *Optics Express*, vol. 27, no. 20, pp. 29 425–29 438, 2019.

[160] A. Shams-Ansari, M. Yu, Z. Chen, C. Reimer, M. Zhang, N. Picqué, and M. Loncar, “Microring Electro-Optic Frequency Comb Sources for Dual-Comb Spectroscopy,” in *Conference on Lasers and Electro-Optics (CLEO)*, 2019, p. JTh5B.8.

[161] S. Wang, X. Fan, B. Xu, B. Wang, J. Du, and Z. He, “Hybrid dual-comb interferometer with easily established mutual coherence and a very high refresh rate,” *Optics Letters*, vol. 43, no. 14, pp. 3441–3444, 2018.

[162] M. Imrul Kayes and M. Rochette, “Fourier transform spectroscopy by repetition rate sweeping of a single electro-optic frequency comb,” *Optics Letters*, vol. 43, no. 5, pp. 967–970, 2018.

[163] D. R. Carlson, D. D. Hickstein, D. C. Cole, S. A. Diddams, and S. B. Papp, “Dual-comb interferometry via repetition rate switching of a single frequency comb,” *Optics Letters*, vol. 43, no. 15, pp. 3614–3617, 2018.

[164] F. Ferdous, D. E. Leaird, C.-B. Huang, and A. M. Weiner, “Dual-comb electric-field cross-correlation technique for optical arbitrary waveform characterization,” *Optics Letters*, vol. 34, no. 24, pp. 3875–3877, 2009.

[165] V. Durán, S. Tainta, and V. Torres-Company, “Ultrafast electrooptic dual-comb interferometry,” *Optics Express*, vol. 23, no. 23, pp. 30 557–30 569, 2015.

[166] P. Martín-Mateos, B. Jerez, and P. Acedo, “Dual electro-optic optical frequency combs for multiheterodyne molecular dispersion spectroscopy,” *Optics Express*, vol. 23, no. 16, pp. 21 149–21 158, 2015.

[167] G. Millot, S. Pitois, M. Yan, T. Hovhannisyan, A. Bendahmane, T. W. Hänsch, and N. Picqué, “Frequency-agile dual-comb spectroscopy,” *Nature Photonics*, vol. 10, no. 1, pp. 27–30, 2016.

[168] J. J. A. van Weerdenburg, “High-multiplicity space-division multiplexed transmission systems,” Ph.D. thesis, Technische Universiteit Eindhoven, 2019.

[169] E. D. Moore, “Advances in swept-wavelength interferometry for precision measurements,” Ph.D. thesis, University of Colorado, 2011.

[170] M. Badar, P. Lu, M. Buric, and P. Ohodnicki Jr, “Integrated auxiliary interferometer for self-correction of nonlinear tuning in optical frequency domain reflectometry,” *Journal of Lightwave Technology*, vol. 38, no. 21, pp. 6097–6103, 2020.

[171] U. Glombitza and E. Brinkmeyer, “Coherent frequency-domain reflectometry for characterization of single-mode integrated-optical waveguides,” *Journal of Lightwave Technology*, vol. 11, no. 8, pp. 1377–1384, 1993.

[172] K. Takada, “High-resolution OFDR with incorporated fiber-optic frequency encoder,” *IEEE Photonics Technology Letters*, vol. 4, no. 9, pp. 1069–1072, 1992.

[173] E. D. Moore and R. R. McLeod, “Correction of sampling errors due to laser tuning rate fluctuations in swept-wavelength interferometry,” *Optics Express*, vol. 16, no. 17, pp. 13 139–13 149, 2008.

[174] S. Fujii and T. Tanabe, “Dispersion engineering and measurement of whispering gallery mode microresonator for Kerr frequency comb generation,” *Nanophotonics*, vol. 9, no. 5, pp. 1087–1104, 2020.

[175] K. Twayana, Z. Ye, Óskar B. Helgason, K. Vijayan, M. Karlsson, and V. Torres-Company, “Frequency-comb-calibrated swept-wavelength interferometry,” *Optics Express*, vol. 29, no. 15, pp. 24 363–24 372, 2021.

[176] J. Carpenter, B. J. Eggleton, and J. Schröder, “Spatially and temporally resolved imaging of modal content in photonic-bandgap fiber,” in *Conference on Lasers and Electro-Optics (CLEO)*, 2014, p. STu3N.2.

[177] R. S. B. Ospina, M. van den Hout, J. C. Alvarado-Zacarias, J. E. Antonio-López, M. Bigot-Astruc, A. A. Correa, P. Sillard, R. Amezcua-Correa, C. Okonkwo, and D. A. A. Mello, "Mode-dependent loss and gain estimation in SDM transmission based on MMSE equalizers," *Journal of Lightwave Technology*, vol. 39, no. 7, pp. 1968–1975, 2021.

[178] N. K. Fontaine, R. P. Scott, L. Zhou, F. M. Soares, J. P. Heritage, and S. J. B. Yoo, "Real-time full-field arbitrary optical waveform measurement," *Nature Photonics*, vol. 4, no. 4, pp. 248–254, 2010.

[179] S. Gross and M. J. Withford, "Ultrafast-laser-inscribed 3D integrated photonics: challenges and emerging applications," *Nanophotonics*, vol. 4, no. 1, pp. 332–352, 2015.

[180] T. Hayashi and S. Tainta, "Record-low spatial mode dispersion and ultra-low loss coupled multi-core fiber for ultra-long-haul transmission," *JLT*, vol. 35, no. 3, pp. 450–457, 2017.

[181] R. Ryf and R.-J. Essiambre, "Impulse response analysis of coupled-core 3-core fibers," in *European Conference on Optical Communications (ECOC)*, 2012, p. Mo.1.F.4.

[182] M. Mazur, N. K. Fontaine, R. Ryf, A. Marotta, H. Chen, T. Hayashi, T. Nagashima, T. Nakanishi, T. Morishima, F. Graziosi, A. Mecozzi, and C. Antonelli, "Transfer matrix characterization of field-deployed MCFs," in *European Conference on Optical Communications (ECOC)*, 2020, pp. Th1A–4.

[183] N. R. Newbury, I. Coddington, and W. Swann, "Sensitivity of coherent dual-comb spectroscopy," *Optics Express*, vol. 18, no. 8, pp. 7929–7945, 2010.

[184] M. I. Bodine, "Superresolved swept-wavelength interferometry: fundamental limits and use in three-dimensional surface characterization," Ph.D. thesis, University of Colorado at Boulder, 2017.

[185] A. Splett, C. Kurtzke, and K. Petermann, "Ultimate transmission capacity of amplified optical fiber communication systems taking into account fiber nonlinearities," in *Proc. Eur. Conf. Opt. Commun.*, 1993.

[186] L. Beygi, N. V. Irukulapati, E. Agrell, P. Johannisson, M. Karlsson, H. Wymeersch, P. Serena, and A. Bononi, "On nonlinearly-induced noise in single-channel optical links with digital backpropagation," *Opt. Express*, vol. 21, no. 22, pp. 26 376–26 386, Nov 2013.

[187] A. Nespola, S. Straullu, A. Carena, G. Bosco, R. Cigliutti, V. Curri, P. Poggiolini, M. Hirano, Y. Yamamoto, T. Sasaki, J. Bauwelinck, K. Verheyen, and F. Forghieri, "GN-model validation over seven fiber types in uncompensated PM-16QAM Nyquist-WDM links," *IEEE Photonics Technology Letters*, vol. 26, no. 2, pp. 206–209, 2014.

[188] R. Dar, M. Feder, A. Mecozzi, and M. Shtaif, "Properties of nonlinear noise in long, dispersion-uncompensated fiber links," *Opt. Express*, vol. 21, no. 22, pp. 25 685–25 699, Nov 2013.

[189] A. Carena, G. Bosco, V. Curri, Y. Jiang, P. Poggiolini, and F. Forghieri, "EGN model of non-linear fiber propagation," *Opt. Express*, vol. 22, no. 13, pp. 16 335–16 362, Jun 2014.

[190] J. Zhou and H. Pu, "Analytical expressions for the crosstalk of super-modes in the tightly bounded multicore fibers," *Optics Express*, vol. 30, no. 4, pp. 4833–4844, 2022.

[191] B. E. A. Saleh and M. C. Teich, *Fundamentls of Photonics*, 2nd ed. Wiley, 2007.

[192] A. Ankiewicz, A. Snyder, and X.-H. Zheng, "Coupling between parallel optical fiber cores–critical examination," *J. Lightwave Technol.*, vol. 4, no. 9, pp. 1317–1323, Sep. 1986.

[193] L. N. Trefethen and D. Bau, III, *Numerical Linear Algebra.* Philadelphia, PA: Society for Industrial and Applied Mathematics, 1997.

[194] E. Deriushkina, "Notebooks and calculations for the PhD thesis "Characterisation and modeling of CCFs"," Apr. 2024. [Online]. Available: https://zenodo.org/records/10964913

[195] N. Gisin and J. Pellaux, "Polarization mode dispersion: time versus frequency domains," *Optics Communications*, vol. 89, no. 2-4, pp. 316–323, May 1992.

[196] N. J. Higham, *Accuracy and Stability of Numerical Algorithms, Ch. 26*, 2nd ed. SIAM, 2002.

[197] N. Higham, "What is a random orthogonal matrix?" Apr. 2020. [Online]. Available: https://nhigham.com/2020/04/22/what-is-a-random-orthogonal-matrix/

[198] M. Cappelletti, M. Mazur, N. K. Fontaine, R. Ryf, T. Hayashi, A. Mecozzi, M. Santagiustina, A. Galtarossa, C. Antonelli, and L. Palmieri, "Statistical analysis of modal dispersion in field-installed coupled-core fiber link," *J. Lightw. Technol*, 2024, early access.

[199] F. Yang, L.-J. Zhang, Z.-Y. Zhang, X.-J. Zhou, and Y. Liu, "Nonlinearity-compensation-free optical frequency domain reflectometry based on electrically-controlled optical frequency sweep," *Journal of Electronic Science and Technology*, vol. 19, no. 1, p. 100025, 2021.

Included papers A–F

Paper A

"Characterisation of a coupled-core fiber using dual-comb swept-wavelength interferometry",
Ekaterina Deriushkina, Israel Rebolledo-Salgado, Mikael Mazur, Victor Torres-Company, Peter Andrekson, Simon Gross, Michael J. Withford, Tetsuya Hayashi, Takuji Nagashima, Jochen Schröder, and Magnus Karlsson,
European Conference on Optical Communication (ECOC), Bordeaux, France, Sep 2021.

Paper B

"Dual-comb swept-wavelength interferometry: Theory and Experiment",
Ekaterina Deriushkina, Israel Rebolledo-Salgado, Mikael Mazur, Victor Torres-Company, Peter Andrekson, Jochen Schröder, and Magnus Karlsson,
Journal of Lightwave Technology, vol. 40, no. 19, pp. 6508-6516, Oct, 2022.

Paper C

“Modeling of 3-Coupled-Core Fiber: Comparison Between Scalar and Vector Random Coupling Models”,
Ekaterina Deriushkina, Jochen Schröder, and Magnus Karlsson,
Journal of Lightwave Technology, vol. 42, no. 2, pp. 793-801, Jan, 2024.

Paper D

“Analysis of the Scalar and Vector Random Coupling Models For a Four Coupled-Core Fiber”,
Ekaterina Deriushkina, Jochen Schröder, and Magnus Karlsson,
European Conference on Optical Communication (ECOC), Glasgow, UK, Oct 2023.

Paper E

"Circuit Implementation of Pilot-Based Dynamic MIMO Equalization for Coupled-Core Fibers",
Ekaterina Deriushkina, Jochen Schröder, and Magnus Karlsson,
Optical Fiber Communication Conference (OFC), San Diego, USA, March, 2024.

Paper F

“Dynamic Model For Coupled-Core Fibers”,
Ekaterina Deriushkina, Jochen Schröder, and Magnus Karlsson,
Journal of Lightwave Technology, submitted.